Experimental and Numerical Assessment of Adhesively Bonded Non-Crimp Fabric Carbon Fiber/Epoxy Composite Joints

by

Ramin Chitsaz Dehaghani

A thesis
presented to the University of Waterloo
in fulfillment of the
thesis requirement for the degree of
Master of Applied Science
in
Mechanical and Mechatronics Engineering

Waterloo, Ontario, Canada, 2021

AUTHOR'S DECLARATION

I hereby declare that I am the sole author of this thesis. This is a true copy of the thesis, including any required final revisions, as accepted by my examiners.

I understand that my thesis may be made electronically available to the public.

Abstract

To achieve a reduction in the contribution of greenhouse gas emissions from the transportation sector, automotive manufacturers have shifted towards utilization of advanced lightweight materials for vehicle structures, including fibre reinforced plastic (FRP) composite materials. FRPs exhibit desirable high specific strength, stiffness and energy absorption capabilities; however, they often have relatively high manufacturing costs and duration of part manufacture cycles. The recent development of heavy-tow non-crimp fabric (NCF), rapid curing resins and automated fabrication processes such as high-pressure resin transfer moulding (HP-RTM) enable reduced manufacturing cost and cycle times, which may accelerate the integration of FRP composites into the structures of high-volume production vehicles.

A prevailing challenge for FRP composite structures is the design and assessment of robust joining methods. Conventional mechanical fastener joining methods require drilling holes in FRP parts, which affects the continuity of the reinforcing fibres, causes local damage around the periphery of the drilled hole, and ultimately degrades mechanical performance of the composite. On the contrary, owing to lower structural weight, lower fabrication cost, and improved damage tolerance, adhesive bonding is a more widely considered joining method for the assembly of composite structures. The objective of this thesis was to assess the performance and fracture behaviour of adhesively bonded NCF carbon-fibre-reinforced plastic (CFRP) composite joints.

During the first part of this study, adhesively bonded NCF-CFRP single lap joints (SLJ) were used to assess the influence of the composite adherend surface treatment and stacking sequence on the joint strength. The highest joint strength (24.7 MPa) was achieved for specimens with adherends treated by abrading the surface with sandpaper compared to acetone degreasing or grit blasting. Furthermore, specimens comprising adherends with a higher effective flexural longitudinal modulus exhibited higher joint strength. Variation in the CFRP adherend stacking sequence also led to distinct failure processes. The intra-ply and inter-ply cracks observed in the adherends were driven by local in-plane and out-of-plane stresses, which was confirmed through corresponding three-dimensional finite element analyses of the SLJ specimens.

During the second part of the study, double cantilever beam (DCB) tests were employed to assess the effects of adherend fibre volume fraction, adhesive bond-line thickness and loading rate on Mode I fracture behaviour of adhesively bonded NCF-CFRP joints. Increasing the fibre volume fraction of the CFRP adherend, the bond-line thickness of the adhesive or the loading rate increased the average Mode I critical strain energy release rate (G_{Ic}). A two-dimensional finite element model was employed to calibrate the Mode I traction-separation law parameters for a cohesive zone model using a commercial finite element software (ABAQUS 6.14-2). The predicted force-displacement response was in good agreement with that of the DCB tests, which demonstrates the capability of the numerical model to capture the macroscopic response of the DCB specimen.

Acknowledgements

I would like to express my gratitude towards my colleagues, friends, and family. I will start off by thanking my supervisors Dr. John Montesano and Dr. Duane Cronin for their mentorship, patience and great professionalism providing me with advice and encouragement throughout the whole process of completing this project. Their insight and support throughout this journey have been invaluable to my personal development.

I also would like to express my appreciation to the industrial sponsors Honda R&D Americas, Hexion Inc., Zoltek Corporation, LAVAL International and 3M^{TM} Canada. In addition, I would like to express my thanks to Natural Science and Engineering Research Council of Canada (NSERC) and Ontario Centers of Excellence (OCE) for providing funding for the project.

I would also like to thank the university laboratory staff: Tom Gawel, Andy Barber, Doug Hirst, and Eckhard Budziarek, for always being available and willing to help. Special thanks to Brock Watson, Chi-Hsiang Liao, Michael Bustamante, Devon Hartlen and Mehdi Ghazimoradi for helping me and answering all my questions about lab equipment.

Thank you to all the group member in the Composites Research Group: Farzad Sharifpour, Pravin Gopal Samy Dharmaraj, Khizar Rouf, Zohreh Asaee, Sanaz Hashemi, Mehdi Ghazimoradi, Devon Hartlen, Eleazar Alberto Trejo Sandoval, Yu Zeng and Ben Harvey and also IMMC group: Ahmed Ibrahim, Aleksander Lukasz Rycman, Brock Watson, Chi-Hsiang Liao, Chris Pastula, Devon Hartlen, Dilaver Singh, Donata Gierczycka, Jeffrey Barker, Kathy Tang, Marwan Darweesh, Matheus Augusto Correia, Mayank Kalra, Miguel A. Corrales Fabre, Mike Bustamante, Nancy Evans, Prasannaah and Sophia Ngan for making it fun to

come to the EC4 office and the good times shared over meals and hangouts. I would also like to thank Aaditya Suratkar for sharing the experimental data to validate my research results.

Finally, I want to thank my dad, my mom and my sister for their emotional support and their unconditional encouragement through this journey. To my friends which I have enjoyed my time with you and help me walk through all challenges.

To my family, Alireza, Yasaman and Nazanin

Table of Contents

List of Figures

List of Tables

Chapter 1: Introduction

1.1 Research Motivation

Corporate Average Fuel Economy (CAFÉ) standards in the United States and other regulations legislated in Canada, Asia and Europe aim to reduce greenhouse gas emissions and increase fuel efficiency of light-duty vehicles (LDVs) [1–4]. Several approaches can be used to improve fuel efficiency, including improving aerodynamic efficiency, developing new efficient powertrains, and optimizing vehicle body-in-white (BIW) structures for weight reduction [5]. A key factor for improving the fuel efficiency of LDVs is to reduce vehicle weight [6]. A reduction of vehicle weight by 10% can lead to a 6-8% improvement in fuel economy for a vehicle with an internal combustion engine, while the driving range of an electric vehicle can be increased by 13.7% [7]. The approach to light-weighting incorporates advanced materials such as aluminum, magnesium, high-strength steel and high-performance fibre-reinforced plastic (FRP) composite materials into BIW structures. The use of FRP composite materials in the structures of LDVs has increased in recent years, owing to their high specific strength, stiffness, and energy absorption capabilities [8, 9] (Figure 1).

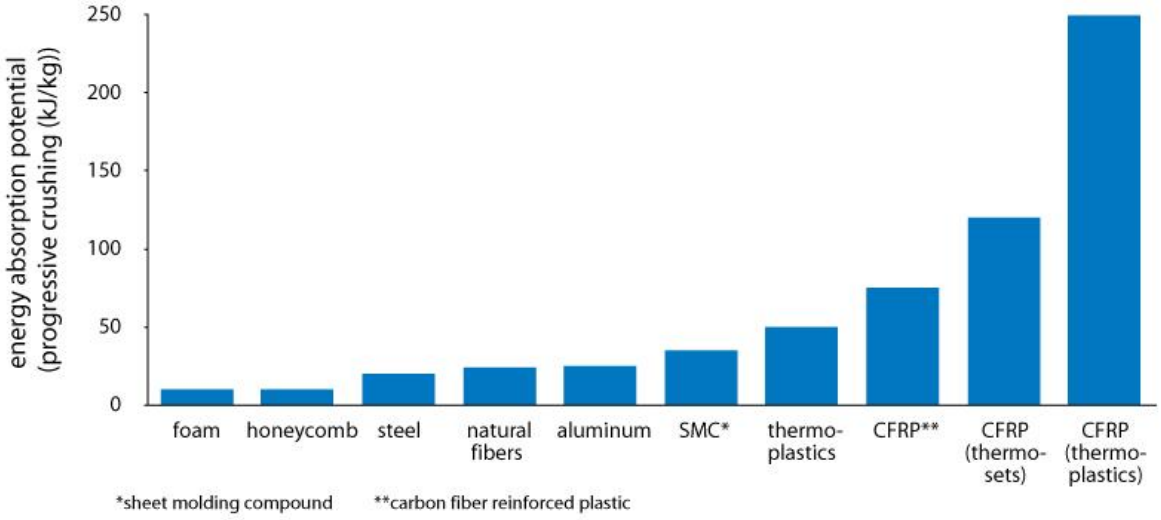

Figure 1.1. A comparison of energy absorption potential between advanced composite materials and other types of materials [10].

Despite the advantages of FRP composite materials, high manufacturing costs and long cycle times has limited their adoption in BIW structures of luxury vehicles such as the BMW 7 Series [11], the Audi R8 [12] and Lamborgini Murciélago 670 [13]. The recent development of heavy-tow carbon fibre-based non-crimp fabric (NCF) [14], rapid curing resin systems [15] and automated processing technologies such as high-pressure resin transfer moulding (HP-RTM) [16] provide additional advantages over more conventional laminated FRP composites. This includes reduced manufacturing cost and cycle times, which provide a robust potential to incorporate the FRP composite materials in the BIW structures of high-volume production vehicles.

A prevailing challenge for composite structures is the design and assessment of robust joining methods. Conventional mechanical joining methods that utilize fasteners such as bolts and rivets require drilling holes in FRP parts, which causes local damage around the periphery

of the drilled hole, cutting of the reinforcement fibres, and ultimately a drastic degradation of the structural integrity [17]. In contrast, adhesive bonding provides advantages over mechanical joining methods such as lower structural weight by eliminating fasteners, lower assembly cost, and improved damage tolerance [18]. In addition, adhesively bonded joints reduce noise, vibration, and harshness (NVH) in the vehicle structure due to structural damping [19]. As a result, adhesive bonding has become a more widely used joining method for FRP components in recent years. An important process during the preparation of an adhesively bonded joint is the surface treatment applied to the bonded components, which plays an important role in the performance and the morphology of the failure process of adhesively bonded FRP joints [20]. Common surface treatments for FRP composites include the use of a peel ply during fabrication, mechanical abrasion, and laser treatments such as plasma treatment. Despite several important studies that have been conducted to assess the influence of surface treatment on performance of adhesively bonded joints, inconsistent findings have been reported [21–24].

Finite element analysis (FEA) is widely used in the automotive sector as a computer-aided engineering (CAE) design tool for assessing the impact performance of vehicle structures [25]. Characterization of adhesively bonded joints under different loading conditions is a primary requirement to improve the prediction capability of CAE simulation models for structures with adhesive joints [25]. The required mechanical properties range from joint strength values for a specific joint configuration to full traction–separation curves that are required to calibrate a cohesive zone model (CZM) [26]. These parameters are often determined by a variety of fracture tests such as double cantilever beam (DCB), end notch flexure (ENF) and mixed-mode

tests [25]. However, a finite element analysis is required to compliment the results of experimental tests to calibrate the CZM parameters. However, a survey of the literature has revealed that an in-depth study on assessment the fracture behaviour characterization of adhesively bonded FRP joints is focused on those with woven or braided composite adherends, while studies on joints with non-crimp fabric composite adherends is currently lacking [27–29].

1.2 . Research Objectives

Owing to an increased interest in the automotive sector to incorporate carbon fibre-reinforced plastics (CFRPs) into the BIW structures of LDVs, the overall goal of this thesis was to assess the performance and fracture behaviour of adhesively bonded NCF-CFRP composite joints. The main research objectives are summarized as follows:

- Assess the influence of adherend surface treatment and stacking sequence on the strength and failure mechanisms of NCF-CFRP single lap joints (SLJs).
- Characterize the Mode I fracture behaviour of adhesively bonded NCF-CFRP joints and investigate the influence of adhesive bond line thickness and loading rate on fracture toughness.
- Develop a numerical model to calibrate the Mode I traction-separation law parameters of adhesively bonded NCF-CFRP joints for a corresponding cohesive zone model.

1.3 . Thesis Overview

This remainder of the thesis is organized into six chapters. In Chapter 2, the theoretical background and relevant literature review of FRP composite and adhesive materials are presented, while the limitations and gaps of previous research focused on adhesively bonded FRP joints is discussed. In chapter 3, details of materials and test methods used to determine the performance and fracture behaviour of adhesively bonded joints are described. Chapter 4 outlines the numerical modelling methods used to assess the local stress fields in the SLJ specimens and to calibrate the CZM parameters for the Mode I fracture tests. Chapter 5 presents the experimental and numerical results for different SLJ and DCB specimen configurations. In Chapter 6, the relevant research findings and results are discussed. Chapter 7 wraps up the thesis with conclusions and recommendations for future work.

Chapter 2: Background and Literature Review

In this chapter, a general overview of FRP composite materials including manufacturing process methods, theoretical stress analysis and details of damage mechanics is presented in Section 2.1. An introduction to adhesive materials is presented in Section 2.2, followed by a literature review focused on surface treatment, joint configuration and failure modes for adhesively bonded FRP joints in Section 2.3. Finally, an overview of fracture characterization of adhesively bonded joints and cohesive zone modelling is presented in Section 2.4.

2.1 Fiber-Reinforced Plastic Composite Materials

2.1.1 Material System

FRP composite materials consist of high-performance reinforcement fibres and a polymer matrix material, which results in a heterogeneous material with distinct interfaces separating the different phases [30]. An important advantage of FRP composite materials compared to homogeneous materials is the ability to tailor the material system to achieve the desired properties for an intended application. FRP composite materials are also inherently damage tolerant, and exhibit excellent fatigue performance and energy absorption characteristics [31].

A key role of the polymer matrix is to transfer applied loads to the fibres [30]. Additional roles include maintaining fibres in a required orientation, protecting the fibres from environmental degradation, and defining the part geometry [32]. The matrix phase is typically a thermosetting or thermoplastic polymer, with the former more widely used for structural applications. Epoxy resins are a class of thermosetting polymers that exhibit low viscosity for ease and flexibility of processing, good mechanical properties and thermal stability, and acceptable cost. Epoxies have been extensively used in FRP composites for applications in

several industrial sectors [30]. During the last decade, new rapid curing epoxy resins have been formulated and are being considered to fabricate high-performance FRP composites for structural applications in the automotive sector [15].

For the reinforcement fibres, the main role is to support the majority of the load applied to the FRP material. Owing to a small diameter and reduced probability of defects, fibres are inherently stronger than the bulk form of the corresponding material [30]. Common fibre types used in structural FRP composites include glass, carbon, and aramid [33]. Carbon fibres are widely utilized in high-performance FRP composites, and are produced commercially by the thermal decomposition of organic precursor fibres such as rayon or polyacrylonitrile (PAN) [34]. Reinforcement fibre tows are often used in the form of fabrics to fabricate FRP parts comprised of continuous fibres. Common fabric architectures include woven, multi-axial braided, knitted, and stitched non-crimp fabrics (NCF). NCFs have been used increasingly in industrial applications in recent years [35] in various forms, including unidirectional NCF (UD-NCF) layers and multidirectional NCF layers.

UD-NCFs are comprised of a single layer of aligned continuous fibre tows that are stitched to one another with a polyester yarn. Pillar, cord, satin, and tricot stitching patterns are commonly used, where the tricot stitching pattern typically follows the direction of the carbon fibre tows in a zig-zag form (Figure 2.1). Transversely oriented supporting fibres are typically placed between the tows and the stitching to provide support for the fabric when handling during FRP part processing [36]. UD-NCFs provide several advantages when compared to woven or braided fabrics including improved reinforcement performance during processing

[37, 38] and reduced manufacturing cost owing to the simplicity of the architecture of UD-NCFs [39].

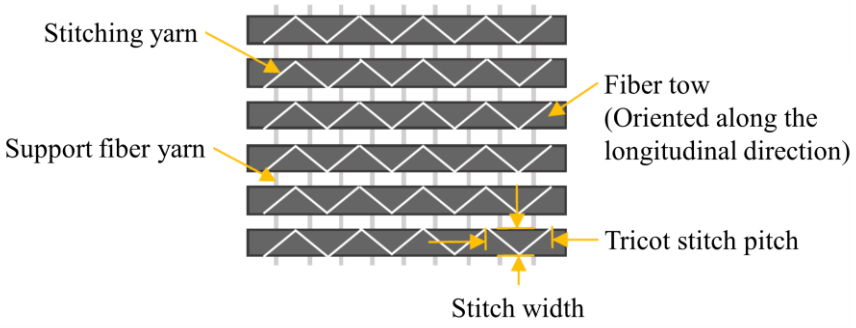

Figure 2.1. Schematic of a unidirectional non-crimp fabric with tricot stitching pattern [36].

A common class of FRP part fabrication methods that utilize a stack of reinforcement fabrics and liquid thermosetting resins are liquid composite moulding (LCM) processes [40]. A closed two-part mould is used where the dry fabric layers are first placed in the mould cavity and the resin is later introduced for subsequent curing under pressure and elevated temperature. Resin transfer moulding (RTM) is a commonly used LCM processes where the liquid resin is injected into a closed heated mould under low pressures (Figure 2.2) [41]. RTM processes have the ability to repeatable fabricate high-quality FRP composite parts with complex geometry and good dimensional stability [42].

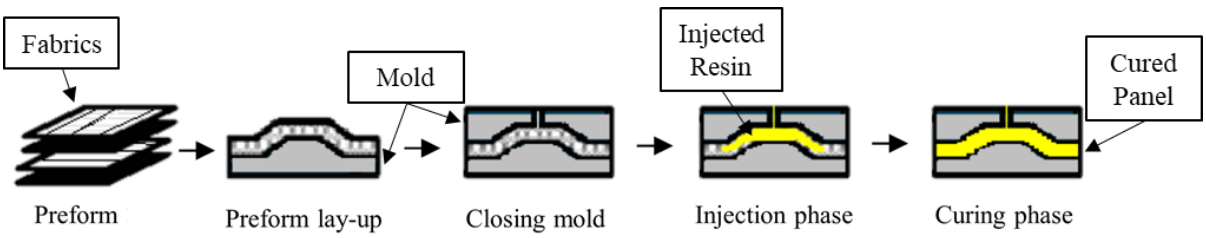

Figure 2.2. Resin transfer moulding process steps [43].

High-pressure resin transfer moulding (HP-RTM) had been developed recently to enhance the RTM process, and address limitations such as intrinsically long processing cycles [44]. During the HP-RTM process, a highly reactive rapid curing resin and hardener are mixed immediately prior to being injected at high flow rates into the closed mould [45] resulting in improved surface finish and higher attainable fibre volume fractions for the FRP parts. Due to the high pressures generated within the closed mould, large presses are required to hold the tool in a shut and sealed position during resin injection. UD-NCFs have been recently used to produce CFRP parts using an HP-RTM process [42].

2.1.2 Mechanics of Laminated Composites

Continuous FRP materials are typically comprised of several layers (a.k.a., plies or laminae) stacked together and oriented along different directions to achieve the required anisotropic mechanical properties. Characterization of the failure modes of laminated FRP materials is a complex topic owing to the number of exhibited intra- and inter-laminar damage mechanisms [46]. In addition, since the strength of an anisotropic lamina is higher along the fibre direction, failure is a function of the direction of the applied stress relative to the direction of the fibres [47]. As a result, a lamina may exhibit a linear elastic response until failure or an elastic-inelastic response prior to failure. The linear elastic anisotropic response of lamina is governed by three-dimensional generalized Hooke's law, as per the following set of equations represented using index notation:

$$\sigma_{ij} = C_{ijkl}\varepsilon_{kl} \tag{2.1}$$

Here, σ_{ij}, C_{ijkl} and ε_{kl} are respectively the components of the second-order Cauchy stress tensor, the fourth-order homogenized elastic tensor components and the components of the second-order infinitesimal strain tensor, where indices i, j, k, l = 1, 2, 3. There are 81 components for the elastic tensor for a fully anisotropic material. The symmetry of the stress tensor can be deduced by applying the principle of equilibrium. The number of the independent constants of the elastic tensor is reduced to 21 by consideration of the symmetry of the strain tensor. For unidirectional composites, such as UD-NCF lamina, the existence of three mutually orthogonal planes of material symmetry leads to an orthotropic material response, which further reduces the independent components of the elastic tensor to 9. For a UD lamina, the local material coordinate system can be defined based on the 1, 2, 3 indices, with 1 representing the fibre direction, 2 the in-plane transverse fibre direction and 3 the out-of-plane direction (Figure 2.3).

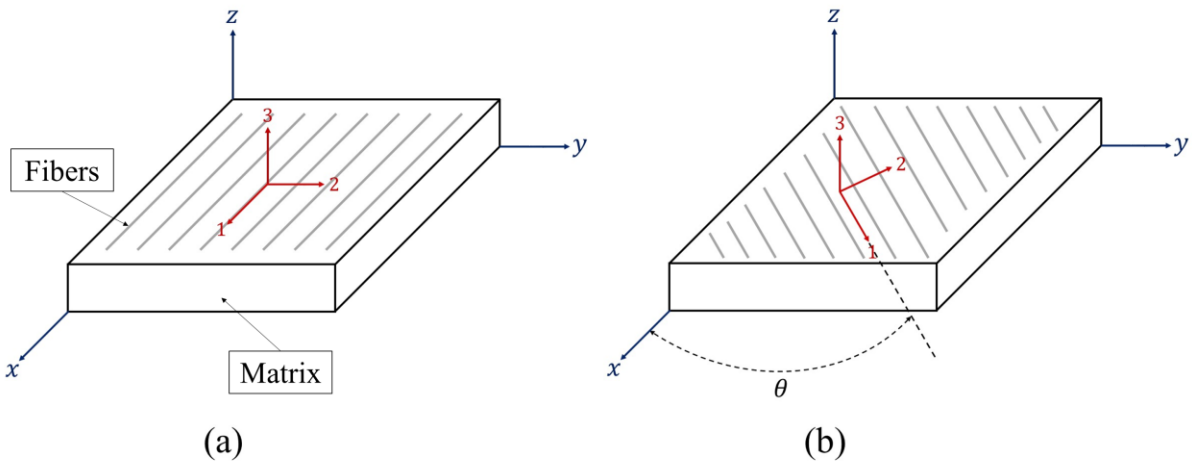

Figure 2.3. (a) The local material coordinate system for a UD composite and (b) orientation of UD lamina with respect to the laminate coordinate system (***θ*** is the angle between the x- and 1- axes).

Stress and strain tensors can be represented in vector form allowing for reduced (Voigt) notation by assuming the following definitions for the indices of the stress, strain and elastic tensors: 11 = 1, 22 = 2, 33= 3, 23 = 4, 13 = 5 and 12 = 6. The stress-strain relations for a three-dimensional orthotropic lamina in reduced notation is defined as [32]:

$$\begin{bmatrix}\sigma_1\\ \sigma_2\\ \sigma_3\\ \sigma_4\\ \sigma_5\\ \sigma_6\end{bmatrix} = \begin{bmatrix}C_{11} & C_{12} & C_{13} & 0 & 0 & 0\\ C_{21} & C_{22} & C_{23} & 0 & 0 & 0\\ C_{31} & C_{32} & C_{33} & 0 & 0 & 0\\ 0 & 0 & 0 & C_{44} & 0 & 0\\ 0 & 0 & 0 & 0 & C_{55} & 0\\ 0 & 0 & 0 & 0 & 0 & C_{66}\end{bmatrix}\begin{bmatrix}\varepsilon_1\\ \varepsilon_2\\ \varepsilon_3\\ \varepsilon_4\\ \varepsilon_5\\ \varepsilon_6\end{bmatrix} \tag{2.2}$$

$$C_{ij} = S_{ij}^{-1} \tag{2.3}$$

Here, C_{ij} and S_{ij} are respectively the components of the elastic tensor and the compliance tensor. The compliance tensor components can be written in terms of the orthotropic elastic constants as follows [47]:

$$S_{11} = \frac{1}{E_1}, S_{22} = \frac{1}{E_2}, S_{33} = \frac{1}{E_3} \tag{2.4}$$

$$G_{23} = \frac{1}{S_{44}}, G_{13} = \frac{1}{S_{55}}, G_{23} = \frac{1}{S_{66}} \tag{2.5}$$

$$\nu_{23} = -\frac{S_{23}}{S_{22}}, \nu_{13} = -\frac{S_{13}}{S_{11}}, \nu_{12} = \frac{S_{12}}{S_{11}} \tag{2.6}$$

Here, E_i, G_{ij} and ν_{ij} are respectively Young's moduli, shear moduli and Poisson's ratios of the effectively homogeneous lamina with respect to the local material coordinate system. It should be noted that E_i, G_{ij} and ν_{ij} are dependent on the properties of the constituent materials (i.e. the reinforcement fibre and polymer matrix) and the fibre volume fraction (V_f).

The out-of-plane stresses can be assumed zero by considering the plane stress condition for the case when the laminae are thin. As a result, Equation 2.2 is reduced from three dimensions to two dimensions:

$$\begin{bmatrix}\sigma_1\\ \sigma_2\\ \sigma_{12}\end{bmatrix}=\begin{bmatrix}Q_{11} & Q_{12} & 0\\ Q_{21} & Q_{22} & 0\\ 0 & 0 & Q_{66}\end{bmatrix}\begin{bmatrix}\varepsilon_1\\ \varepsilon_2\\ \gamma_{12}\end{bmatrix} \tag{2.7}$$

The components of the reduced stiffness matrix $[Q]$ can be written in terms of the in-plane lamina elastic constants [47]:

$$Q_{ij}=\begin{bmatrix}\frac{E_1}{1-\upsilon_{12}\upsilon_{21}} & \frac{\upsilon_{12}E_2}{1-\upsilon_{12}\upsilon_{21}} & 0\\ \frac{\upsilon_{12}E_2}{1-\upsilon_{12}\upsilon_{21}} & \frac{E_1}{1-\upsilon_{12}\upsilon_{21}} & 0\\ 0 & 0 & G_{12}\end{bmatrix} \tag{2.8}$$

For a laminate comprised of several laminae oriented along different directions, it is required to describe the orientation of each lamina with respect to the laminate coordinate system (see *x*, *y*, *z*-direction in Figure 2.4b). The orientation of a lamina can be represented as a rotation about the *z*-direction by angle θ (see Figure 2.4b). The transformation with respect to the laminate coordinate system leads to the following stress-strain relations [48]:

$$\begin{Bmatrix}\sigma_x\\ \sigma_y\\ \sigma_{xy}\end{Bmatrix}=[T_1]^{-1}[Q][T_2]\begin{Bmatrix}\varepsilon_x\\ \varepsilon_y\\ \gamma_{xy}\end{Bmatrix}=[\bar{Q}]\begin{Bmatrix}\varepsilon_x\\ \varepsilon_y\\ \gamma_{xy}\end{Bmatrix} \tag{2.9}$$

Here, $[T_1]$, $[T_2]$ and $[\bar{Q}]$ are respectively the stress transformation matrix, the strain transformation matrix (see Equations 2.10 and 2.11) and the lamina transformed reduced stiffness matrix. σ_x, σ_y and σ_{xy} are the stresses in the laminate coordinate system and ε_x, ε_y

and γ_{xy} represent the strains in the laminate coordinate system. The transformation matrices are defined by:

$$[T_1] = \begin{bmatrix} m^2 & n^2 & 2mn \\ n^2 & m^2 & -2mn \\ -mn & mn & m^2 - n^2 \end{bmatrix} \tag{2.10}$$

$$[T_1] = \begin{bmatrix} m^2 & n^2 & mn \\ n^2 & m^2 & -mn \\ -2mn & 2mn & m^2 - n^2 \end{bmatrix} \tag{2.11}$$

Here, *m* and *n* denote the transformation coefficients where $m = \cos\theta$ and $n = \sin\theta$.

The elastic response of multi-directional laminates can be defined through classical laminate theory (CLT) [48], where bending and stretching deformations of assumed thin plates are defined based on Kirchhoff's plate theory. It is assumed that the plies are under plane stress states and undergo linear elastic deformation with small strains and rotations, and that there are no out-of-plane strains. Therefore, the deformation of the laminate can be reduced to a two-dimensional problem by relating the deformation of any point through the laminate thickness with the bending and stretching deformation of the laminate geometric mid-plane (Figure 2.4a).

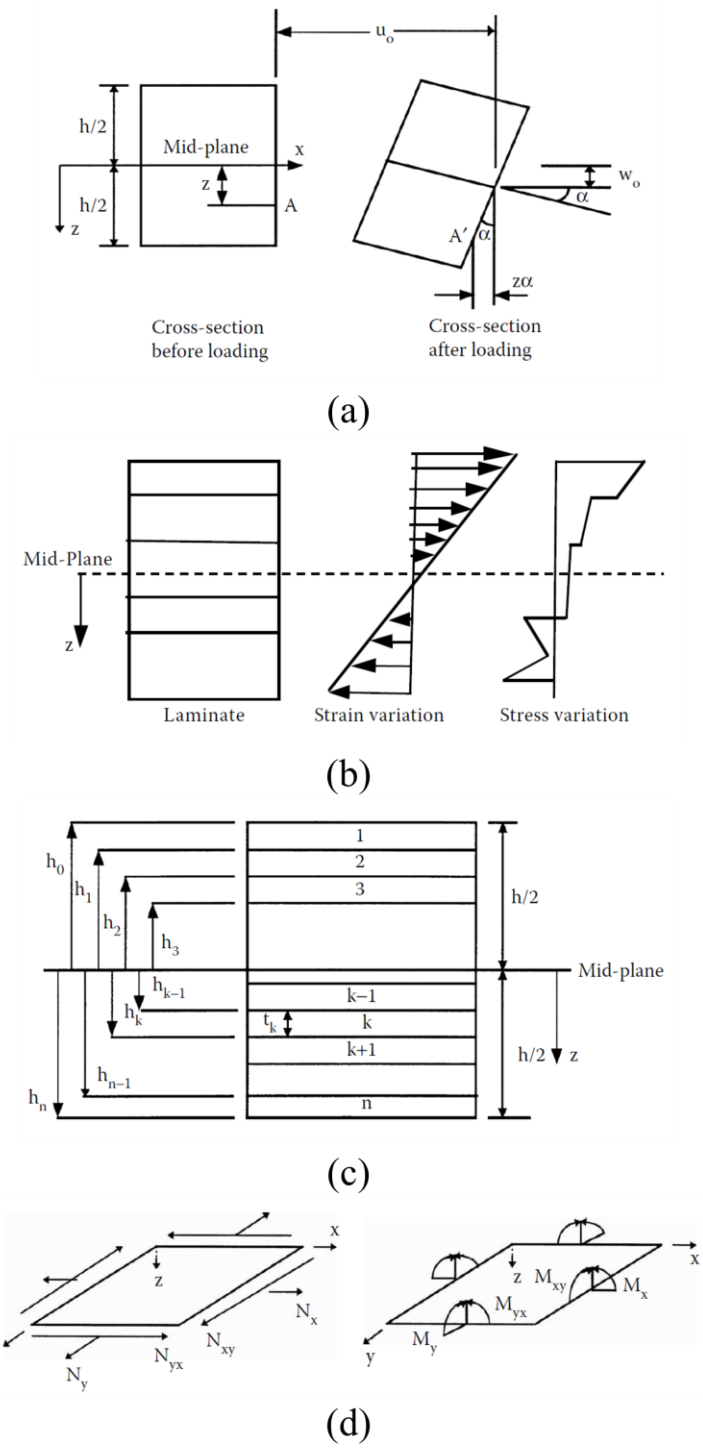

Figure 2.4. Schematic of a thin laminate plate: a) deformed and undeformed state, b) strain and stress variation through the thickness of the laminate, c) coordinate locations of plies in a laminate and d) resultant forces and moments (where $\boldsymbol{u_o}$, $\boldsymbol{v_o}$ and $\boldsymbol{w_o}$ are the displacement in the *x*, *y* and *z* direction) [48].

The strain distribution through the thickness of the laminate can be obtained from the laminate geometric mid-plane strains $\{\varepsilon_0\}$ and curvatures $\{\kappa_0\}$ (Figures 2.4b and 2.4c). The strain distribution in terms of the laminate coordinate system is defined per the following:

$$\begin{Bmatrix} \varepsilon_x \\ \varepsilon_y \\ \gamma_{xy} \end{Bmatrix} = \begin{Bmatrix} \varepsilon_x^0 \\ \varepsilon_y^0 \\ \gamma_{xy}^0 \end{Bmatrix} + z \begin{Bmatrix} \kappa_x^0 \\ \kappa_y^0 \\ \kappa_{xy}^0 \end{Bmatrix} \tag{2.12}$$

The stress distribution for ply *k* with respect to the laminate coordinate system is calculated based on the strain distribution as follows:

$$\begin{Bmatrix} \sigma_x \\ \sigma_y \\ \sigma_{xy} \end{Bmatrix}_k = \begin{bmatrix} \overline{Q_{11}} & \overline{Q_{12}} & \overline{Q_{16}} \\ \overline{Q_{21}} & \overline{Q_{22}} & \overline{Q_{26}} \\ \overline{Q_{61}} & \overline{Q_{62}} & \overline{Q_{66}} \end{bmatrix}_k \begin{Bmatrix} \varepsilon_x^0 + z\kappa_x^0 \\ \varepsilon_y^0 + z\kappa_y^0 \\ \gamma_{xy}^0 + z\kappa_{xy}^0 \end{Bmatrix} \tag{2.13}$$

Here, $[\bar{Q}]_n$ is the transformed reduced stiffness matrix for ply *k*.

The mid-plane strains and curvatures can be evaluated by considering the resultant forces $\{N\}$ and moments $\{M\}$ applied to the laminate (Figure 2.4d). The laminate governing equations are defined as:

$$\begin{Bmatrix} N_x \\ N_y \\ N_{xy} \\ M_x \\ M_y \\ M_{xy} \end{Bmatrix} = \begin{bmatrix} A_{11} & A_{12} & A_{16} & B_{11} & B_{12} & B_{16} \\ A_{21} & A_{22} & A_{26} & B_{21} & B_{22} & B_{26} \\ A_{61} & A_{62} & A_{66} & B_{61} & B_{62} & B_{66} \\ B_{11} & B_{12} & B_{16} & D_{11} & D_{12} & D_{16} \\ B_{21} & B_{22} & B_{26} & D_{21} & D_{22} & D_{26} \\ B_{61} & B_{62} & B_{66} & D_{61} & D_{62} & D_{66} \end{bmatrix} \begin{Bmatrix} \varepsilon_x^0 \\ \varepsilon_y^0 \\ \gamma_{xy}^0 \\ \kappa_x^0 \\ \kappa_y^0 \\ \kappa_{xy}^0 \end{Bmatrix} \tag{2.14}$$

The $[A]$, $[B]$ and $[D]$ are the extensional stiffness, coupling stiffness and bending stiffness matrices of the laminate, respectively. The components of the $[A]$, $[B]$ and $[D]$ matrices are

functions of the ply position (h_k) with respect to the laminate geometric mid-plane (Figure 2.4c) and are given by the following expressions:

$$A_{ij} = \sum_{k=1}^{n} \left(\overline{Q_{ij}}\right)_k (h_k - h_{k-1}) \tag{2.15}$$

$$B_{ij} = \frac{1}{2} \sum_{k=1}^{n} \left(\overline{Q_{ij}}\right)_k (h_k^2 - h_{k-1}^2) \tag{2.16}$$

$$D_{ij} = \frac{1}{3} \sum_{k=1}^{n} \left(\overline{Q_{ij}}\right)_k (h_k^3 - h_{k-1}^3) \tag{2.17}$$

Equitation 2.14 can be presented in short notation as:

$$\begin{bmatrix} N \\ - \\ M \end{bmatrix} = \begin{bmatrix} A & | & B \\ - & | & - \\ B & | & D \end{bmatrix} \begin{bmatrix} \varepsilon^0 \\ - \\ \kappa \end{bmatrix} \tag{2.18}$$

Inverting Equation 2.18 gives the following:

$$\begin{bmatrix} \varepsilon^0 \\ - \\ \kappa \end{bmatrix} = \begin{bmatrix} A^* & | & B^* \\ - & | & - \\ C^* & | & D^* \end{bmatrix} \begin{bmatrix} N \\ - \\ M \end{bmatrix} \tag{2.19}$$

The $[A^*]$, $[B^*]$ and $[D^*]$ matrices are respectively the extensional compliance matrix, coupling compliance matrix, and bending compliance matrix.

2.1.3 Failure of Laminated Composites

Different types of intra-laminar and inter-laminar damage mechanisms have been observed in laminated FRP composite materials. Intra-laminar damage mechanisms include fibre breakage, matrix micro-cracking and fibre/matrix interfacial debonding [49], which can combine and lead to lamina failure. Delamination is the main inter-laminar damage mechanism [49]. Inter-laminar stresses developed between plies owing to several causes, including the

mismatch of elastic constants and orientation between adjacent plies of a laminate as well as due to edge effects [48]. The magnitude of these stresses may be high enough to cause delamination cracks between the plies of a laminated FRP composite.

When a tensile load is applied along the fibre direction of a unidirectional lamina, failure is caused by successive breakage of the fibres. One fibre breaks and the load is transferred through the matrix to the neighbouring fibres (Figure 2.5a). The tensile strength in the fibre direction is denoted by X_t. In contrast, when a compression load is applied in the fibre direction, the lamina will fail by fibre kinking, or in-phase fibre micro-buckling (Figure 2.5b) [47]. The compression strength in the fibre direction is denoted by X_c.

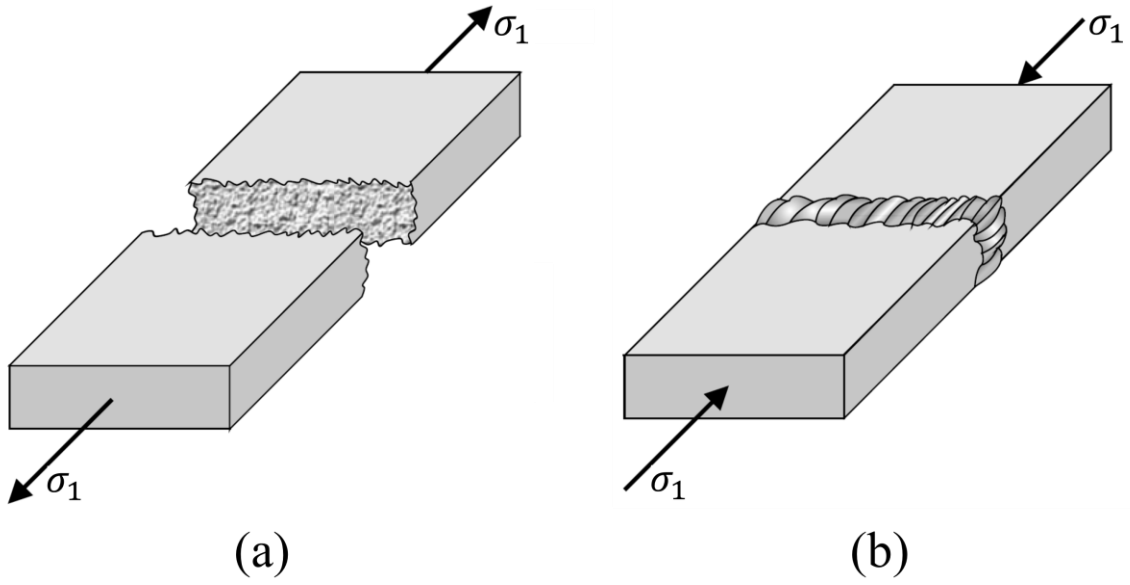

Figure 2.5. Unidirectional lamina failure along the fiber direction: (a) tension, (b) compression [50].

By applying a tensile load in the transverse direction of a unidirectional lamina (i.e., perpendicular to the fibre direction), failure is caused by a combination of matrix micro-cracks

and fibre/matrix interfacial debonds leading to the formation of a through-thickness matrix crack (Figure 2.6a). The tensile strength in the transverse direction is denoted by Y_t. By applying a compression load in the transverse direction, failure is caused by the local fibre/matrix interfacial debonding and local matrix cracks, which coalesce to form an inclined through-thickness matrix crack (Figure 2.6b) [47]. The compression strength in the transverse direction is denoted by Y_c.

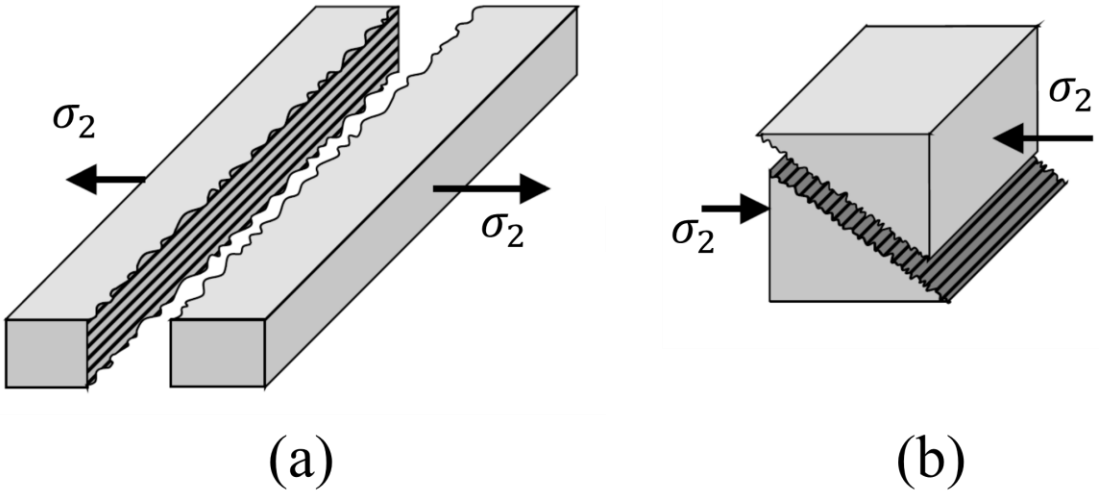

Figure 2.6. Unidirectional lamina failure along the transverse direction: (a) tension, (b) compression [50].

When an out-of-plane shear load is applied to a unidirectional lamina, the failure mechanism is analogous to that observed for tension in the transverse direction (Figure 2.7) [47]. The out of plane shear strength is denoted as S_{out}.

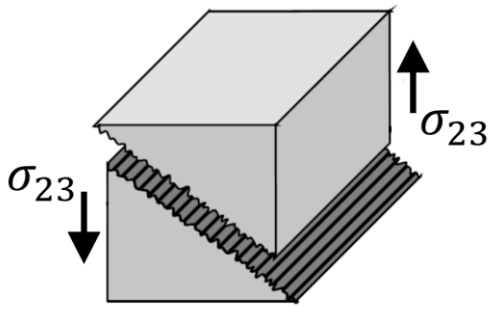

Figure 2.7. Unidirectional lamina failure by out-of-plane shear load [50].

When an in-plane shear is applied to a unidirectional lamina, the matrix between the fibres undergoes shear deformation that causes local matrix cracks resulted in fibre/matrix interfacial debonding. Afterward, these crack coalesce to form a through-thickness matrix crack leading to failure of the unidirectional lamina (Figure 2.8) [47]. The in-plane shear strength is denoted as S_{in}.

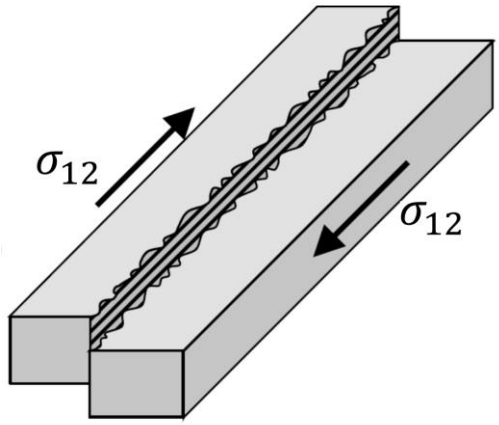

Figure 2.8. Unidirectional lamina failure by in-plane shear load [50].

Several ply-level failure criteria have been proposed for unidirectional FRP composites subjected to combined stress states, including maximum stress [48], Tsai-Wu criteria [48] and Puck's criteria [51, 52] among others. For the maximum stress criteria, three independent failure modes including axial, transverse and shear failure are considered. Thus, ply failure is predicted if any stresses (i.e. axial, transverse or shear) in the local axes exceeds the corresponding strength.

2.2 Structural Adhesives

Adhesives are commonly used for joining similar or dissimilar materials such as metals, plastics, ceramics and wood [53]. Structural adhesives are used in applications where the bonded materials or adherends bear high stresses [54]. Common types of structural adhesives include acrylics, cyanoacrylates, polyurethanes, phenolic and epoxy (Table 2.1) [55]. Epoxy adhesives are classified as thermosetting polymers and have superior adhesion and chemical resistance when compared to other types of adhesives. As a result, epoxy adhesives have seen widespread usage in different sectors, including automotive, aerospace and construction [53, 56, 57].

Table 2.1. Characteristics of typical structural adhesives adopted from [53].

Adhesive Class	Characteristics	
Acrylics	Good flexibility	Toxic
	Good peel and shear strengths	Flammable
	No mixing required	Low hot-temperature strength
Cyanoacrylates	Rapid room-temperature cure	Poor durability on some surfaces
	One-component system	Limited solvent resistance
	High tensile strength	Limited elevated-temperature resistance
Polyurethanes	Various cure times	Poor heat resistance
	Tough	Short pot life
	Excellent flexibility even at low temperature	Special mixing and dispensing equipment required
Phenolic	Good heat resistance	Brittle
	Good dimensional stability	Possibility of pollution due to formaldehyde as a curing agent
	Inexpensive	
Epoxy	High strength	Exothermic reaction
	Good solvent resistance	Short pot life
	Good heat resistance	Relatively low cost
	Modification of toughness by introducing additional substances	

An important advantage of epoxy adhesives is the capability of modifying their mechanical properties by the introduction of additives or fillers [56, 58]. Owing to the brittle behaviour of epoxies, toughening agents are commonly added as fillers to increase peel and shear fracture toughness and allow for greater energy absorption and resistance to impact loading. As a result, toughened epoxy adhesives are more resilient to the crack propagation progress [59]. The

typical approach to toughen epoxies includes adding thermoplastic resin, rubber, organic silicon resin, rigid particle and nano-particle fillers. Rubber fillers are often used to promote "silver streaks-nail anchor" and "silver lines-shear zone" mechanisms during mechanical loading [56], which improves the resistance to fracture during impact and bending loading. For adhesives with nano-particles, the particles act as crack arresting sites and as a result higher energy is required to propagate a crack compared to an adhesive without nano-particles [56].

In addition, adhesives can be classified as one component, two-component and multicomponent. A two-component epoxy is composed of a resin, with possible additives such as accelerators, fillers, plasticizers and resin modifiers, mixed with a hardener (or curing agent) [60]. Epoxy adhesives in liquid of film form can cure and solidify at various temperatures, which ultimately dictates the curing time. It is not ideal for high-volume production applications to use adhesives cured at room temperature due to the longer required curing times [61]. In the automotive industry, adhesives are commonly applied before painting a structure in order to simultaneously cure the paint and adhesive under elevated temperatures [62].

2.3 Adhesive Bonding of Fiber-Reinforced Plastic Composite Materials

2.3.1 Surface Treatment

For in-situ bonding of FRP parts, the thermosetting polymer matrix phase (e.g. epoxy) could be used as an adhesive to achieve a strong adhesion with the adherends due to chemical compatibility [63]. However, in the case of bonding fully cured FRP parts (i.e. secondary bonding), the FRP adherends must be treated to clean surface contaminants and create a chemically reactive surface [64]. Surface treatments can alter the surface of the adherend by

increasing surface tension, which improves the wettability of the surface. Surface tension can be increased by cleaning the adherend surface from contaminants, increasing surface roughness, or functionalizing the surface [65]. The choice of surface treatment method depends on the adherend material and specific adhesive. Several surface treatments have been considered for adhesively bonded FRP composite joints, including surface cleaning, use of a peel ply during processing, chemical treatment, plasma or laser treatment and abrasive sanding.

Mould release agents applied to the surface of tools to enable demolding of cured composite parts are one type of surface contaminant. Since these agents are designed to prevent chemical bonding, they must be removed prior to any subsequent bonding procedure [66]. Therefore, surface cleaning is commonly used to remove and clean the surface of the adherends from contaminants [53]. Effective cleaning solvents include methyl ethyl ketone, acetone, and methanol, the choice of which is based on the type of the adherend [53, 67, 68].

Peel plies are removable fabric layers used during the fabrication of prepreg FRP composite parts to control the part surface roughness and morphology (Figure 2.9) [21, 69]. The peel plies are stripped from the surface of the cured FRP part prior to bonding [70, 71]. Kanerva and Saarela [21] found that the use of peel plies altered the elemental composition and roughness of the surface of FRP composites. One common issue with conventional peel plies, specifically those coated with Teflon or silicone, is that residue remains on the surface of the composite part, which may weaken the joint strength if not cleaned prior to bonding [72]. Another disadvantage of peel plies is the need to layer the fabric onto the FRP layers during processing, which increases processing complexity [73]. In addition, peel plies cannot be used for FRP composites fabricated by liquid moulding processes such as RTM.

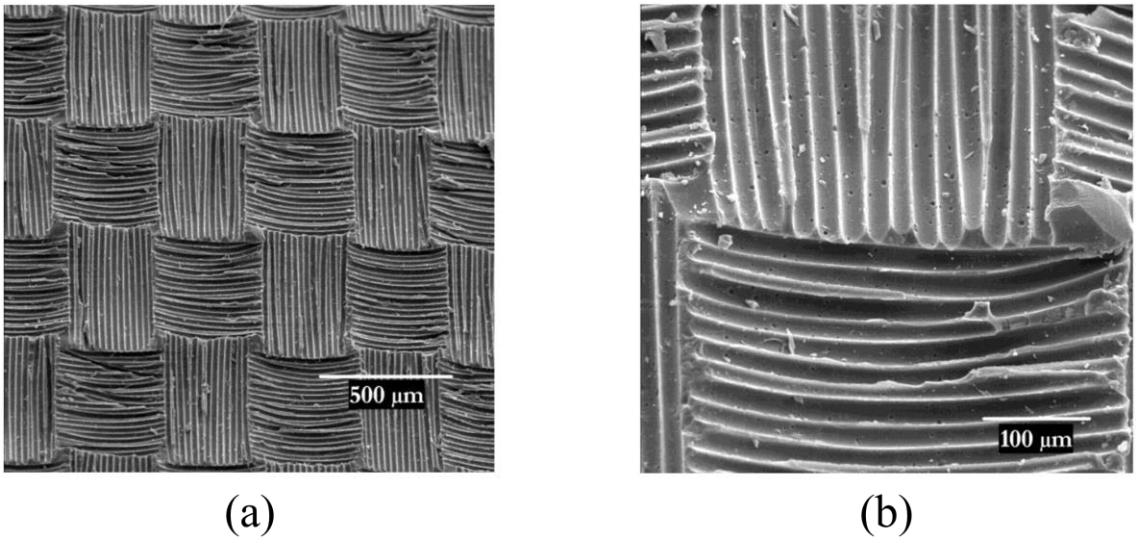

Figure 2.9. Surface morphology of a composite adherend after removal of a peel ply: (a) 50x, and (b) 200x magnification [71].

Chemical treatments are typically used for plastic materials to alter the physical and chemical properties of the surface [53]. Typically, the surface of an FRP composite part is washed with soap followed by immersion in a chemical treatment bath. The solutions for the chemical treatment may include an acid, base, oxidizing agent, chlorinating agent, or other active chemicals [74]. The chemical agent etches the surface of the FRP composite leading to increased and consistent surface roughness [75] (Figure 2.10). In the study by Martinez-Landeros et al. [76], the highest fracture toughness was observed for specimens treated by acid etching (Figure 2.11). They found that surface morphology was similar for the solvent cleaning and acid etching procedures. One problem with chemical etching treatments is that strong solutions such as acid, alkali and oxidants could pollute the environment and be harmful to

operators. Additionally, they could damage the matrix or reinforced fibres of FRP composite parts [77].

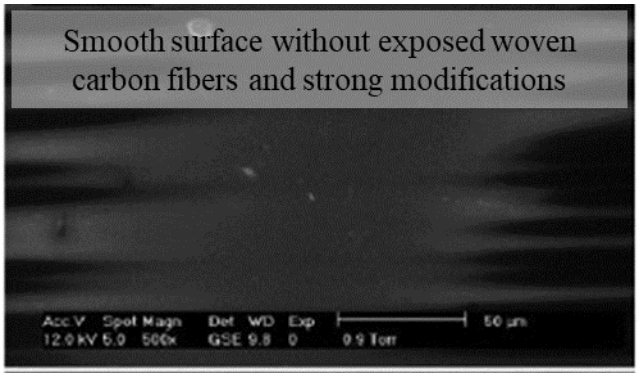

Figure 2.10. SEM image of surface morphology of an FRP composite adherend after an acid etching treatment [76].

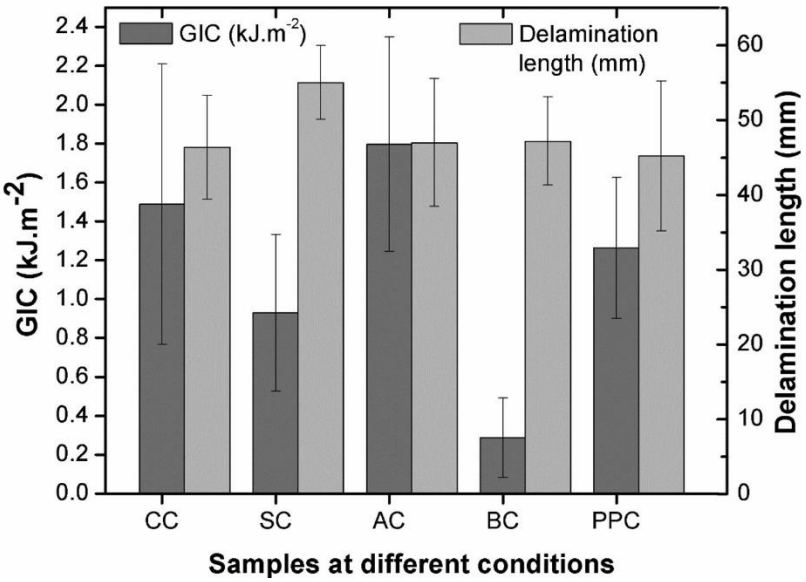

Figure 2.11. Fracture toughness and delamination length for specimens treated with different surface treatments including solvent cleaning (CC), sanding (SC), acid etching (AC), base etching (BC) and peel ply (PPC) [76].

Surface treatment with plasma is classified as an energetic technique that improves bonding by altering the surface energy of materials [78]. The surface of FRP composites are modified by interaction with the plasma beam causing different effects, including ablation or etching,

removal of organics, crosslinking of surface species and reconstructing the surface chemistry [79]. Zaldivar et al. [80] reported that the joint strength of CFRP single lap joint (SLJ) specimens bonded with Henkel Hysol EA 9394 epoxy paste adhesive was improved by increasing the number of atmospheric plasma treatment scans (Figure 2.12). Scanning electron microscopy (SEM) results also indicated that the degree of surface modification was influenced by the number of plasma treatment scans, where chemical effects, surface etching, and microstructural changes are possible (Figure 2.13). Pizzorni et al. [81] investigated the effectiveness of low-pressure plasma treatment on joint strength of CFRP SLJs and compared to the case when mechanical abrasion treatment was used. An improvement of up to 21% and 25% on joint strength was observed using air and oxygen as the gas, respectively, when compared to the mechanical abrasion treatment (Figure 2.14). In addition, statistical analysis with regards to the plasma treatment indicated that the selected intensity attributes more in the improvement on joint strength rather than other parameters such as duration of treatment.

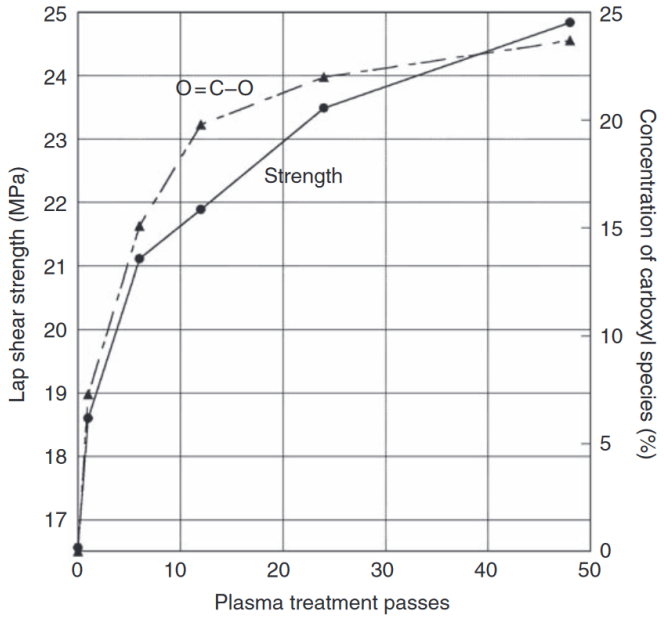

Figure 2.12. The joint strength of SLJs treated with different numbers of plasma passes [80].

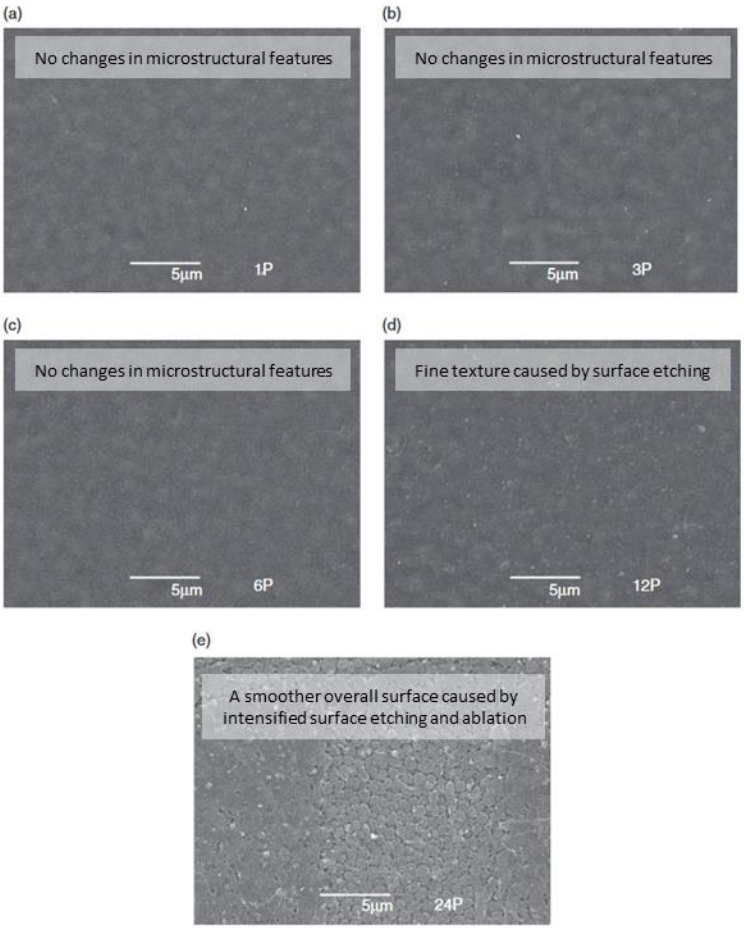

Figure 2.13. SEM photographs taken from the surface of CFRP treated with different plasma passes including (a) 1 pass, (b) 3passes, (c) 6 passes, (d) 12 passes, and (e) 24 passes adopted form [80].

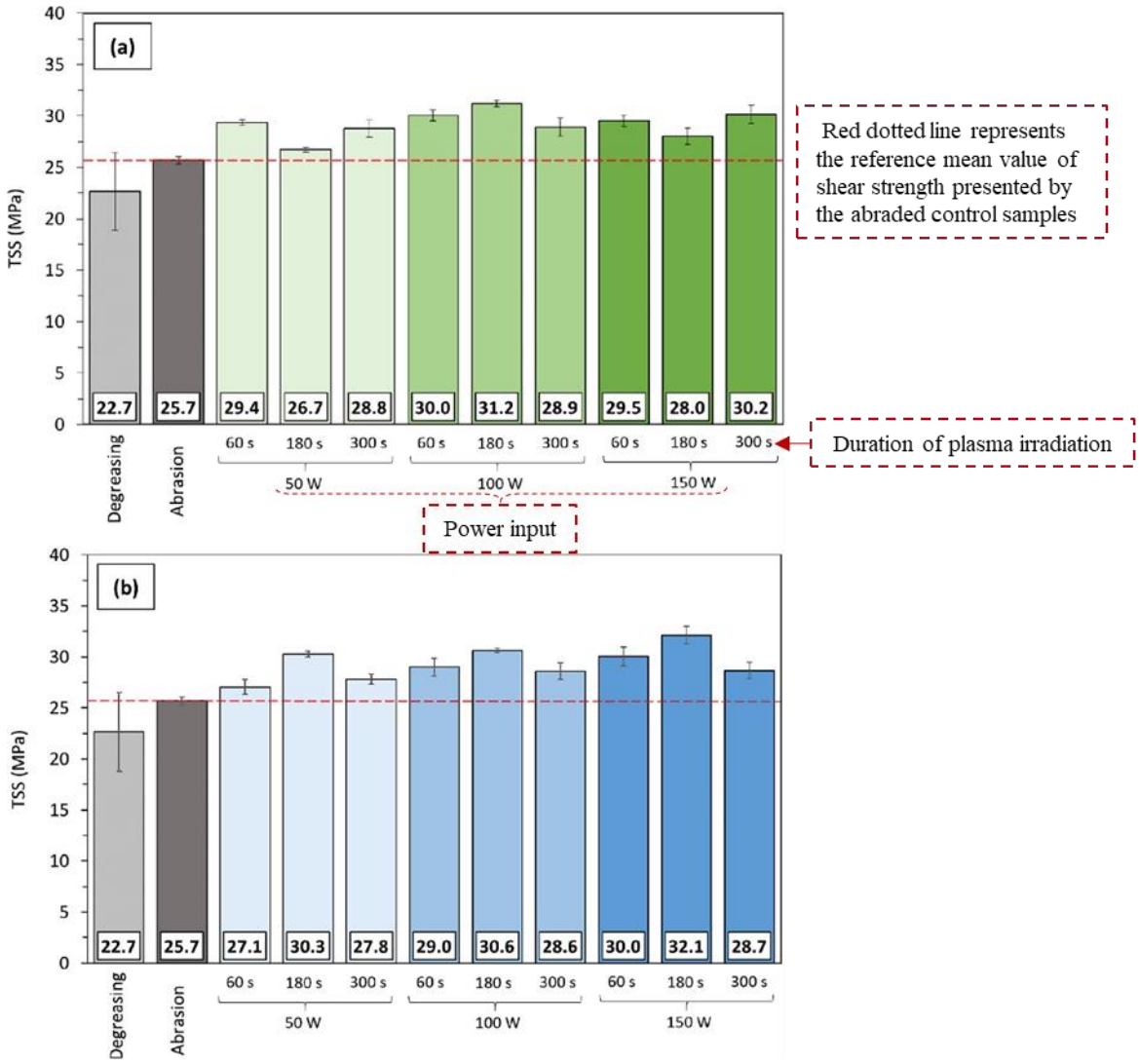

Figure 2.14. Single lap shear strength for various surface treatments including degreasing, abrasion and plasma treatment with different conditions, using (a) air and (b) pure-O_2 as process gasses (standard deviations of the associated measurements are displayed as error bars) [81].

Surface treatment using a laser is another energetic method used to prepare adherends. The common laser technologies used include carbon dioxide (CO_2) lasers, diode-pumped solid-state (DPSS) lasers operating near the infrared wavelength spectrum, frequency multiplied DPSS lasers with output in the ultraviolet wavelength spectrum, and excimer lasers [22]. In the study by Fischer et al. [22], the surface of a CFRP adherend was modified using laser

irradiation by effectively removing all contaminant residues as well as the desired amount of resin from the surface without impairing the fibres. SEM photographs of the treated CFRP surfaces revealed that at low laser intensity levels contaminants from the surface were removed and the bulk material remained unchanged (Figure 2.15a), while at higher intensity levels epoxy material was removed and the underlying fibres were exposed (Figure 2.15c). Depending on the laser wavelength, photochemical abrasion (i.e. breaking molecular bonds by single photons) could occur resulting in higher reactivity of the treated CFRP surface [82].

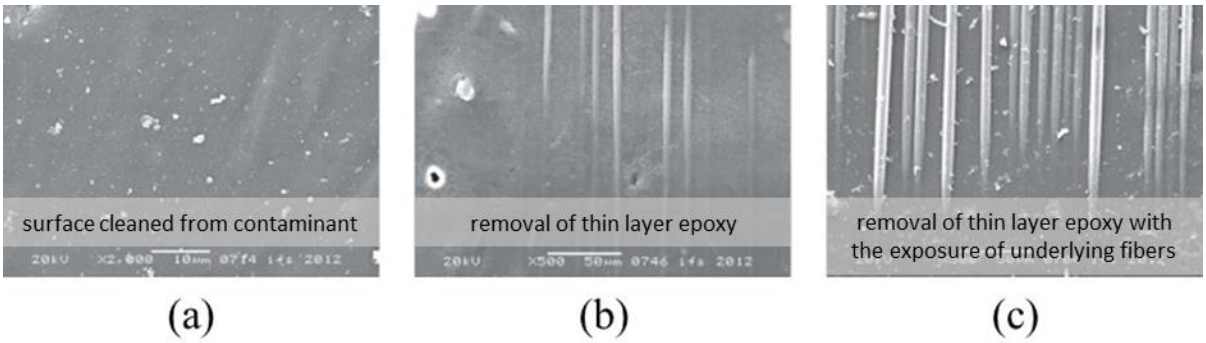

Figure 2.15. SEM photographs taken from CFRP surface treated with different laser intensity: (a) low laser intensity leaving no exposed fibres, (b) increased laser intensity causing fibre exposure, and (c) high laser intensity causing significant fibre exposure with no damage [22].

Sorrentino et al. [83] studied the effectiveness of carbon dioxide laser treatment on an adhesively bonded CFRP joint. The results of end notched flexural (ENF) tests revealed an improvement in fracture toughness of up to 80% for specimens treated using the carbon dioxide laser when compared to untreated specimens. Observation of the fracture surfaces indicated that using carbon dioxide laser treatment altered the failure mode from adhesive failure at the interface of adhesively bonded joints for untreated samples to stock-break failure. Rauh et al. [84] investigated the influence of UV-laser treatment on adhesively bonded CFRP single lap

joints. Observation of the fracture surfaces revealed that the failure mode changed from adhesive failure to failure at the fibre-resin interface in the top surface of adherends. The joint strength of UV laser-treated SLJ specimens was 100% higher when compared to that of the mechanically abraded SLJ specimens (Figure 2.16).

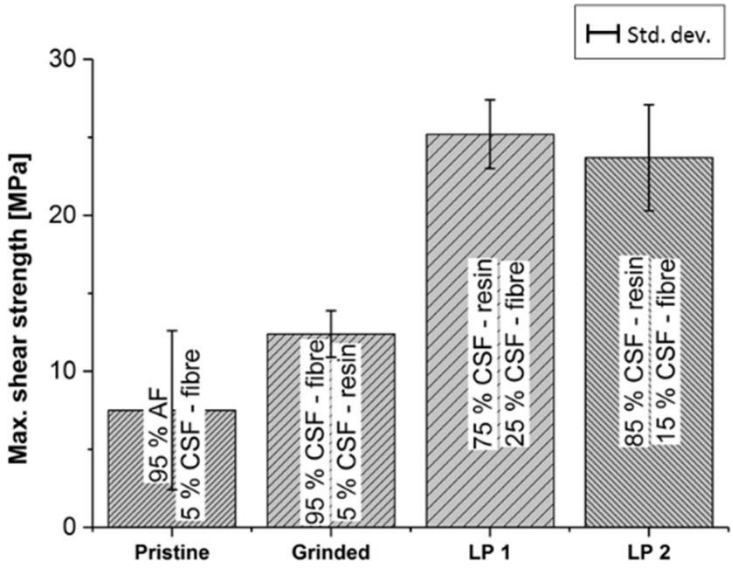

Figure 2.16. Single lap shear strengths for different surface treatments [84].

The use of excimer lasers as a surface treatment method has some limitations, including the emission of dangerous gasses to the environment and the high cost of the equipment and maintenance due to reaction of fluorine and chlorine [85]. In addition, both plasma and laser treatments are limited to treating small adherend surfaces, while the high cost of the apparatus may increase the overall fabrication cost as discussed by Shang et al. [86].

Grit-blasting is a surface treatment process that involves impacting the adherend surface with small particles under high velocities. Common types of grits are aluminum oxide, silicon carbide, sand and glass beads. Grit blasting is commonly applied to FRP composites and results

in changes to the surface chemistry and morphology. Changes in surface chemistry included the removal of mould release agents, while changes in surface morphology includes altering the surface roughness [87]. In addition, free radicals can be created and react with atmospheric oxygen to introduce oxygen containing functional groups on the surfaces of the composite adherends. Njuhovic et al. [23] reported that increasing blasting intensity led to a significant increase in surface roughness, which promoted mechanical anchoring effects on the surface of the CFRP adherend. SEM photographs indicated that grit blasting produced a non-uniform surface structure characterized by dimples and furrows, where higher blasting time led to an increased removal of epoxy resin at the outermost layer such that the carbon fibres were exposed and damaged (Figure 2.17). The experimental results indicated an increase in peel strength for the CFRP adherends with higher surface roughness, owing to greater interlocking effects. The peel strength of the adhesively bonded metalized CFRP-SLJ treated by grit blasting was 10X higher compared to untreated specimens (Figure 2.18). Chamochin et al. [88] investigated the effectiveness of various surface treatments on adhesively bonded FRP joints and found that an improvement in surface energy was achieved using grit blasting and plasma treatments. Wedge tests and single lap shear tests revealed an improvement in joint strength and durability, where grit blasting was identified as the most effective surface treatment (Figure 2.19).

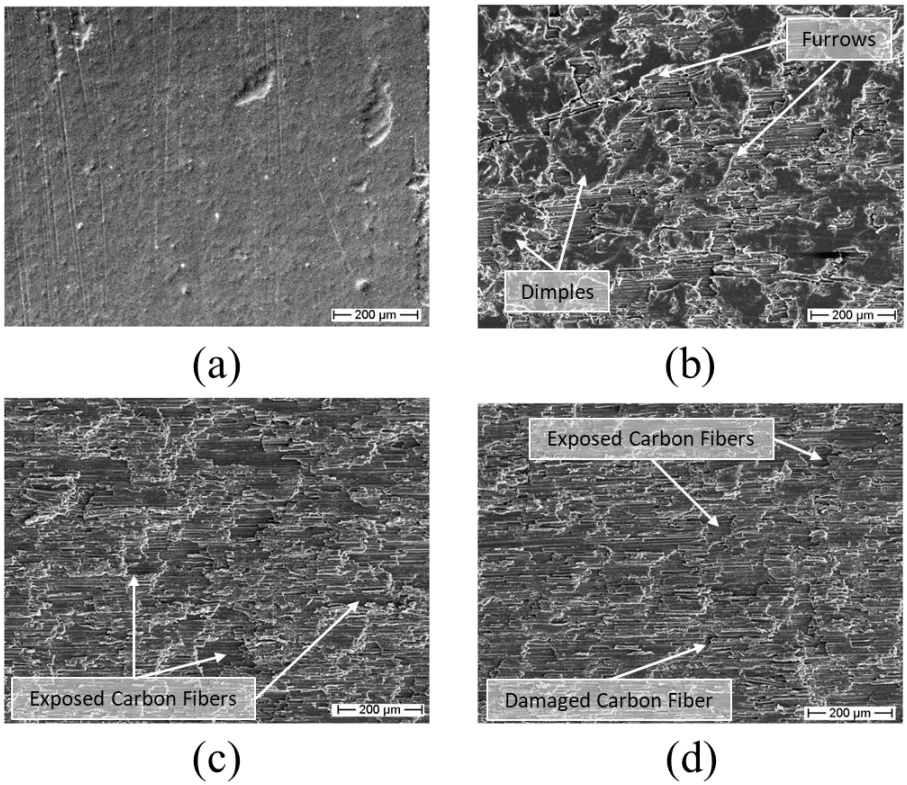

Figure 2.17. SEM images of (a) un-treated CFRP adherend and grit blast treated adherends with different blasting times including (b) 3 s, (c) 6 s and (d) 9 s adopted from [23].

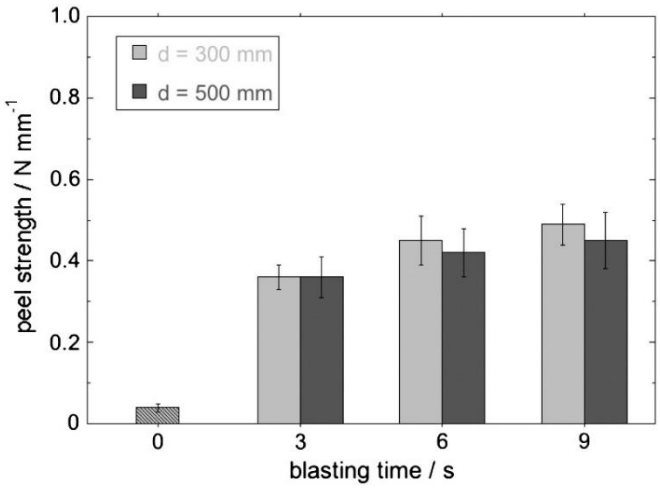

Figure 2.18. Peel strength of adhesively bonded metalized CFRP-SLJ treated by grit blasting with different blasting times and nozzle distances [23].

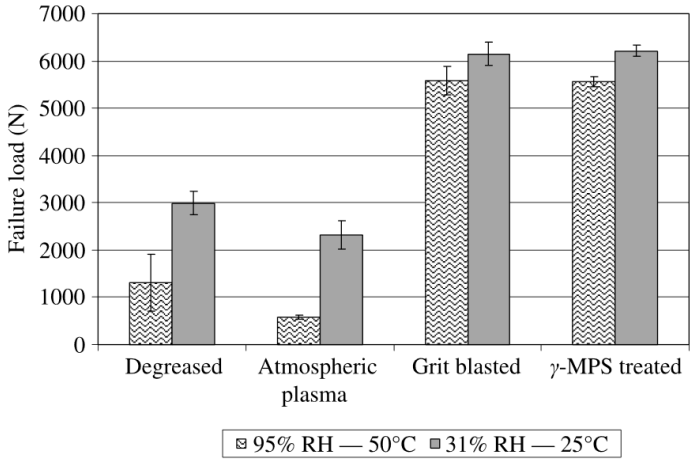

Figure 2.19. Failure load of single lap joints with different surface treatments after exposure for 30 days [88].

Abrasion surface treatments involve sanding the adherend surface with an abrasive material, which removes surface contamination, increases surface energy and increases surface roughness. However, using an abrasive with large grit size may increase the amount of epoxy resin removed, resulting in fibre damage and decreased bond performance for FRP adherends. In the study by Zaldivar et al. [89], SEM images revealed the sensitivity of the abrasion affected zone on the FRP composite surface to the abrasive grit size, where an increase in abrasive grit size led to a larger abrasion damage zone (Figure 2.20).

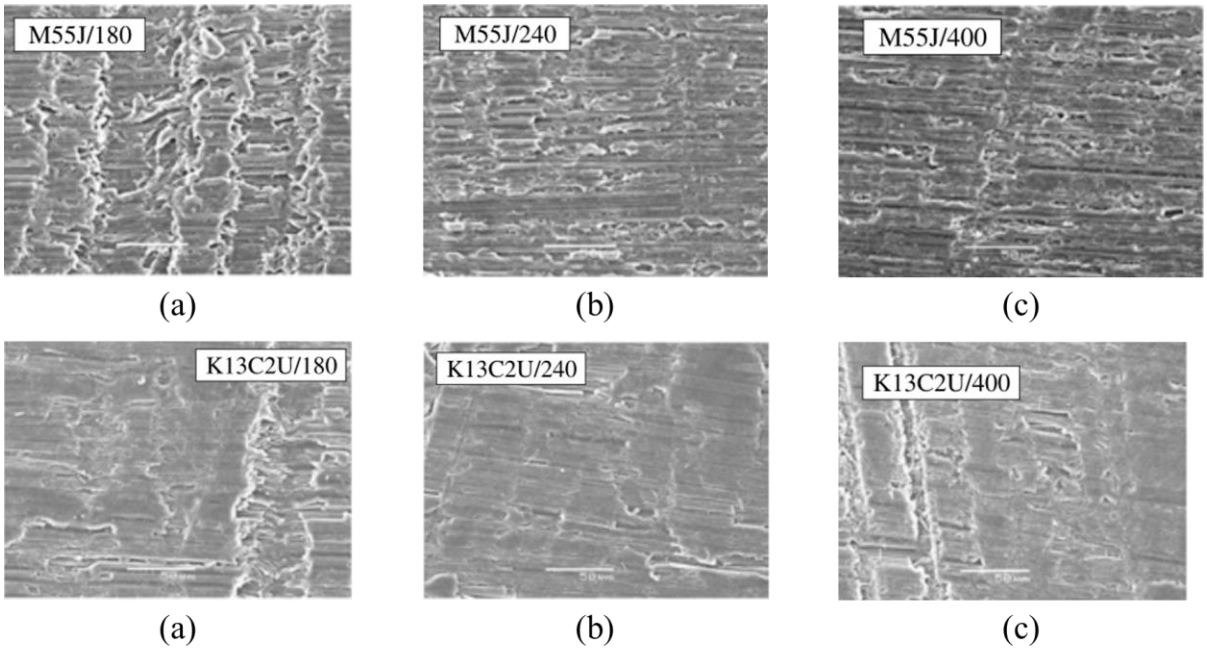

Figure 2.20. SEM images of M55J and K13C2U composite surfaces treated with sandpaper with different abrasive grit sizes including: (a) 180 grit, (b) 240 grit and (c) 400 grit adopted from [89].

Yang et al. [90] studied the influence of sandpaper grit size on the performance of adhesively bonded CFRP joints over the range 60–800 grit, where an optimum joint strength was obtained for the surfaces abraded with 220 grit sandpaper. They also found that abrading along the direction perpendicular to the fibre direction resulted in removal of the matrix at the surface. Abrading parallel to the fibre direction also led to removal of the epoxy layer at the surface of the adherend, resulting in exposure of fibres along the grinding direction. However, when the adherends were sanded along random directions the surface was completely polished and loose fibres on the surface were removed, which resulted in the highest joint strength.

Park et al. [24] investigated the effectiveness of abrasion with sandpaper, grit blasting and use of a peel ply as surface treatments on the lap shear strength of CFRP secondary bonded

joints. The lowest static joint strength was observed for the SLJ treated with sandpaper, which was due to the potentially low polar component of surface energy. However, in cyclic fatigue testing the highest static strength retention at one million cycles was achieved for specimens treated with sandpaper (Figure 2.21). Observation of the fracture surfaces indicated that the failure mode was predominantly cohesive failure during static loading and thin layer cohesive failure for high cycle fatigue loading.

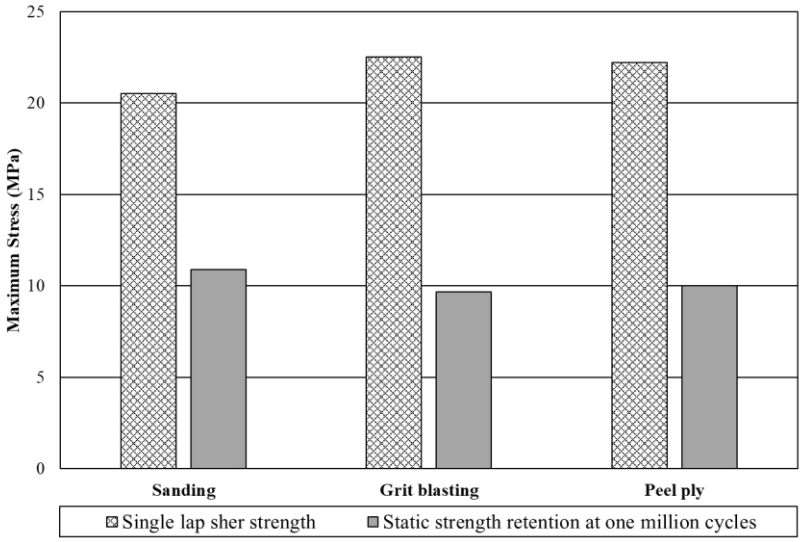

Figure 2.21. Single lap joint strength under static and fatigue loading with different surface treatments [24].

2.3.2 Joint Configurations

Joints design is challenging for composite structures, owing to the fact that these discontinuities within the structure are load transfer points between parts [91]. Different types of joint configurations that can be used for the design of composite structures include single lap joint, double lap joint, and butt joints, among others (Figure 2.22). Owing to its simplicity, the single lap shear test is commonly used to determine the effectiveness of surface treatment

on joint strength and to assess the joint performance of similar and dissimilar materials [92]. There are various ASTM standards for single lap shear tests based on different types of adherends and adhesives. For instance, ASTM D1002-10 (Figure 2.23a) and ASTM D3165-07 (Figure 2.23b), are used to assess the joint strength and compare engineering shear stress at failure for adhesively bonded metal specimens. Backing plates are recommended for specimens in ASTM D3165-07 to align the loading axis with the overlap area, thus reducing the bending load and increasing the stiffness of the specimen. ASTM D5868-01 is used to determine the joint strength and compare engineering shear stress at failure for adhesively bonded FRP adherends (Figure 2.23c). However, since in ASTM 5868-01 backing plates are not specified, the test specimen can be modified with backing plates (Figure 2.23d).

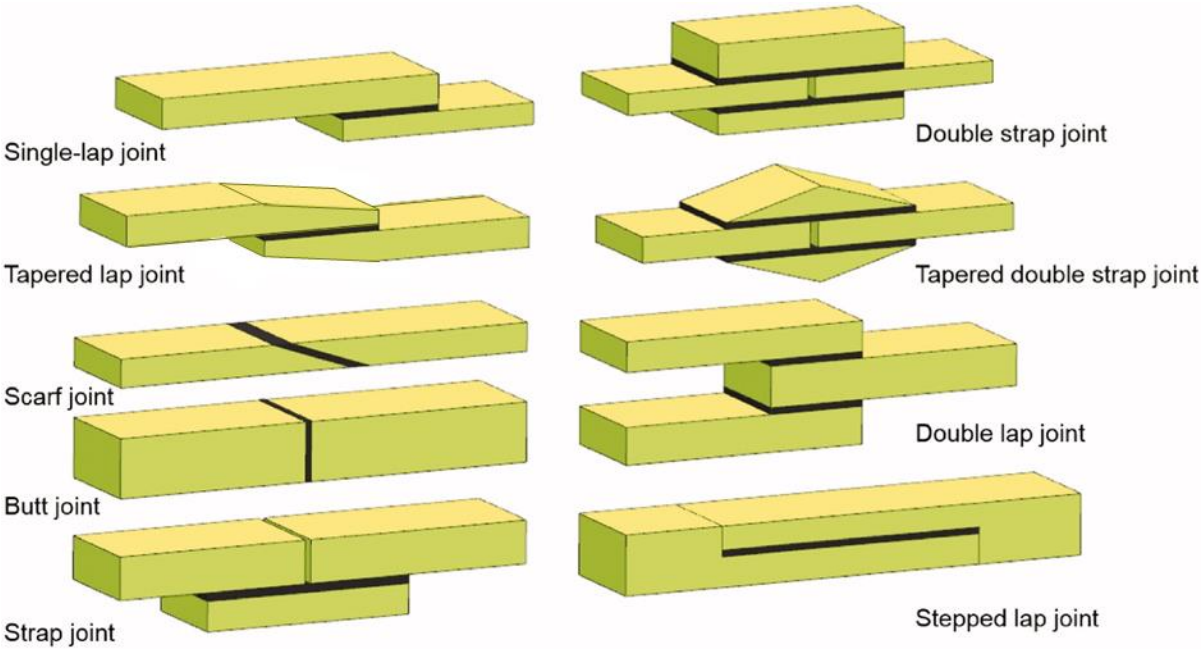

Figure 2.22. Adhesively bonded joints configurations [93].

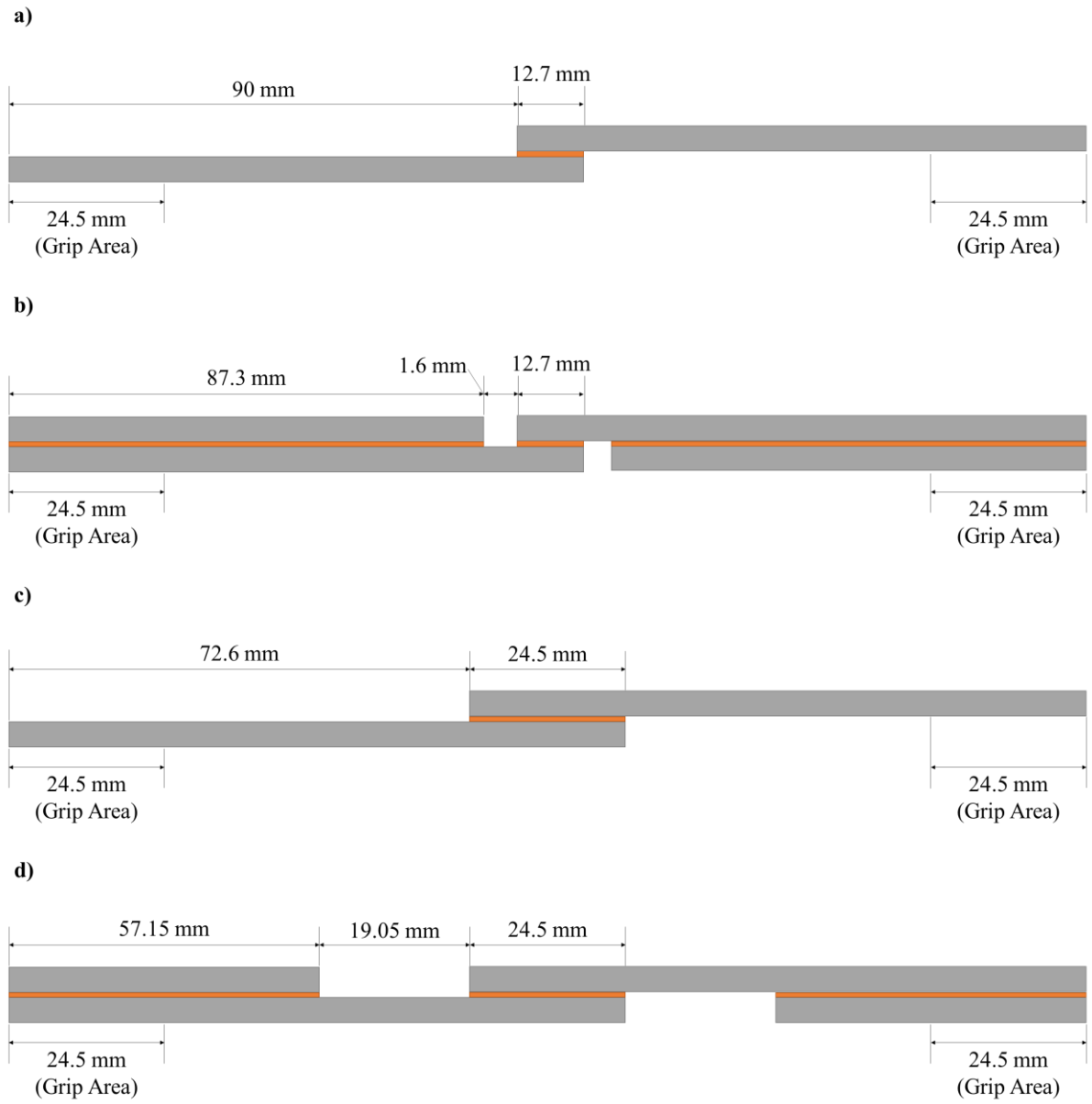

Figure 2.23. Different types of single lap shear specimens based on standards: (a) ASTM D 1002-10, (b) ASTM D 3165-07, (c) ASTM D 5868-01, (d) Modified ASTM D 5868-01.

For a particular adhesively bonded joint configuration and type of load, the joint strength depends on the stress distribution within the joint, which in turn depends on the mechanical properties of the adhesive and adherend [86, 91] as well as the joint geometry. Important

geometrical characteristics that influence the joint strength include the overlap length [94, 95], bond-line thickness [96] and other joint features (i.e. adherend recessing, adherend and adhesive chamfering) [86, 97]. Studies have reported that the joint strength of adhesively bonded SLJs increases with increasing overlap length [94] and decreasing bond-line thickness [96]. Moya-Sanz et al. [97] studied the effect of adherend recessing and adherend and adhesive chamfering on the joint strength of FRP composite SLJs. Chamfering of the adherends and the adhesive contributed to reducing the eccentricity of the load and the prevention of stress concentrations at the end of the overlap region, leading to an improvement in joint strength. Moreover, spew fillets (i.e. excess of adhesive squeezed out of the lap region during bonding) provided smoother stress transition at the end of the overlap region, resulting in reduced stress concentration [98]. Goglio et al. [99] reported that the size and shape of spew fillets could influence the peak stress at the end of the overlap region in single lap joints.

In adhesively bonded composite joints, the joint strength is also influenced by the stacking sequence of the adherend. Hart-Smith [100] analyzed the influence of laminate bending stiffness on the stress distribution along the overlap region in adhesively bonded composite single lap joints. Joint efficiency ($\sigma_{avg}/\sigma_{max}$) was introduced as a ratio of average stress in the overlap region over the peak stress at the end of overlap region. The analytical results indicated that laminates with 0° plies at the bonded surface exhibited greater joint efficiency due to the increased laminate bending stiffness. Similarly, Demiral et al. [101] found that single lap joints comprising composite adherends with higher bending stiffness resulted in increasing the joint strength. Kupski et al [102] observed that adherends comprising laminates with higher bending stiffness led to higher loads at damage initiation in FRP single lap joints. In addition,

they found that for composite adherends with similar bending stiffness, SLJ specimens consisting of adherends with higher off-axis ply angle at the bonded surface led to an increase in final failure load due to promotion of progressive crack propagation inside the composite rather than in the adhesive. Similarly, Purimpat et al. [103] reported that for single lap joints with different FRP laminate adherends with constant stiffness, the adherends containing surface plies with larger biased angles caused more complex crack paths and an increase in the joint strength by up to 30%. Ozel et al. [104] showed that the joint strength of CFRP single lap joint consisting of adherends with $[0/\pm45/90]_4$ stacking sequence increased by 48%, 62%, and 123% when compared to adherends with $[0]_{16}$, $[0/90]_8$, and $[\pm45]_8$ stacking sequences, respectively. This in part contradicts the conclusions by Hart-Smith et al [100], Demiral et al. [101] and Kupski et al. [102], indicating that bending stiffness is not the only critical parameter that influences joint strength. Meneghetti et al. [105] reported that the fatigue strength of CFRP single lap joints comprising adherends with $[45/0_2]_s$ and $[45_2/0]_s$ stacking sequences were higher than that of a single lap joint consisting of adherends with $[0]_6$ stacking sequence.

2.3.3 Failure Modes for Single Lap Joint

Failure modes of adhesively bonded FRP SLJs are influenced by the quality of the adhesion at the adherend/adhesive interface, surface conditions (e.g. contamination and different surface treatments), joint geometry and configurations such as fillet and bond line thickness, environmental conditions, stacking sequence of the composite adherend and loading conditions. Characterizing the failure mode of FRP SLJs provides a better insight into the properties of the adhesive and joint performance [68].

According to the study by Banea et al. [68], there are six common modes of failure for adhesively bonded composite joints including adhesive (interfacial) failure, cohesive failure, thin-layer cohesive failure, fibre-tear failure, light-fibre-tear failure and stock-break failure (Figure 2.24). Adhesive failure occurs at the interface between the adhesive and the adherend and typically indicates low adhesion caused by an ineffective surface treatment (e.g., see study by Fischer et al. [82]). Cohesive and thin-layer cohesive failure modes comprise fracture within the adhesive layer and are desirable since the maximum strength of the adhesive can be utilized and the lowest corresponding variability in joint strength is achieved [53]. Cohesive failure is indicative of a strong adhesion between the adhesive and adherends [82]. The high through-thickness stresses at the end of the overlap region are the main concern in adhesively bonded FRP composite joints, due to the relatively low through-thickness strength of most composite materials [68] (Figure 2.25). As a result, FRP composite joints made with high strength adhesives are more likely to fail within the plies of the FRP adherend, leading to fibre-tear or light-fibre-tear failure modes. Fibre-tear failure mode can also be observed in cases where the surface treatment caused local damage to the adherend [82]. Finally, a stock-break failure occurs when the applied load supported by the adherend exceeds the strength of the FRP composite material.

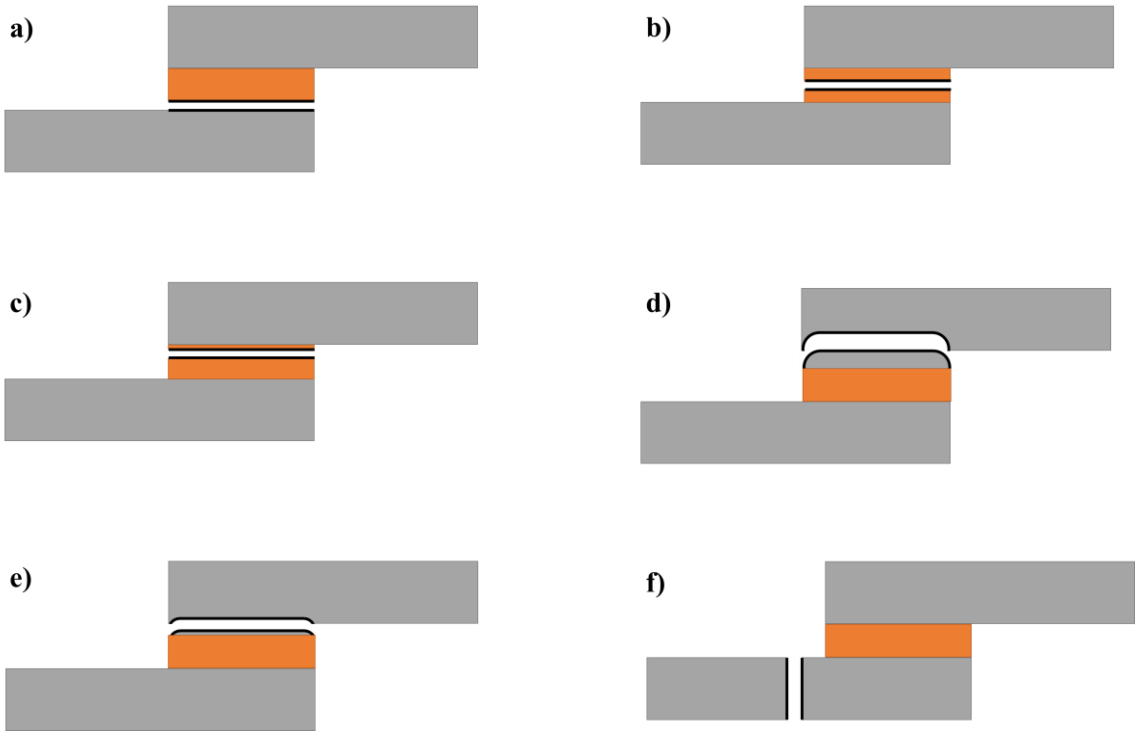

Figure 2.24. Different failure modes occurred in adhesively bonded composite joints: (a) adhesive (interfacial) failure, (b) cohesive failure, (c) thin-layer cohesive failure, (d) fibre-tear failure, (e) light-fibre-tear failure and (f) stock-break failure.

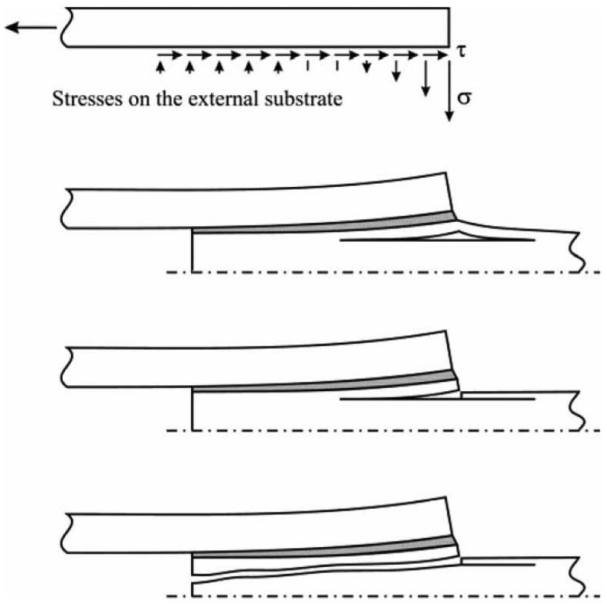

Figure 2.25. Failure occurred in adherend due to transverse (through the thickness) stresses [68].

2.3.4 Summary

Despite several important studies that have been conducted to determine the influence of different parameters (e.g., surface treatment, adherend laminate stacking sequence, etc.) on the joint strength and failure mode of FRP-SLJ, inconsistent findings on the impact of FRP laminate stacking sequence on adhesively bonded joint strength have been reported. Furthermore, a survey of the literature has revealed that there are no in-depth studies that have investigated the performance and behaviour of adhesively bonded FRP adherends comprised of NCF/epoxy material systems.

2.4 Fracture Characterization of Adhesively Bonded Joints

2.4.1 Testing Methods

Fracture mechanics concepts are widely used to characterize the fracture behaviour of adhesively bonded joints. The three modes of fracture include opening, sliding and tearing, which are denoted as Modes I, II and III respectively (Figure 2.26). Fracture Modes I and II are typically considered when assessing the fracture behaviour of adhesively bonded joints [106].

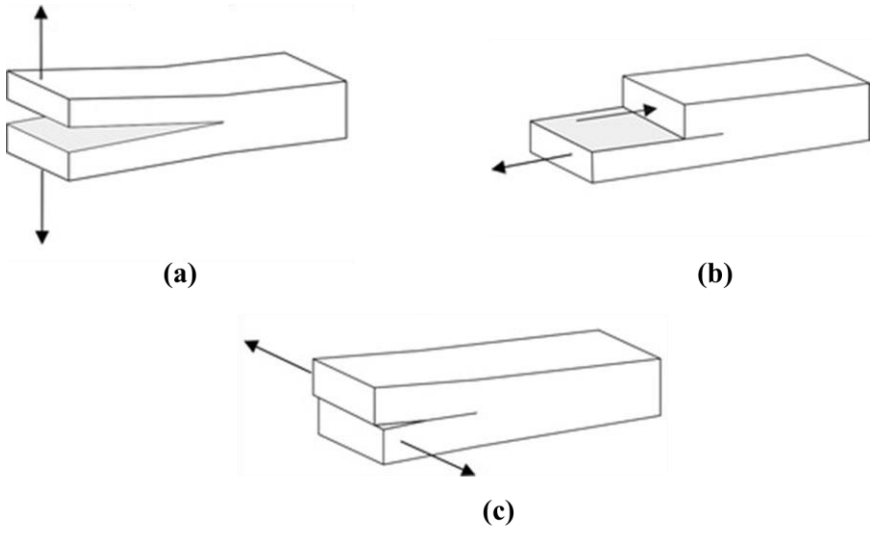

Figure 2.26. Different fracture modes: a) Mode I (opening), b) Mode II (sliding), c) Mode III (tearing) [106].

Fracture criterion based on a stress intensity factor or the strain energy release rate (SERR) represent the two basic criteria in fracture mechanics [107]. The energetic criteria relies on the assumption that the propagation of an internal defect will occur when the available energy at that defect tip (G, SERR), caused by the applied load, is equal to or higher than the energy required for the crack to propagate (G_c, critical SERR) [108]. For adhesively bonded joints, it is common that the applied load causes a simultaneous combination of peeling and shear stresses that drive crack propagation (i.e., Modes I and II), which requires a mixed-mode criterion to analyze damage propagation. It is difficult to accurately calculate the stress intensity factor values when the crack propagates near the interface of adhesively bonded joints; hence, in mixed-mode loading the energetic criterion based on the SERR is more appropriate [109].

Double cantilever beam (DCB) and tapered double cantilever beam (TDCB) are conventional test methods used to obtain the Mode I critical SERR (G_{Ic}) for an adhesive. A

typical DCB specimen consists of two bonded adherends with the same length/width and constant thickness (Figure 2.27a). In contrast, the bonded adherends for TDCB specimens have a wedge shape with a region of constant height on one end and a tapered region on the opposite end where height increases along the direction of crack propagation (Figure 2.27b). For both test methods, the bonded adherends are loaded in tension and the critical strain energy release rate is calculated using the Irwin-Kies equation [110]. FRP adherends for DCB test specimens are easily manufactured from flat panels, while the fabrication of FRP adherends for TDCB test specimens are challenging due to the tapered geometry. Additionally, three data reduction methods for the determination of G_{Ic} are available for DCB tests, including modified beam theory (MBT), compliance calibration (CC), and modified compliance calibration (MCC) methods (ASTM D5528-0). However, a limitation of the DCB test is the difficulty in defining other properties required to calibrate the entire traction-separation law for a cohesive zone model, including initial stiffness and peak traction. Accordingly, it was concluded that an additional test method is required to obtain the initial stiffness and peak traction [111, 112], which is often accomplished by conducting a butt-joint test [113]. More recently, the rigid double cantilever beam (RDCB) test was proposed by Dastjerdi et al. [114] to directly measure the critical SERR and other cohesive properties of soft biological adhesives with a single test (Figure 2.28a). Watson et al. [115] enhanced the RDCB specimen geometry and presented an improved analysis method for testing toughened structural adhesives.

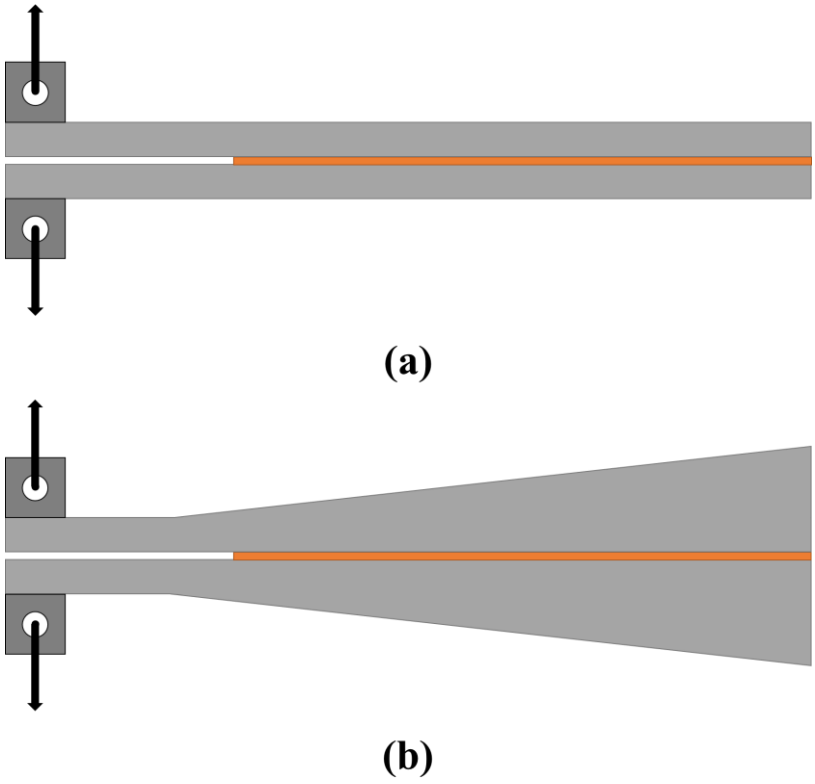

Figure 2.27. Test specimens used for Mode I fracture behaviour characterization of adhesively bonded joints: (a) double cantilever beam (DCB) (b) tapered double cantilever beam (TDCB).

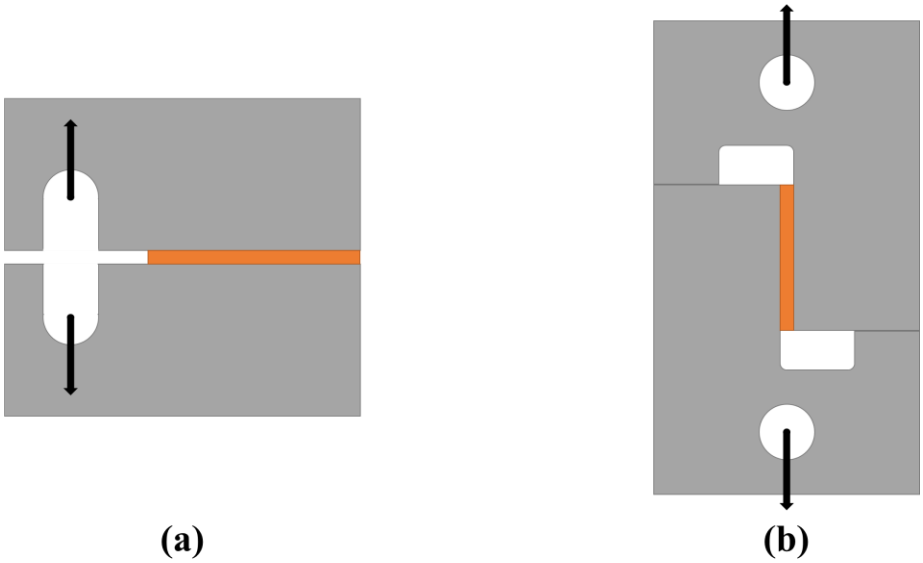

Figure 2.28. RDCB test specimen geometries developed to characterize: (a) Mode I and (b) Mode II fracture behaviour.

Several test methods have been developed to determine the Mode II critical strain energy release rate (G_{IIc}) of an adhesive, including end notch flexure (ENF), end-loaded split (ELS) or the four-point end-notched flexure (4ENF) test (Figure 2.29). Some problems were observed with the variability of calculated G_{IIc} using the ELS test due to the complexity of data reduction brought about by the boundary conditions [116]. The 4ENF involves a sophisticated test setup and the results are affected by friction at the pre-crack zone, resulting from the loading [117]. Therefore, the ENF test is the most common test used to characterize Mode II fracture behaviour of adhesively bonded joints [118]. In addition, a new test setup using bonded shear samples (BSS) was developed to characterize the Mode II fracture behaviour under pure shear, which enables measurement of the critical SERR and other cohesive properties (Figure 2.28b) [119].

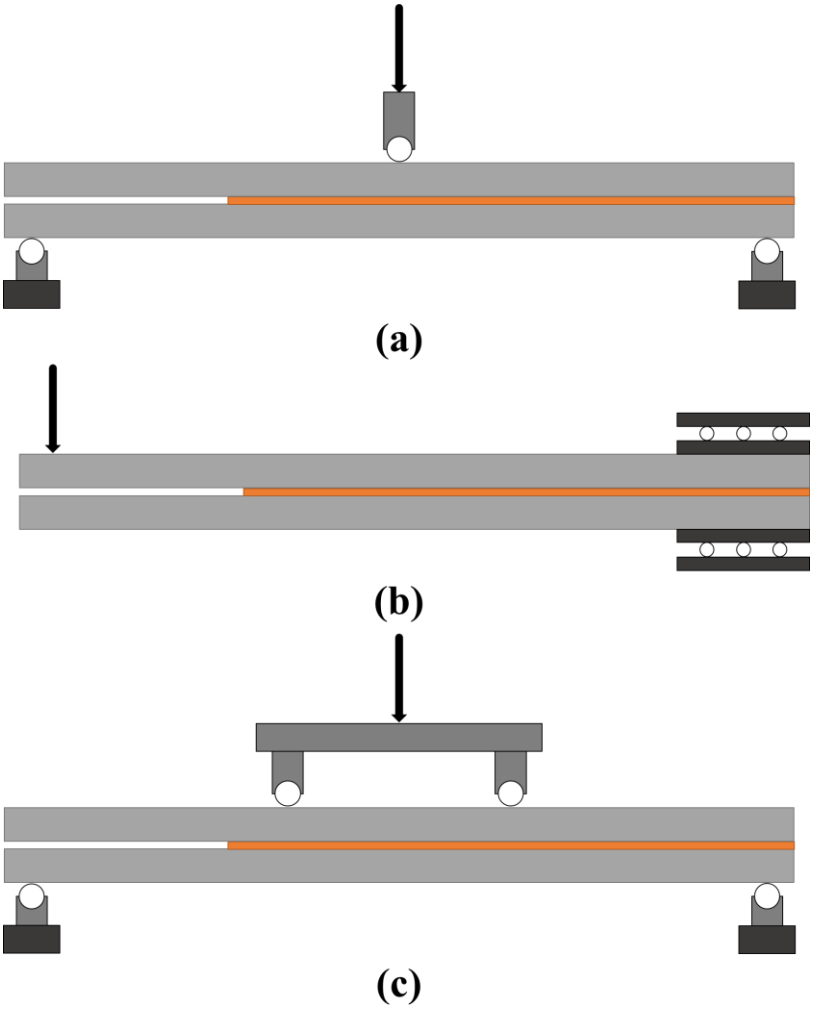

Figure 2.29. Test methods used for Mode II fracture behaviour characterization of adhesively bonded joints: (a) end notch flexure (ENF), (b) end-loaded split (ELS), and (c) four-point end-notched flexure (4ENF).

2.4.2 Influence of Bond-Line Thickness and Loading Rate on Fracture Behavior

Several studies have investigated the effect of different parameters on the fracture behaviour of adhesively bonded FRP composite joints, including the adhesive bond-line thickness and the loading rate. Marzi et al. [120] reported that the Mode I fracture energy for a DCB test specimen increased with an increasing adhesive bond-line thickness up to a plateau at 1 mm

thickness, while further increase in the bond-line thickness beyond 2 mm caused a reduction in the fracture energy. They also reported that the Mode II fracture energy for ENF test specimens increased with increasing adhesive bond-line thickness. Banea et al. [27] observed that the Mode I fracture energy increased with increasing bond-line thickness for a structural polyurethane adhesive (Figure 2.30). Similar observations were reported by Lißner et al. [121] and Waston et al. [119].

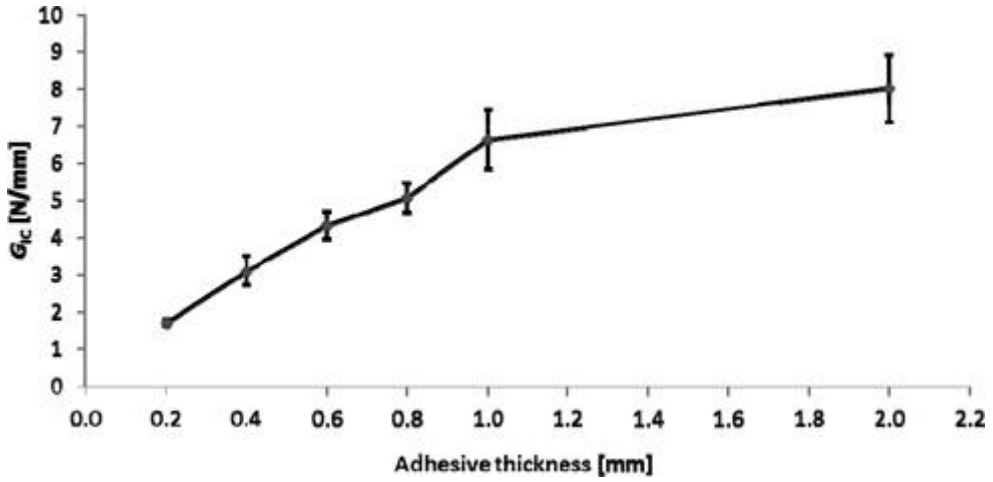

Figure 2.30. G_{Ic} as a function of adhesive bond-line thickness adapted from [27].

Ravindran et al. [122] investigated the Mode I fracture behaviour of adhesively bonded carbon/epoxy composite joints under a range of loading rates. It was observed that for the epoxy-based adhesive film, as the loading rate increased the fracture energy reduced by 30–53% when compared to the quasi-static fracture energy. Blackman et al. [28] reported similar results for CFRP DCB test specimens over the range of loading rates from 1×10^{-5} m/s to 15 m/s (Figure 2.31). On the contrary, some studies [29, 113, 123] reported that the fracture energy increased with increasing loading rate. For example, Georgiou et al. [29] observed an increase

in the fracture energy from 5 kJ/m^2 to 7.5 kJ/m^2 for DCB specimens with loading rates of 1 mm/min 60 mm/min, respectively.

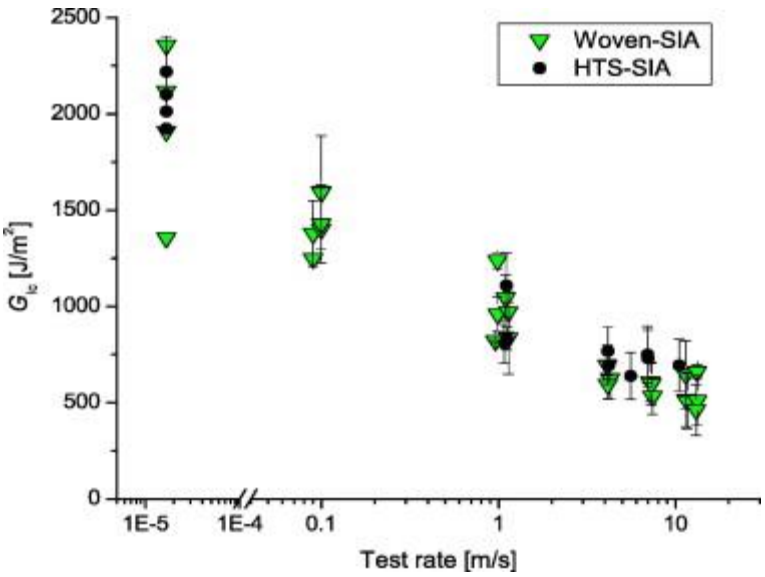

Figure 2.31. G_{Ic} as a function of loading rate for the adhesively bonded joints comprised of HTS (Triangles) and woven (Circles) adherends [28].

2.4.3 Cohesive Zone Modelling

A common approach used for analyzing the fracture behaviour of adhesively bonded joints is a cohesive zone model (CZM), which uses a traction-separation law to represent the cohesive properties of the joint. CZM can be embedded in a finite element (FE) framework, which allows modelling the fracture behaviour in a wide range of materials and structures including adhesively bonded joints [124]. However, the traction-separation law parameters, including initial stiffness, peak traction and SERR, must be precisely determined [25].

CZMs are established between paired nodes of cohesive elements and based on the concepts of stress and fracture mechanics, which can be applied by using local or continuum approaches. For a local approach (Figure 2.32a), fracture is confined to a zero volume line or surface

representing fracture between materials, e.g. between the adhesive and the adherend [125]. For a continuum approach (Figure 2.32b) fracture is modelled within a thin bulk layer of constant thickness material (e.g., cohesive failure for adhesively bonded joints), which is represented using solid cohesive elements [126].

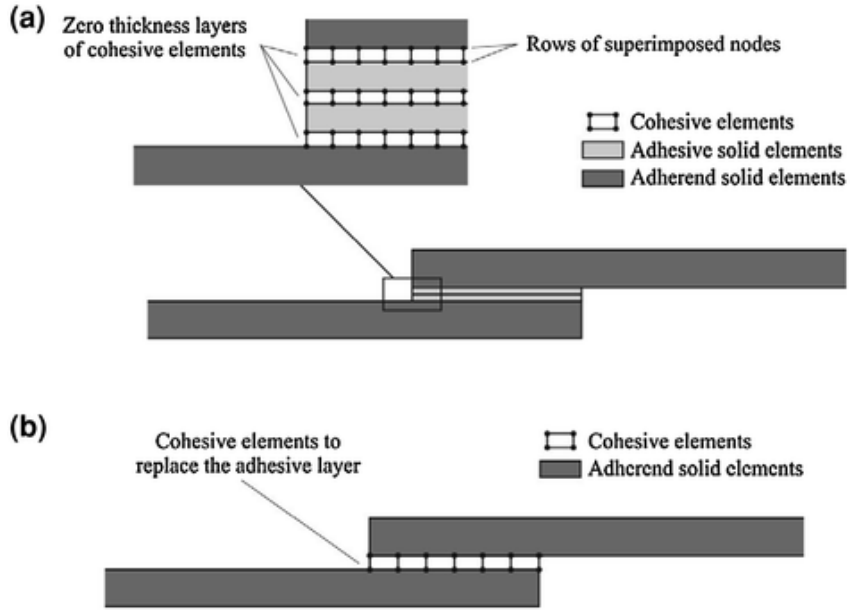

Figure 2.32. Different approaches to simulate the fracture behaviour of adhesively bonded joints: (a) local approach and (b) continuum approach [25].

Owing to its simplicity, the continuum approach is commonly used to simulate Mode I and Mode II fracture behaviour of adhesively bonded joints [127]. A single layer of cohesive elements provides the representative response of the entire adhesive layer (Figure 2.32b) [128]. Traditional material constitutive models, which require a relationship between stress and strain, determine the microscopic phenomena on the origin of failure. Traction-separation (stress-displacement) descriptions in the normal (Mode I) and shear (Mode II) directions provide a macroscopic reproduction of fracture along a given path. Bilinear, exponential and trapezoidal

traction-separation responses (Figure 2.33) are the most commonly used for representing fracture of adhesively bonded joints.

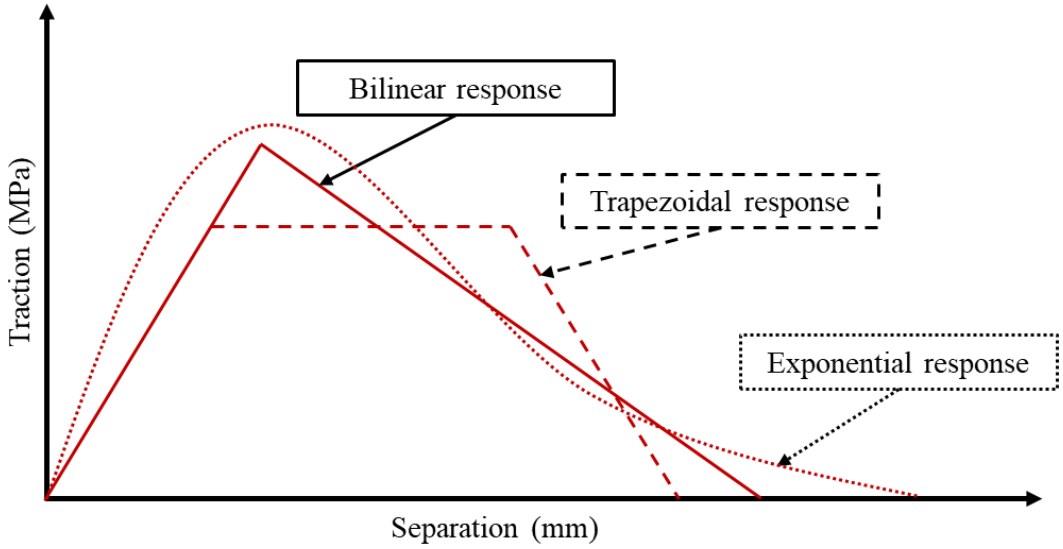

Figure 2.33. Different shapes of pure mode CZM laws**.**

A CZM law requires definition of the fracture energy (i.e., critical SERR, G_c) along the fracture path, which is the area under the traction-separation curve (Figure 2.34). In addition, the cohesive strength (i.e., peak traction, t°) representing the onset of damage and stress softening and the displacement at peak traction (δ°), which is related to the initial stiffness ($E = t^o/\delta^o$), must be defined. The displacement at final failure (δ^f) is defined using the critical SERR, G_c (Figure 2.34).

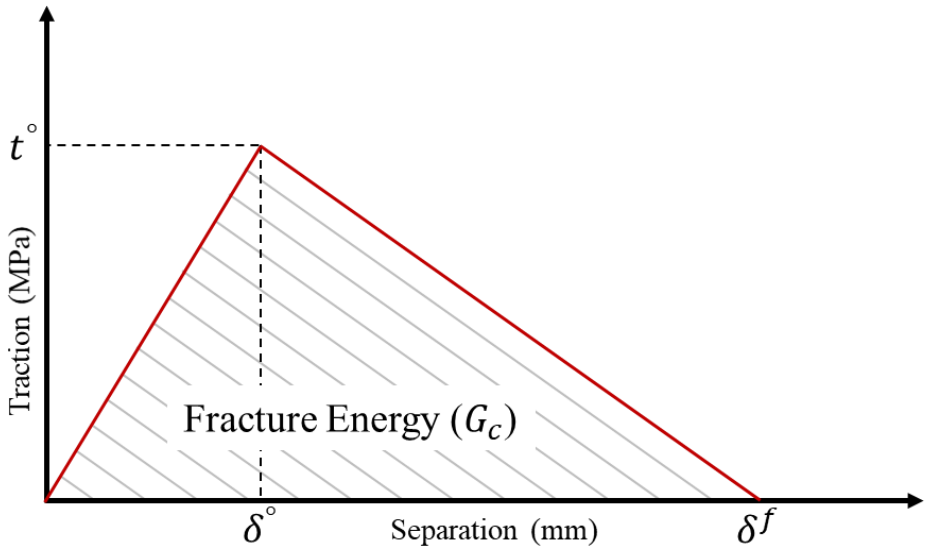

Figure 2.34. Bilinear traction-separation response and the required parameters for the definition of CZM law.

The definition of CZM parameters requires careful calibrations using experimental data and respective validation to accurately simulate the failure process. A few data reduction methods have been used for this purpose, including the property determination technique, the direct method and the inverse method [25]. The inverse method involves an iterative curve fitting analysis between experimentally measured force-displacement data and that predicted by a representative finite element analysis. The inverse characterization of CZM parameters is applied individually for each tested specimen to account for slight geometry variations between specimens [128]. Fracture energy (G_c) is required as input for the CZM along with approximate values for peak traction and initial stiffness of the traction-separation curve. The CZM parameters are varied and a trial and error iterative procedure is performed until the predicted force-displacement response match that of the experiment [129].

Chapter 3: Experimental Methodology

In this chapter, details of the CFRP and adhesive materials used in this study are presented in Section 3.1. The single lap shear tests that were used to assess the surface preparation and joining technique are discussed in Section 3.2. Double cantilever beam tests that were employed to characterize the Mode I fracture behaviour of adhesively bonded joint are described in Section 3.3.

3.1 Materials

The adherends used for this project were carbon fibre/epoxy laminates. A unidirectional non-crimp fabric containing 5 mm wide tows with 50,000 carbon fibre filaments, and transversely oriented supporting glass fibres bonded together with a light polyester stitching in a tricot pattern (Zoltek Corporation) was used as the reinforcement [14]. The total areal density of the fabric was 333 g/m^2. The matrix was a three-part fast-cure epoxy system containing EPIKOTE™ Resin TRAC 06150, EPIKURE™ Curing Agent TRAC 06150 and internal mould release agent HELOXY™ Additive TRAC 06805 (Hexion Inc.) [15, 130]. Flat carbon fibre/epoxy panels measuring 900 mm $\times$ 550 mm were fabricated using an HP-RTM process (see Cherniaev et al. [42] for processing details). Panels with two different fibre volume fractions, including 45% and 53% and two distinct stacking sequences, namely $[0_7]$ and $[0/\pm 45/90]_s$ with the 0° layers oriented along the 900 mm direction of the panels, were fabricated. A summary of the manufactured panels is provided in Table 3.1.

Table 3.1. The average thickness of CFRP panels comprising $[\mathbf{0_7}]$ and $[\mathbf{0/\pm45/90}]_s$ stacking sequences.

V_f (%)	Stacking Sequence	Average Thickness (±STV) (mm)
53	$[0_7]$	2.27 (±0.03)
45	$[0_7]$	2.70 (±0.03)
45	$[0/\pm45/90]_s$	3.01 (±0.04)

The mechanical properties of the CFRP lamina were adopted from Refs. [42, 131] (Table 3.2). Note, the longitudinal (1) and transverse (2) directions correspond to the directions along and transverse to the carbon fibre tows, respectively.

Table 3.2. Mechanical properties of cured unidirectional non-crimp fabric CFRP ply [42, 131].

		Fibre Volume Fraction, V_f (%)	
		45	53
$\boldsymbol{E_1}$ $(\boldsymbol{GPa})$	Longitudinal Young's modulus	102.7	123.4
$\boldsymbol{E_2}$ $(\boldsymbol{GPa})$	Transverse Young's modulus	8.1	8.4
$\boldsymbol{\nu_{12}}$	Major in-plane Poisson's ratio	0.25	0.37
$\boldsymbol{G_{12}}$ $(\boldsymbol{GPa})$	In-plane shear modulus	3.1	3.4
$\boldsymbol{X_t}$ $(\boldsymbol{MPa})$	Longitudinal tensile strength	1204	1765
$\boldsymbol{Y_t}$ $(\boldsymbol{MPa})$	Transverse tensile strength	51.9	60.3
$\boldsymbol{X_c}$ $(\boldsymbol{MPa})$	Longitudinal compressive strength	645.3	1000.7
$\boldsymbol{Y_c}(\boldsymbol{MPa})$	Transverse compressive strength	150.2	144.9
$\boldsymbol{S_{12}}$ $(\boldsymbol{MPa})$	In-plane shear strength	65.3	42.6

The adhesive used for this project was a two-part toughened structural epoxy, namely Impact Resistant Structural Adhesive 07333 (3M Canada Company). The mechanical properties of the adhesive were adopted from a study by Watson et al. [132] (Table 3.3).

Table 3.3. Mechanical properties of adhesive [132].

$\boldsymbol{E}$ $(\boldsymbol{GPa})$	Young's modulus	2.2
$\boldsymbol{\nu}$	Poisson's ratio	0.43

3.2 Single Lap Shear Test

3.2.1 Specimen Surface Preparation and Bonding Procedure

Adherends and tabs for the SLJ specimens were cut from the flat fabricated carbon fibre/epoxy panels with 45% fibre volume fraction using abrasive water jet cutting. Four different surface treatments were considered to investigate the influence of surface treatment on the joint strength and failure mode in the SLJ specimens. The first surface treatment consisted of degreasing the bond area of the adherend with acetone, which aided in removing surface contaminants. The second surface treatment involved abrading the bond area of the adherend with 400-grit aluminum oxide sandpaper and then degreasing with acetone. It should be noted that the surface of the adherend was degreased with acetone before the abrasion. The third surface treatment consisted of grit blasting the bond area of the adherend with 60-grit silicon carbide by applying 25 psi pressure and then degreasing with acetone. The fourth surface treatment had similar procedure to the third, except for a higher applied grit blasting pressure of 60 psi, which was intended to create a higher surface roughness.

To investigate the influence of the adherend stacking sequence on the joint strength and failure mode, four stacking sequences were considered in this study. Adherends with unidirectional plies were cut from the $[0_7]$ carbon fibre/epoxy panels, while adherends with

$[0/\pm 45/90]_s$, $[45/90/0/-45]_s$, and $[90/\mp 45/0]_s$ stacking sequences were all cut from the $[0/\pm 45/90]_s$ panels.

The SLJs had an overlap of 25.4 mm and the adhesive thickness was controlled by using 0.18 mm thick shims (Figure 3.1a). The dimensions are consistent with standard ASTM D 5868-01. Each SLJ specimen was placed onto the baseplate of the bonding fixture (Figure 3.1b). The length of the overlap area was adjusted by calibrating the distance between two length stop bars (parts A and B indicated in Figure 3.1c). Shoulder screws were placed between each SLJ specimen to make a sufficient gap between each sample for the excess adhesive and to ensure the samples were aligned during the curing process. Three top plates (parts C, D and E indicated in Figure 3.1c) were placed on top of the SLJ specimens and were secured by screws to adjust the bond-line thickness. Note that all parts of the bonding fixture were coated prior to assembly with a mould release solution, namely LOCTITE 700-NC (Henkel Corporation) to enable removal of the samples following curing. The adhesive curing process was performed in a convection oven (Binder, ED-53) for 90 min at 80℃. Note that the curing cycle was based on the adhesive manufacturer recommendation to provide reduced variability and achieve maximum strength in the shortest amount of curing time [133]. After curing, the excess adhesive was removed from each specimen (Figure 3.1d). Overall, seven different configurations of the SLJ specimens were considered in this project and the bond-line thickness and length for each were measured using a VHX 5000 opto-digital microscope (Keyence, Osaka) (Table 3.4).

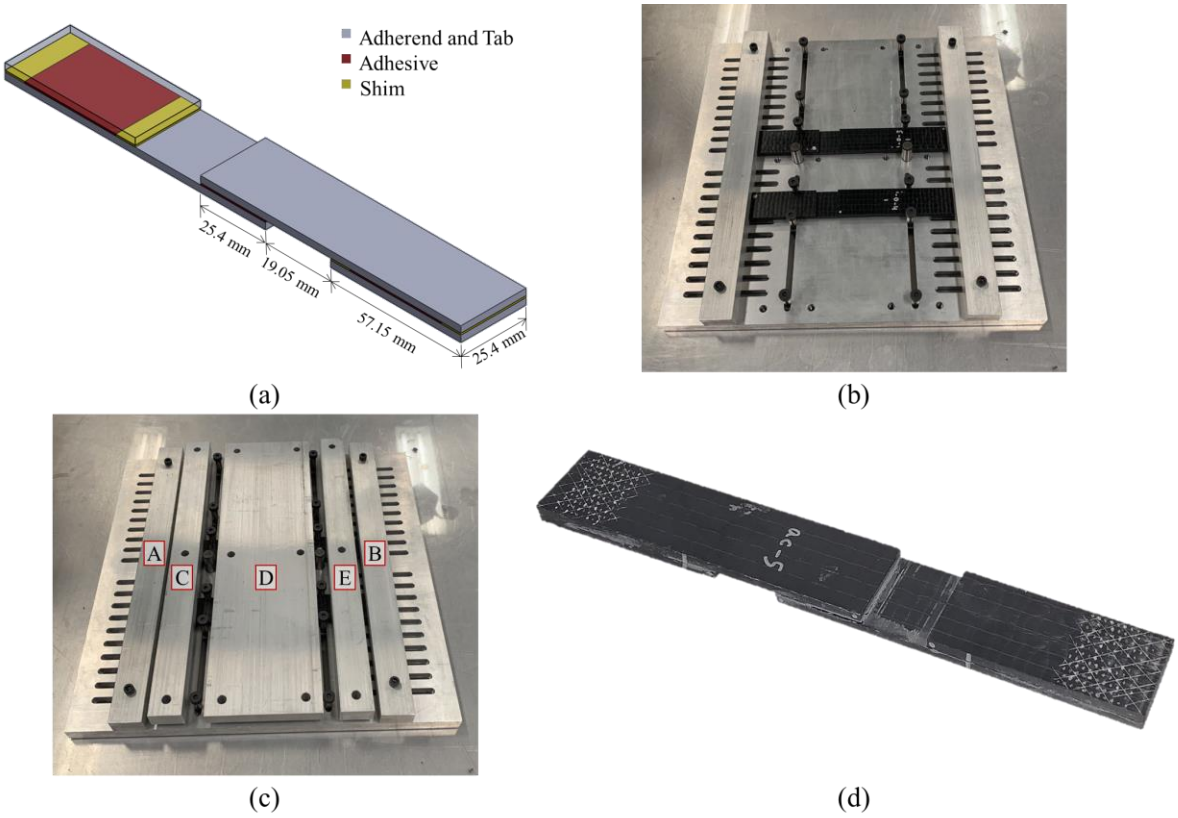

Figure 3.1. SJL specimen bonding procedure: (a) The geometrical properties of SLJ specimens, (b) Bonding fixture without top plates, (c) Bonding fixture with top plates and (d) Final SLJ specimen.

Table 3.4. Configuration of the SLJ specimens.

Specimen Code	Adherend Stacking Sequence	Surface Treatment	Average Bond-line Thickness (±STV) (μm)	Average Bond-line Length (±STV) (mm)
AC	$[0_7]$	Acetone	469.2 (±70.3)	24.8 (±0.50)
SP	$[0_7]$	Sandpaper	570.4 (±73.2)	26.2 (±0.55)
LGB	$[0_7]$	Low-pressure grit lasting	579.8 (±36.0)	25.7 (±0.44)
HGB	$[0_7]$	High-pressure grit blasting	591.6 (±75.1)	25.5 (±0.77)
INT0	$[0/\pm45/90]_s$	Sandpaper	256.7 (±37.6)	25.5 (±0.33)
INT45	$[45/90/0/-45]_s$	Sandpaper	307.6 (±26.8)	25.4 (±0.17)
INT90	$[90/\mp45/0]_s$	Sandpaper	333.8 (±31.2)	25.3 (±0.24)

3.2.2 Single Lap Shear Test Equipment and Setup

Single lap shear tests were conducted under ambient temperature and humidity conditions using a custom servo-hydraulic test frame with a 90 kN load cell capacity and wedge-type mechanical grips (Fig.3.2a). A constant crosshead speed of 0.1 mm/sec was applied to all SLJ specimens. The displacement for each SLJ specimen was measured optically by tracking two points at the edge of the SLJ tabs (points A and B indicated in Figure 3.2b) using an image tracking software (Tracker, Open Source Physics) from a video captured by a DLSR camera (Figure 3.2b). The DLSR camera was positioned orthogonal to the SLJ specimen and each test was imaged at a resolution of 1920 × 1080 pixels with a frame rate of 30 fps. Note, for all SLJ configurations five repeated tests were performed.

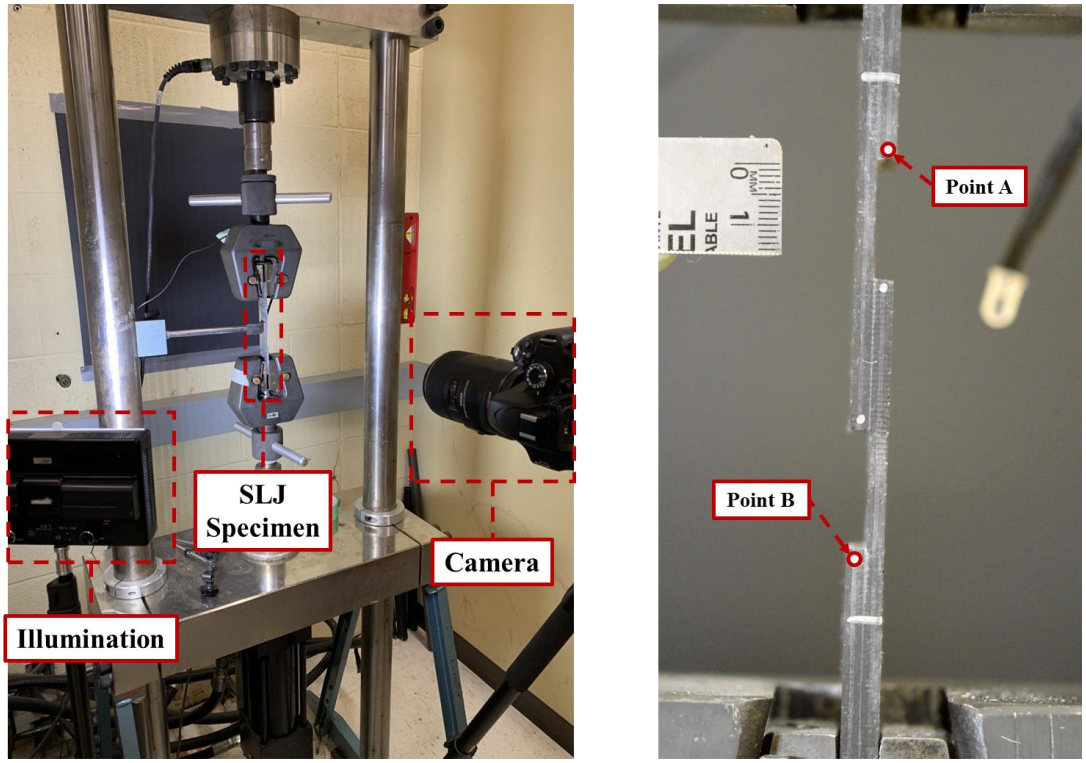

Figure 3.2. (a) Experimental setup of the SLJ test, (b) An image of the SLJ specimen captured by the DLSR camera.

3.3 Double Cantilever Beam Test

3.3.1 Test Specimen Surface Preparation and Bonding Procedure

Adherends for the DCB specimens were cut from the flat fabricated composite panels with $[0_7]$ stacking sequence, with 45% and 53% fibre volume fraction, using an abrasive water jet. The choice of surface treatment used for the DCB specimens was based on the SLJ experimental results (see Section 5.1.1). The treatment used for the SP SLJ specimens was used for the DCB specimens, which involved abrading the bond area of the adherend with 400-grit aluminum oxide sandpaper and then degreasing with acetone. The pre-crack length and the adhesive bond-line thickness were controlled by shims (Figure 3.3a). Each DCB specimen

was placed onto the baseplate of the bonding fixture (Figure 3.3b). The fixture was used to ensure adherend alignment. Two top plates (parts A, B indicated in Figure 3.3c) were placed on top of the DCB specimens and were secured by screws to make sure the bond-line thickness is as same as the thickness of shims (Figure 3.3c). The same curing cycle used for the SLJ specimens was used to bond the DCB specimens. Excessive adhesive was removed from each specimen after curing (Figure 3.3c). The bond-line thickness and pre-crack length were measured using a VHX 5000 opto-digital microscope (Keyence, Osaka). Three different bond-line thicknesses were considered in this project including 0.25 mm, 0.4 mm and 0.65 mm. Custom loading blocks with a width and thickness of 9.5 mm and a length of 25.4 mm were subsequently bonded to the test specimens using an instant adhesive, namely LOCTITE 480 (Henkel Corporation), and allowed to cure at room temperature (Figure 3.3c). Overall, six different configurations of the DCB specimens were considered in this study (Table 3.5).

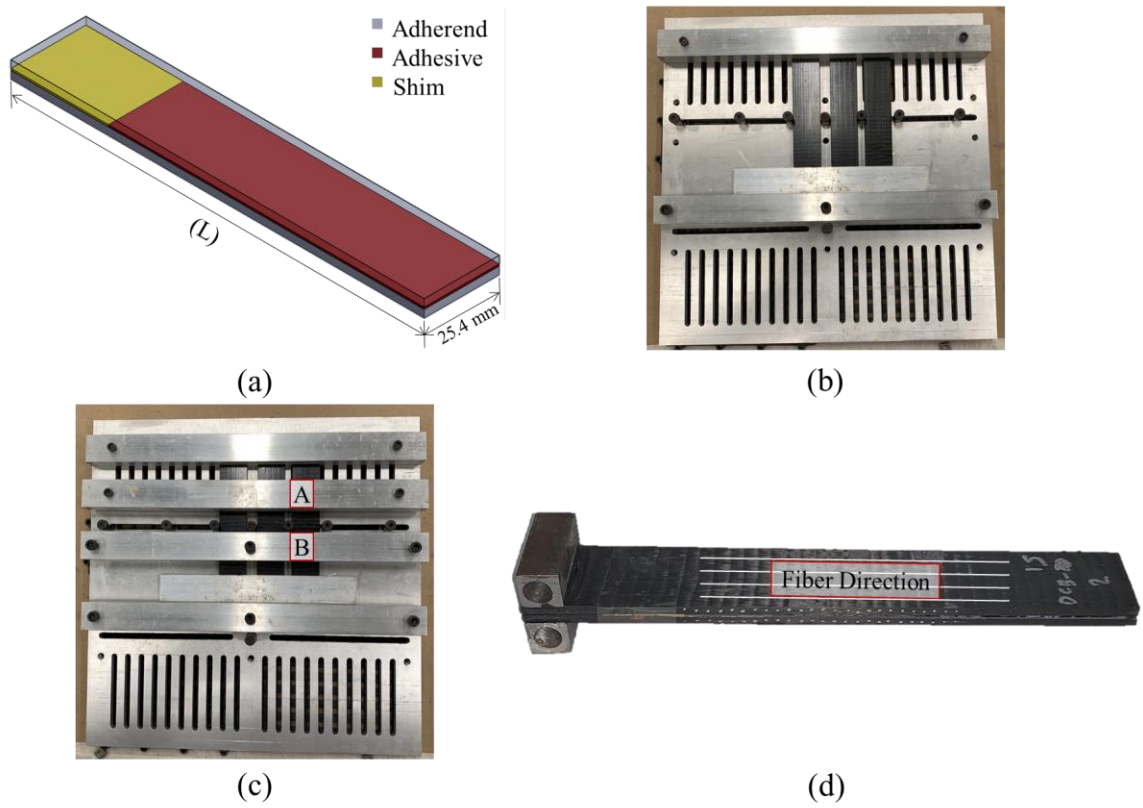

Figure 3.3. DCB specimen bonding procedure: a) The geometrical properties of DCB specimens where L=120 mm for DCB-1 specimens and L=140 mm for the rest of the DCB specimens, b) Bonding fixture without top plates, c) Bonding fixture with top plates and d) Final DCB specimen.

Table 3.5. Configuration of the DCB specimens.

Specimen Code	Nominal Bond-line Thickness (mm)	Loading Rate (mm/sec)	Fibre Volume Fraction (%)	Average Pre-crack Length (±STV) (mm)
DCB-1	0.25	0.1	45	33.45 (±1.09)
DCB-2	0.25	0.1	53	32.96 (±0.26)
DCB-3	0.4	0.1	53	32.91 (±0.28)
DCB-4	0.65	0.1	53	32.85 (±0.32)
DCB-5	0.4	5	53	33.11 (±0.29)
DCB-6	0.4	15	53	33.20 (±0.30)

3.3.2 Double Cantilever Beam Test Equipment and Setup

The DCB tests were conducted under ambient conditions using a servo-hydraulic test frame with an MTS Flex Test SE controller, a 2.2 kN capacity load cell and custom fixtures (Figure 3.4a). The load point displacement of each DCB specimen was measured optically by tracking two points at the blocks using an image tracking software (Tracker, Open Source Physics) from a video captured by the DLSR camera (Figure 3.4b). Also, crack propagation along the length of the DCB specimen was tracked using an image tracking software (Tracker, Open Source Physics) from a video captured by a second DLSR camera. The DLSR cameras were positioned orthogonal to the DCB specimen and each test was imaged at a resolution of 1280 × 720 pixels with a frame rate of 60 fps. Three different constant crosshead speeds including 0.1 mm/sec, 5 mm/sec and 15 mm/sec were applied to the DCB specimens. Note, for all DCB configurations at least four repeated tests were performed.

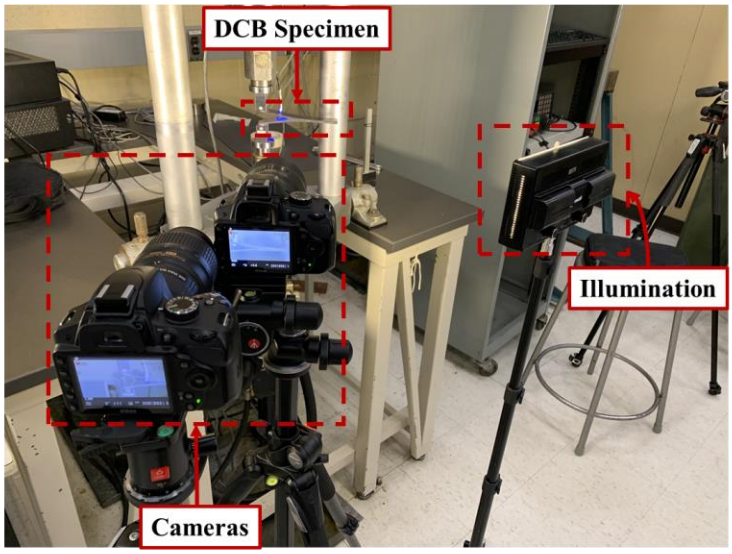

(a)

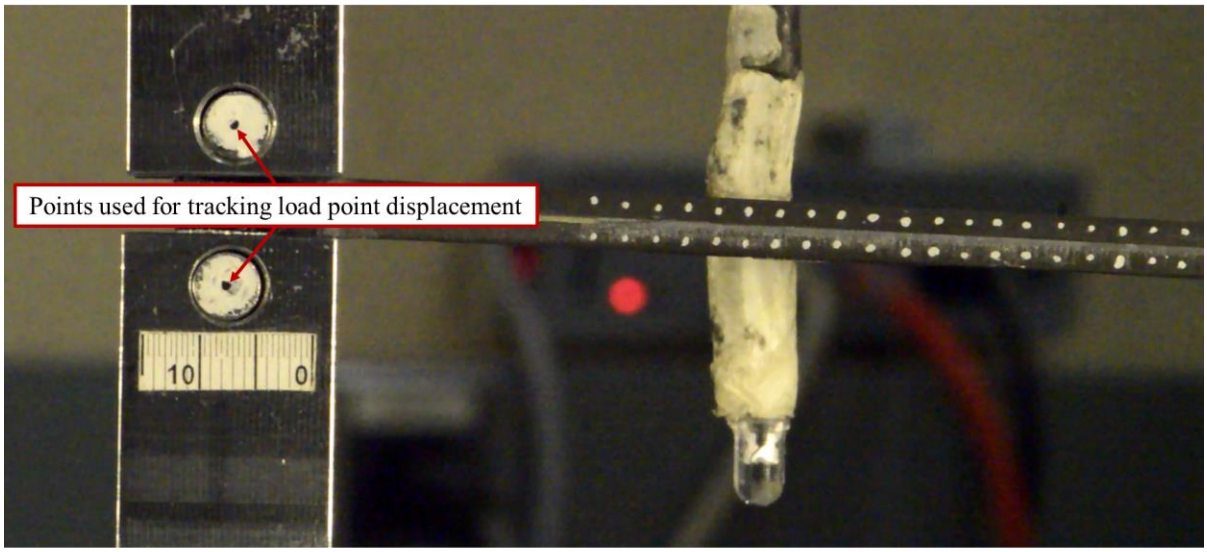

(b)

Figure 3.4. (a) Experimental setup of the DCB test, (b) An image of the DCB specimen captured by the DLSR camera.

3.3.3 Data Reduction Method

As indicated in Section 2.4.1, modified beam theory is a data reduction approach for calculation of critical SERR for DCB test specimens as proposed in ASTM D5528-0. The SERR was determined by the following equation:

$$G = \frac{3P\delta}{2B(a+\Delta)} \quad (1)$$

Here, P, δ, B and a are the applied load, load point displacement, DCB specimen width and crack length, respectively. In addition, Δ is calibration parameter that was experimentally determined by generating a least-square plot of the cube root of the compliance $C^{1/3}$, as a function of the crack length (a) (Figure 3.5). The compliance (C) was calculated by dividing the load point displacement (δ) by the applied load (P).

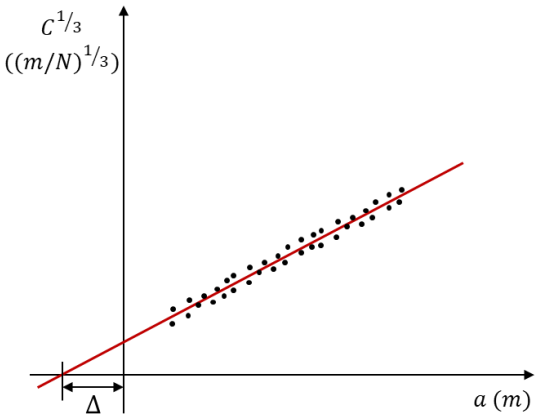

Figure 3.5. Cube root of the compliance as a function of the crack length.

To measure the crack length at a given point in time, specific points above and below the bond line at 2.5 mm increments along the specimen length were considered (Figure 3.6a). The vertical distance of each pair of points was extracted from a video captured by a DLSR camera

using an image tracking software (Tracker, Open Source Physics). The time corresponding to crack initiation was assumed to be the time when the vertical distance began to increase. Hence, for all DCB tests, a crack length plot as a function of time was generated (Figure 3.6.b) and synchronized with the force-time or load point displacement-time plots to extract the force and the load point displacement at each specific crack length (Figure 3.6c).

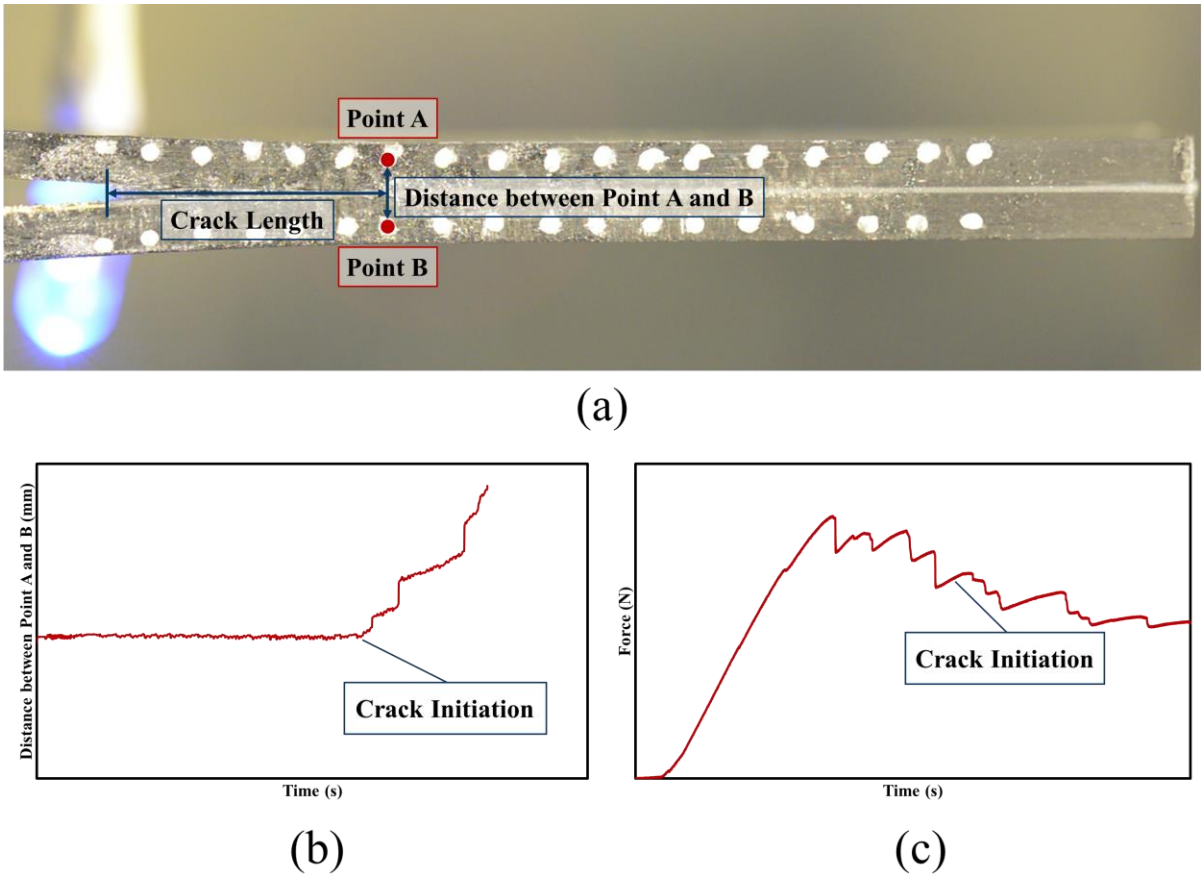

Figure 3.6. Crack tracking process: (a) a picture from the DCB specimen during the test, (b) plot of the distance between two points versus time at a specific crack length of the DCB specimen, and (c) force-time plot of the DBC specimen.

Chapter 4: Numerical Modelling Methodology

This chapter presents the details of FEA performed in this study using the commercial finite element software (ABAQUS 6.14-2). An FE model was developed for the assessment of local stress fields in the SLJ specimens (Section 4.1), while a second FE model was developed for calibration of the cohesive properties for the DCB tests (Section 4.2).

4.1 Single Lap Joint Modelling

Single lap shear tests were simulated to analyze the local stress states in the adherends of the different SLJ specimens and gain insight into the driving forces for the observed failure mechanisms. Eight-node three-dimensional solid elements (C3D8R) were used to mesh the CFRP adherends and the adhesive for each SLJ specimen considered. The composite adherend plies and adhesive were modelled as transversely isotropic and isotropic linear elastic materials, respectively (Tables 3.2 and 3.3). The interface between the adherends and adhesive were assumed to have a strong bond; thus, common nodes were used in the FE model. For the stationary grip on one end of the SLJ specimen all nodal displacements and rotations on the gripped area were constrained ($U_{x,y,z} = UR_{x,y,z} = 0$), while on the opposite end the nodes on the gripped area were constrained along the y- and z-directions and only allowed translation along the x-direction (Figure 4.1). The applied load, which corresponded to the maximum tensile load at damage onset as measured from each SLJ test, was distributed over the grip area of the SLJ specimen and applied along the x-direction (Figure 4.1).

A mesh sensitivity study was performed to determine a suitable mesh density for the SLJ specimen models, where the INT0 specimen was considered by investigating the local stress gradient along the specimen width in the bonded 0° ply at the end of the specimen overlap

region. Six different element sizes within the plane of the specimen adherends were considered, including 1 mm x 1 mm, 0.5 mm x 0.5 mm, 0.25 mm x 0.25 mm, 0.15 mm x 0.15 mm, 0.1 mm x 0.1 mm, and 0.05 mm x 0.05 mm. In addition, the mesh density through the thickness of the specimen adhesive and adherends was considered, including 1, 2, 4 and 8 through-thickness elements. Further details about the mesh sensitivity study will be discussed in Section 5.1.3.

For each simulated SLJ specimen, the local stress fields in the CFRP adherend along the width of each ply, at the end of the overlap region, were assessed (i.e. failure assessment plane in Figure 4.2). Note, the failure assessment plane was chosen based on observations of damage onset made during the experiments (Section 5.1.2). The maximum stress theory was invoked to predict the onset of ply failure using the stresses from the numerical model and the strengths presented in Table 3.2, with the goal of further understanding the progressive failure process of the SLJ specimens.

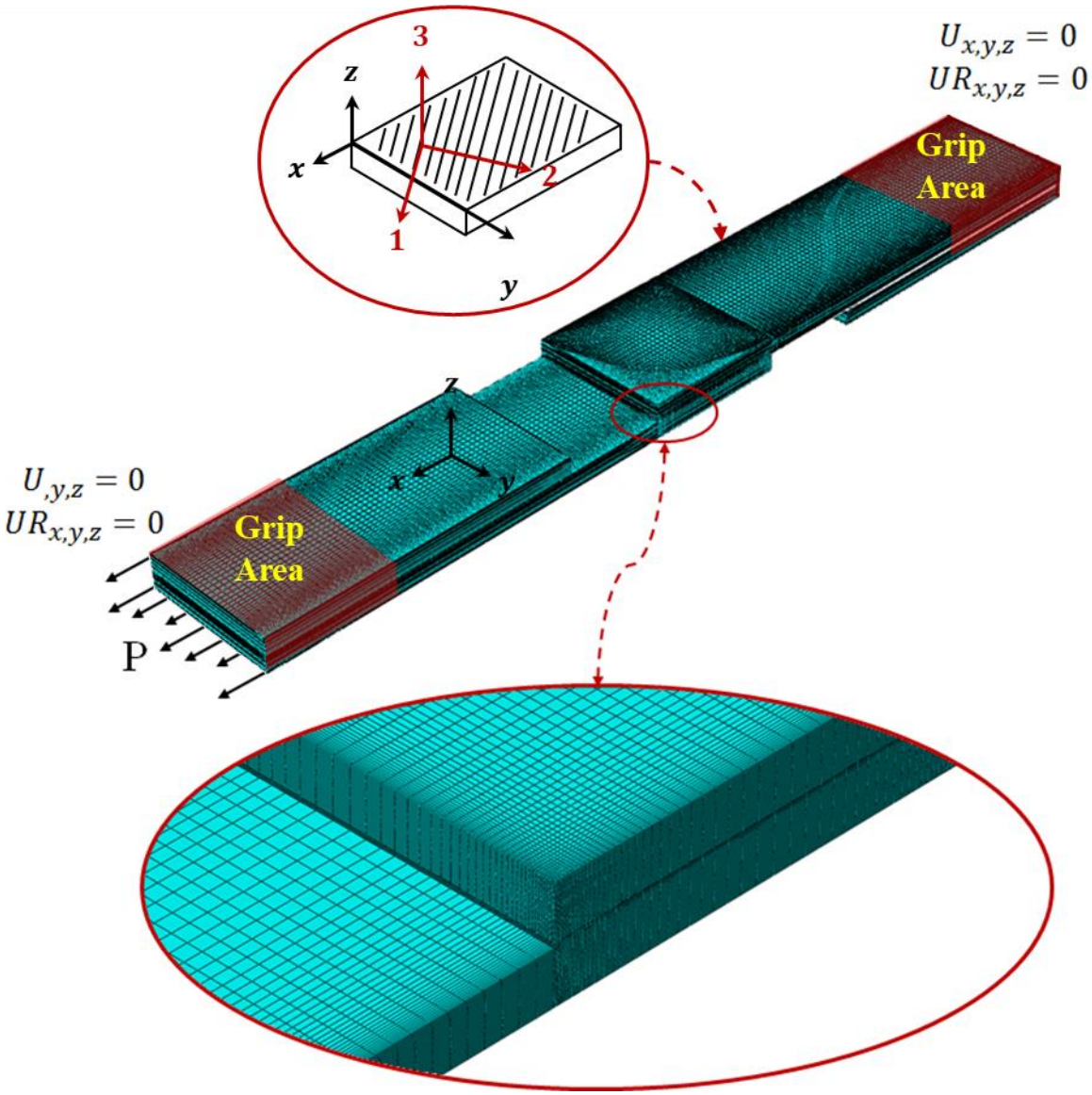

Figure 4.1. Boundary and loading conditions and mesh generation of the finite element model for the SLJ specimens**.**

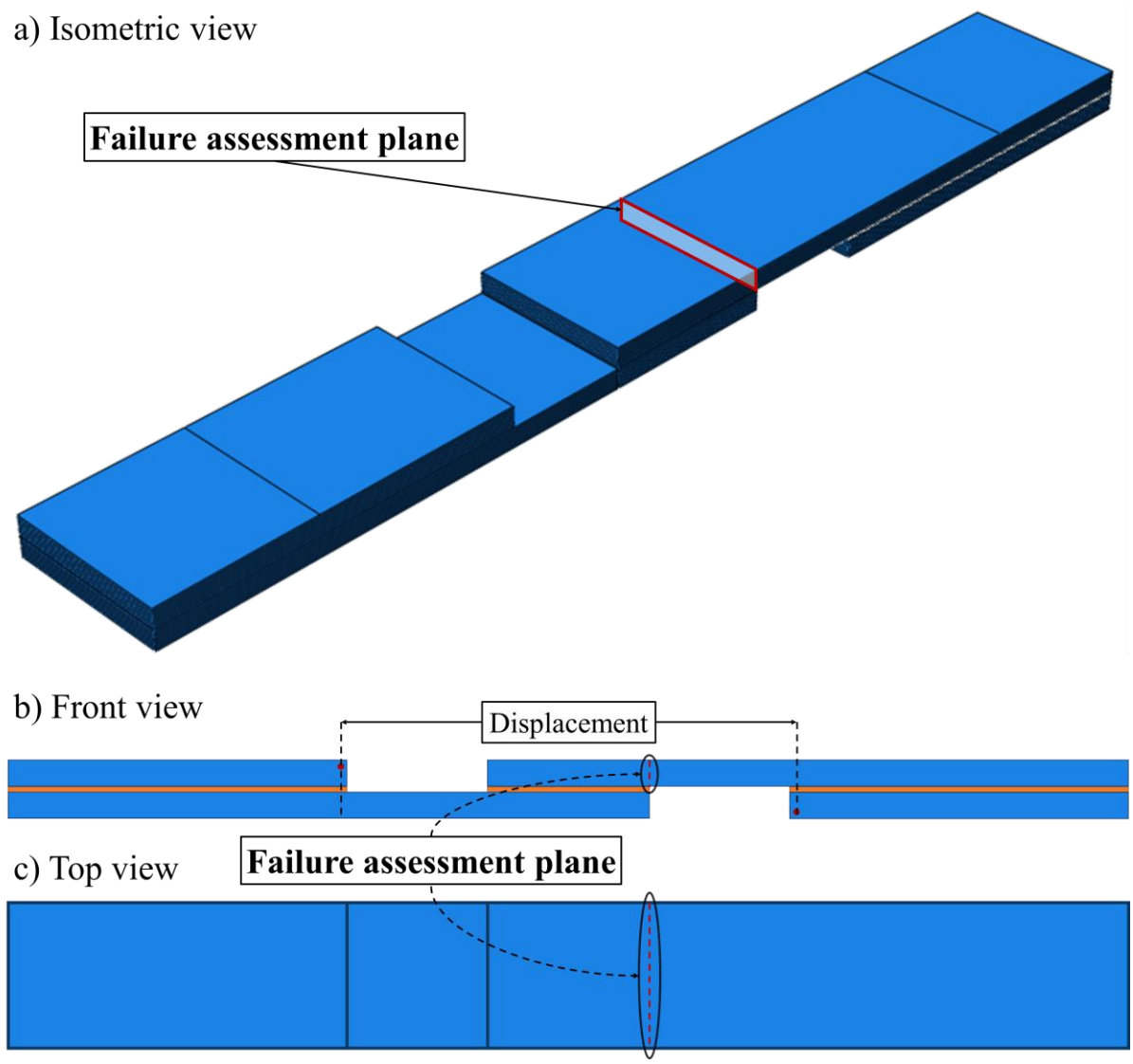

Figure 4.2. Schematic of the failure assessment plane for the SLJ finite element model indicated in different views including (a) isometric, (b) front, and (c) top.

4.2 Double Cantilever Beam Modelling

Finite element analysis of the DCB test specimens was conducted to calibrate the Mode I traction-separation response of the adhesively bonded joint by comparing the predicted and experimentally measured force-displacement response (i.e. the so-called inverse method). A

two-dimensional finite element analysis was used for modelling the DCB specimens to reduce the computational time during the iterative process. A two-dimensional analysis was deemed acceptable since all the DCB specimens comprised CFRP adherends with $[0_7]$ stacking sequence and the model was not used to analyze local stress states of the DCB specimens. Therefore, four-node bilinear plane strain elements (CPE4R) and four-node two-dimensional cohesive elements (COH2D4) were used to mesh the adherends and adhesive of the DCB specimen, respectively. The composite adherend plies were modelled as a transversely isotropic linear elastic material (Table 3.2). The adhesive was modelled using a bilinear traction-separation cohesive zone model [25], which was chosen due to the availability in Abaqus. For the bottom adherend, the displacements of one node at the bottom corner were constrained along the x- and y-directions ($U_{x,y} = 0$), while for the upper adherend, the displacements of one node at the top corner were constrained along the x-direction to prevent the rigid body motion but allowed to translate in the y-direction to a set displacement (Figure 4.3a).

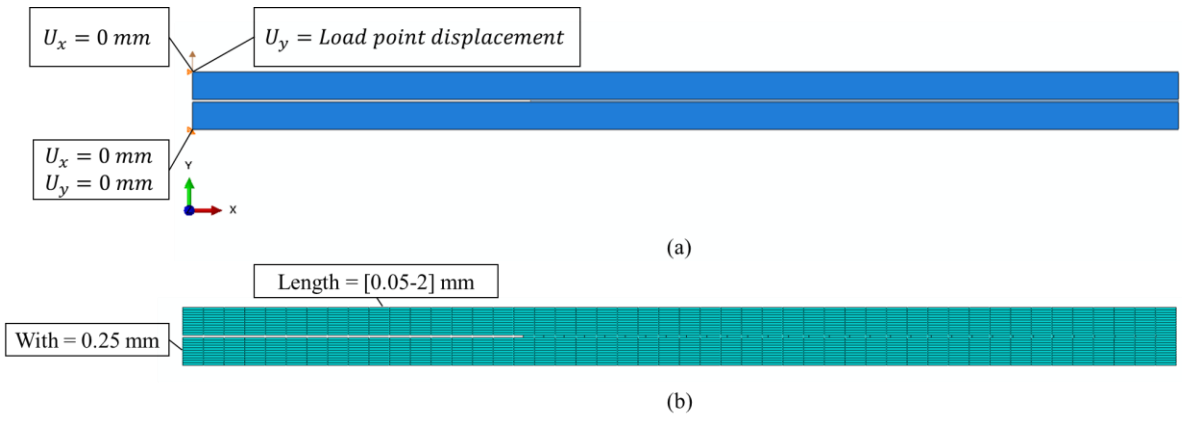

Figure 4.3. DCB specimen FE model: (a) Boundary conditions and (b) mesh generation**.**

Four different element lengths along the length of the DCB specimen (0.5, 0.25, 0.125 and 0.05 mm) were considered in the FE model to study the influence of mesh element size on the prediction of the force-displacement response. The element width along the specimen thickness direction considered for modelling the CFRP adherends was 0.25 mm (Figure 4.3b). The adhesive was modelled using CZM elements with the length corresponding to the element size of the adherends, and the bond-line thickness corresponding to that measured experimentally for each DCB specimen. Further details about the mesh sensitivity study will be discussed in Section 5.2.4.1.

The critical SERR values extracted from the DCB test results were employed as the fracture energy for the cohesive zone law in the FE model and fixed during the parameter calibration. The traction-separation response parameters, namely the peak stress and initial stiffness, were variable during the parametric study (Table 4.1). In the first case, the DCB specimen was simulated with constant initial stiffness and critical SERR value, while four different values were considered for peak traction including 5, 12.5, 25 and 53.28 MPa in order to calibrate the peak traction parameter. The same procedure was employed in the second case for calibration of initial stiffness, where five different values were considered including 500, 1000, 1500, 2585 and 4000 MPa and constant values were considered for peak traction and critical SERR. Further details about the result of the parametric study will be discussed in Section 5.2.4.2.

Table 4.1. Cohesive material properties used in the parametric study.

	Numerical Model Code	Initial Stiffness (MPa)	Peak Traction (MPa)	Critical SERR ($G_{Ic_{avg}}$) (kJ/m^2)
Case 1	1-1	2589	5	1.39
	1-2	2589	12.5	1.39
	1-3	2589	25	1.39
	1-4	2589	53.38	1.39
Case 2	2-1	500	53.38	1.39
	2-2	1000	53.38	1.39
	2-3	1500	53.38	1.39
	2-4	2585	53.38	1.39
	2-5	4000	53.38	1.39

Chapter 5: Experimental and Numerical Results

In this chapter, the results and outcomes of the SLJ tests are presented in Sections 5.1.1 and 5.1.2. An in-depth assessment of the SLJ specimen fracture surface morphology, including the relevant numerical results, are presented in Section 5.1.3. The results of the DCB tests performed to characterize the Mode I fracture behaviour of the adhesively bonded NCF-CFRP joints are presented in Sections 5.2.1, 5.2.2 and 5.2.3. The numerical simulation results of the DCB tests that were used to calibrate the Mode I traction-separation law parameters for a CZM are presented in Section 5.2.4.

5.1 Single Lap Joint Tests

5.1.1 Influence of Adherend Surface Treatment on Joint Performance

The surface roughness of the $[0_7]$ composite laminate adherends was measured after each treatment using a Surtronic 25 profilometer (Taylor Hobson, Warrenville) (Table 5.1). An increase in surface roughness was observed for the surface treated with sandpaper when compared with the adherend treated with acetone. The highest roughness was achieved by using grit blasting, where a change in the pressure used did not notably influence the average roughness values. Microscopic topography of the treated composite adherend surfaces revealed that the specimens treated by grit blasting exhibited local damage in the polymer matrix (Figure 5.1d).

Table 5.1. Average surface roughness of CFRP adherends with different surface treatments.

Surface treatment	Average roughness (R_a) (±STV) (μm)
Acetone (AC)	0.3 (±0.07)
Sandpaper (SP)	0.6 (±0.04)
Low-pressure grit blasting (LGB)	1.8 (±0.68)
High-pressure grit blasting (HGB)	1.8 (±0.12)

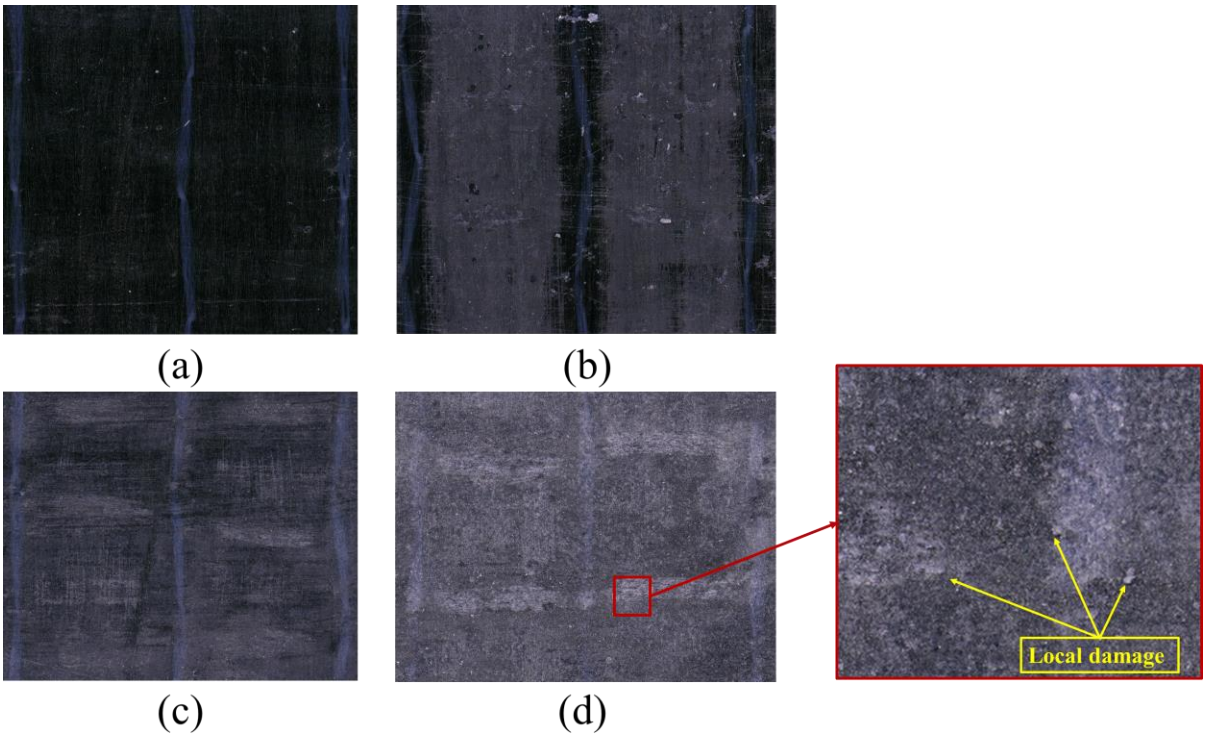

Figure 5.1. Images of the treated surfaces of the SLJ adherends: a) cleaning with acetone, b) abrading with sandpaper, c) low-pressure grit blasting d) high-pressure grit blasting.

For the SLJ test, the joint strength was determined as the magnitude of the load measured at failure divided by the specimen overlap area. The results revealed that the highest average joint strength and the lowest variability (i.e., 24.7 MPa with ±1.5 MPa standard deviation) was observed for the SLJ specimens treated with sandpaper (SP) (Figure 5.2). However, a comparison of the SLJ strength for specimens with different adherend surface treatments revealed that there was no statistically significant difference.

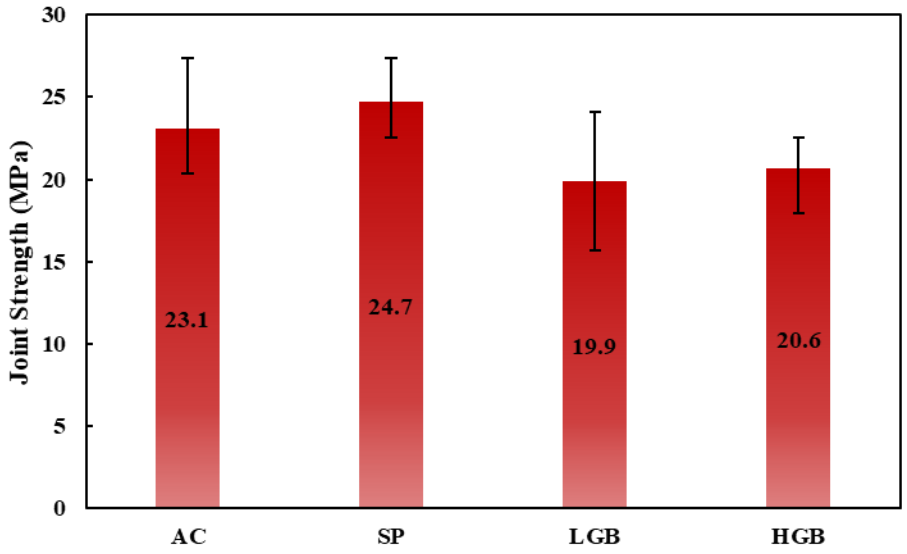

Figure 5.2. The joint strength of SLJ specimens comprising $[0]_7$ laminate with different surface treatments (error bars indicate max/min values).

Inspection of the specimen fracture surfaces revealed that the failure mode was consistent for each SLJ specimen regardless of the surface treatment used (Figure 5.3). The purple region in the images corresponds to the adhesive layer that remained bonded to one adherend (e.g. see Figure 5.3a). The black shades on the purple region were thin layers of epoxy and carbon fibres removed from the surface of the 0^o ply from the opposite adherend. Therefore, an intra-laminar crack initiated and propagated near the surface of the first 0^o ply in one composite adherend, which caused a thin layer of epoxy bonded to the adhesive to be removed.

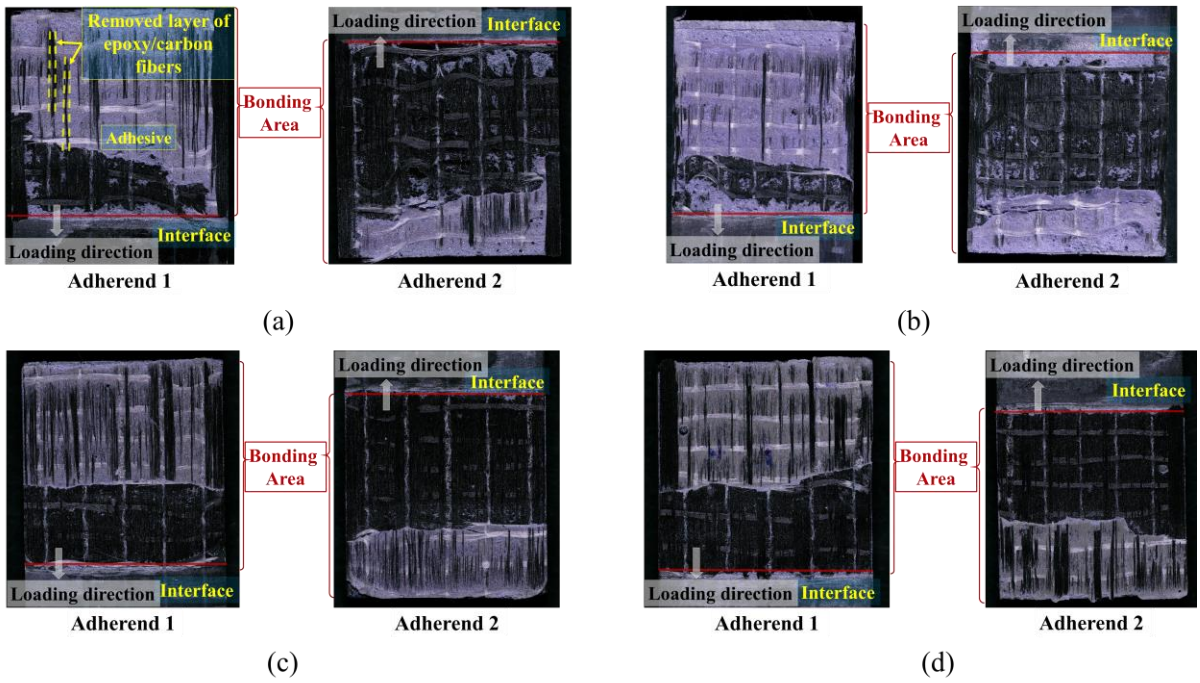

Figure 5.3. The fracture surfaces of SLJ specimens comprising an adherend with a $[0]_7$ laminate with different surface treatments: (a) acetone, (b) sandpaper, (c) low-pressure grit blasting, and (d) high-pressure grit blasting.

5.1.2 Influence of Adherend Stacking Sequence on Joint Performance

The joint strength was compared for SLJ specimens comprising adherends with different stacking sequences and treated with sandpaper. Note, the sandpaper surface treatment was chosen due to the higher exhibited average joint strength, lowest variability (Section 5.1.1), and the ease of application. The effective in-plane longitudinal modulus (E_x) and flexural longitudinal modulus (E_x^f) were calculated for each adherend laminate using classical laminate theory as per the following equations (assuming a symmetric laminate):

$$E_x = \frac{1}{tA_{11}^*} \tag{5.1}$$

$$E_x^f = \frac{12}{t^3 D_{11}^*} \tag{5.2}$$

Here, t is the overall laminate thickness with a value of 2.7 mm for the $[0_7]$ stacking sequence and 3 mm for the $[0/\pm 45/90]_s$, $[45/90/0/-45]_s$ and $[90/\mp 45/0]_s$ stacking sequences. A_{11}^* is a coefficient in the extensional compliance matrix $[A^*]$ and D_{11}^* is a component of the bending compliance matrix $[D^*]$, which were described in Section 2.1.2.

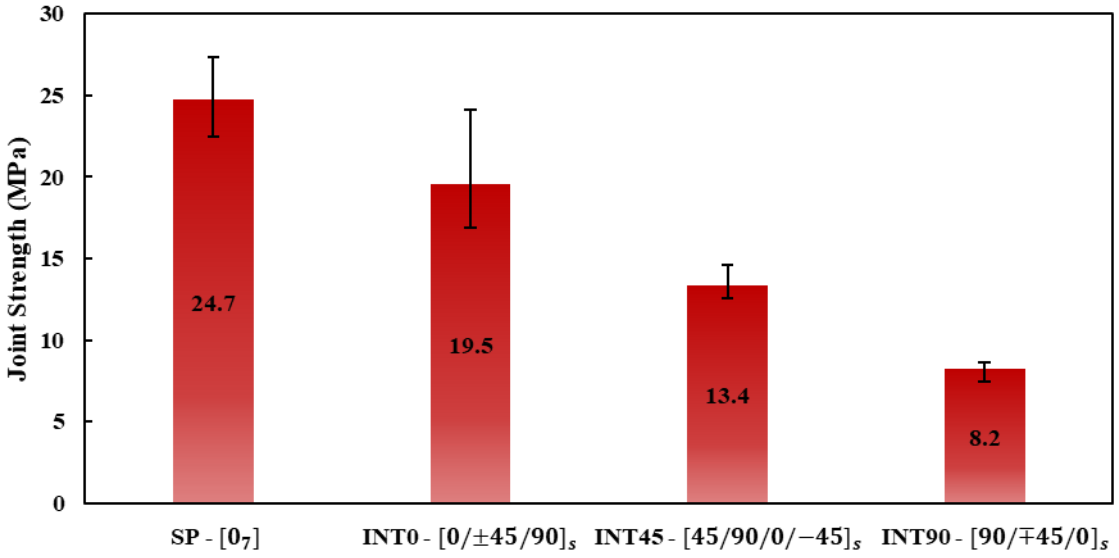

Figure 5.4. The joint strength for SLJ specimens with adherends comprising varying stacking sequences.

Table 5.2. Calculated effective in-plane and flexural longitudinal moduli for the indicated laminates.

Specimen Code	Laminate Stacking Sequence	Effective In-plane Longitudinal Modulus (GPa)	Effective Flexural Longitudinal Modulus (GPa)
SP	$[0_7]$	102.7	102.6
INT0	$[0/\pm 45/90]_s$	39.4	65.4
INT45	$[45/90/0/-45]_s$	39.4	21.5
INT90	$[90/\mp 45/0]_s$	39.4	16.3

In the initial assessment, the performance of the SP and INT0 SLJ specimens were compared. The SP specimen comprising an adherend with a $[0_7]$ stacking sequence exhibited a 27% increase in the average joint strength in comparison to the INT0 specimen, which consisted of an adherend with a $[0/\pm 45/90]_s$ stacking sequence (Figure 5.4). The effective flexural longitudinal modulus of the adherend for the SP specimen was 57% higher when compared to that of the INT0 specimen (Table 5.2). Note that the ply orientation adjacent to the adhesive layer (i.e. 0° ply) was the same in the SP and INT0 specimens.

The fracture surfaces for both the SP and INT0 specimens revealed that an intra-laminar matrix crack propagated just below the surface of the adherend in the first 0° ply. As a result, a thin layer of epoxy and carbon fibres were removed from the adherend (see black regions in Figure 5.5), as was found for the SLJ specimens with different surface treatments. For the SP specimen, a thin epoxy layer was removed in both CFRP adherends (Figure 5.5a), while for the INT0 specimen a thin layer of epoxy was removed in only one of the CFRP adherends (see adherend 1 of the INT0 specimen in Figure 5.5b). Furthermore, in some cases for the INT0 SLJ specimen a matrix crack propagated through the thickness of the first 0^o ply and reached the interface with the adjacent 45^o ply, where an inter-laminar delamination crack occurred (see the left side of adherend 1 for specimen INT0 in Figure 5.5b). Note, for both configurations there was virtually no fracture observed in the adhesive.

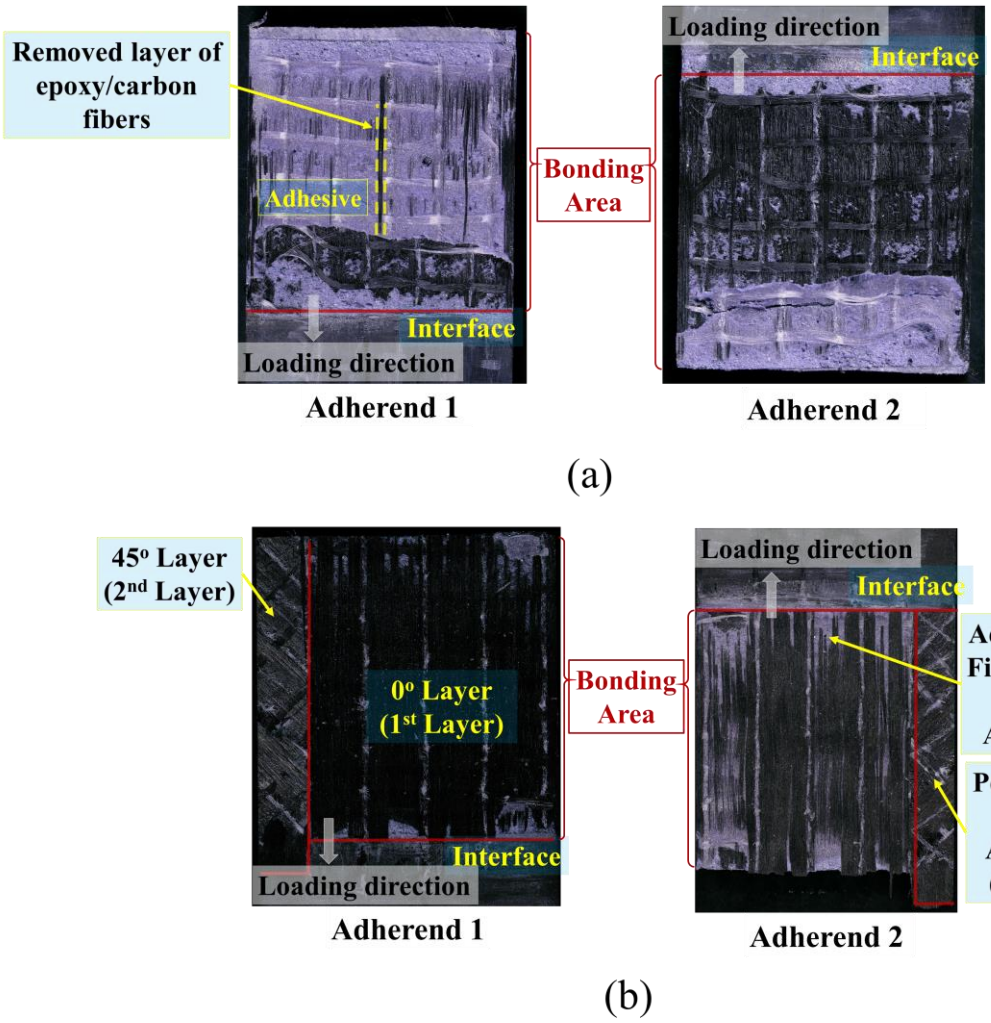

Figure 5.5. The fracture surfaces of SLJ specimens with different stacking sequences: (a) SP specimen comprising an adherend with a $[0_7]$ stacking sequence, (b) INT0 specimen comprising an adherend with a $[\mathbf{0}/\pm\mathbf{45}/\mathbf{90}]_s$ stacking sequence.

The next assessment aimed to compare the joint strength of SLJ specimens with adherends comprising different quasi-isotropic stacking sequences, namely INT0, INT45 and INT90 (i.e. $[0/\pm45/90]_s$, $[45/90/0/-45]_s$ and $[90/\mp45/0]_s$, respectively). The highest average joint strength was observed for the INT0 specimen, i.e., 19.5 ± 3.2 MPa (Figure 5.4), which had the

highest effective flexural modulus (Table 5.2). Note, that the effective in-plane longitudinal modulus of these three stacking sequences was the same (Table 5.2).

Observation of the fracture surfaces revealed that the orientation of the unidirectional CFRP ply in the adherend adjacent to the adhesive layer influenced the fracture surface morphology (Figures 5.5 and 5.6). For the INT45 specimen, a through-thickness matrix crack propagated along the fibre direction of the 45^{o} ply outside the overlap area in one of the adherends. Within the overlap area, a matrix cracking also formed in the 90° ply and propagated through the ply thickness, reaching the interface with the adjacent 0^{o} ply. Finally, in the 0^{o} ply a crack propagated through epoxy and a thin layer of epoxy was removed, which led to SLJ specimen failure (see Adherend 1 in Figure 5.6a). However, for the INT90 specimen comprising an adherend with a $[90/\mp 45/0]_s$ stacking sequence, observation of the fracture surface indicated that delamination cracks occurred in the adherend, between the 90^{o} and -45^{o} plies and between the -45^{o} and 45^{o} plies (Figure 5.6b). In addition, a matrix crack propagated through the 90° ply thickness at the end of the specimen overlap area. Within the overlap area, a matrix cracking formed in the -45° ply and propagated through the ply thickness.

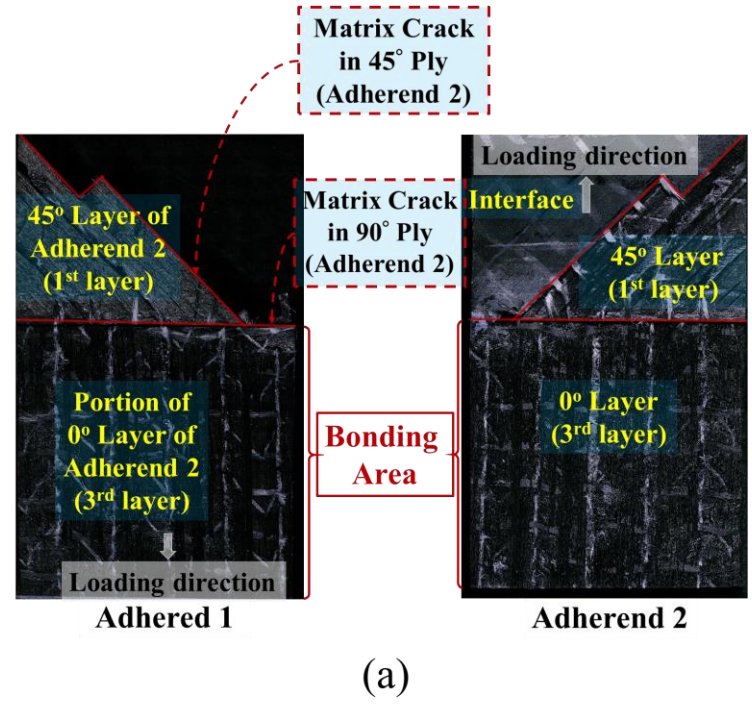

Figure 5.6. Fracture surfaces of SLJ specimens with different stacking sequences: (a) INT45 specimen comprising an adherend with a $[\mathbf{45/90/0/-45}]_s$ stacking sequence, (b) INT90 specimen comprising an adherend with a $[\mathbf{90/\mp 45/0}]_s$ stacking sequence.

In-situ observations of the edges for the SP, INT0 and INT45 SLJ specimens indicated that damage initiation occurred at the maximum tensile load, which was immediately followed by rapid final failure (i.e. points A, B and D from Figure 5.7). However, observations during the tests for the INT90 specimens revealed that damage initiated at the maximum tensile load (i.e. point C from Figure 5.7) prior to final failure of the specimen (i.e. point E from Figure 5.7). Note, force fluctuations observed during the tests (Figure 5.7) were a result of the experimental setup and limitations with the data acquisition system during low magnitude displacements.

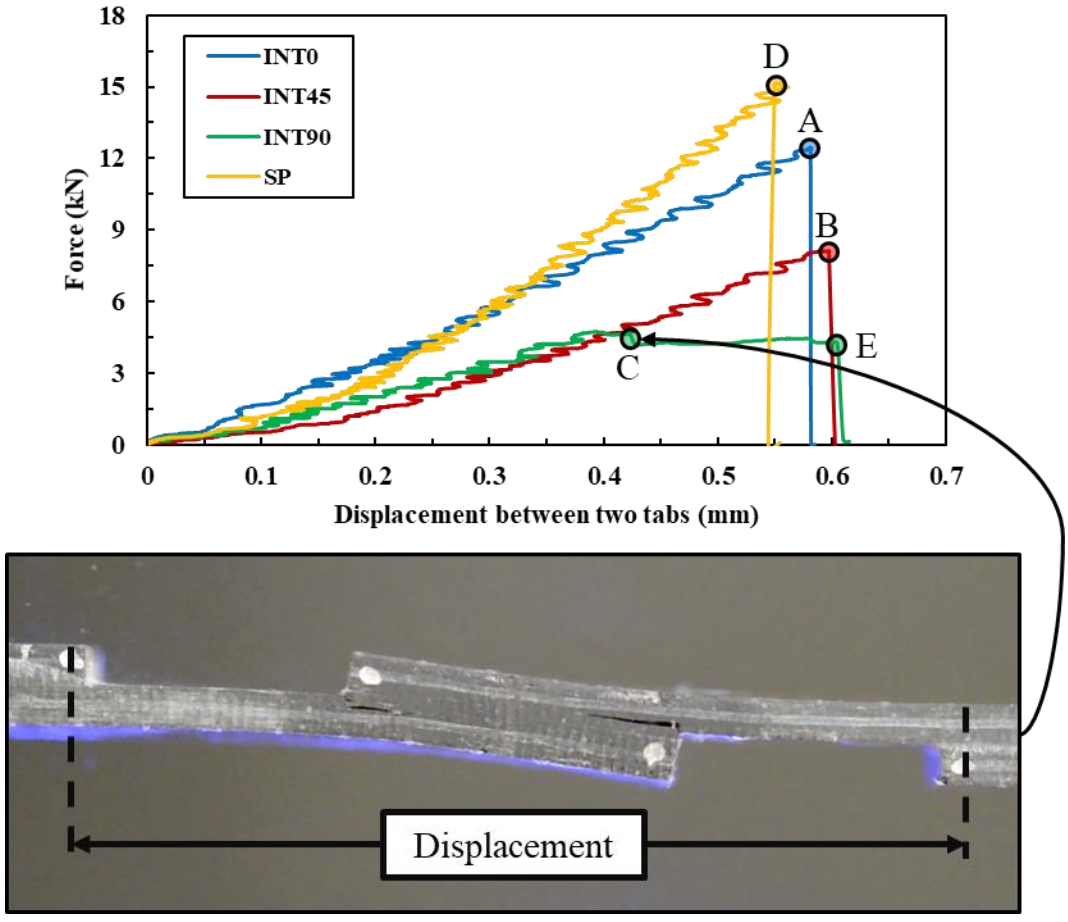

Figure 5.7. Force-displacement response of INT0, INT45, INT90 and SP SLJ specimens. Note, the relative displacement along the loading direction between the two points shown on the specimen edge were measured.

5.1.3 Failure Mechanisms

Overall, a comparison between the fracture surfaces of each SLJ specimen with different adherend ply stacking sequences revealed that there was no adherend/adhesive interfacial failure or cohesive failure for all specimens. However, four distinct failure modes were observed, which comprised of distinct local crack patterns within the adherends (Figure 5.8).

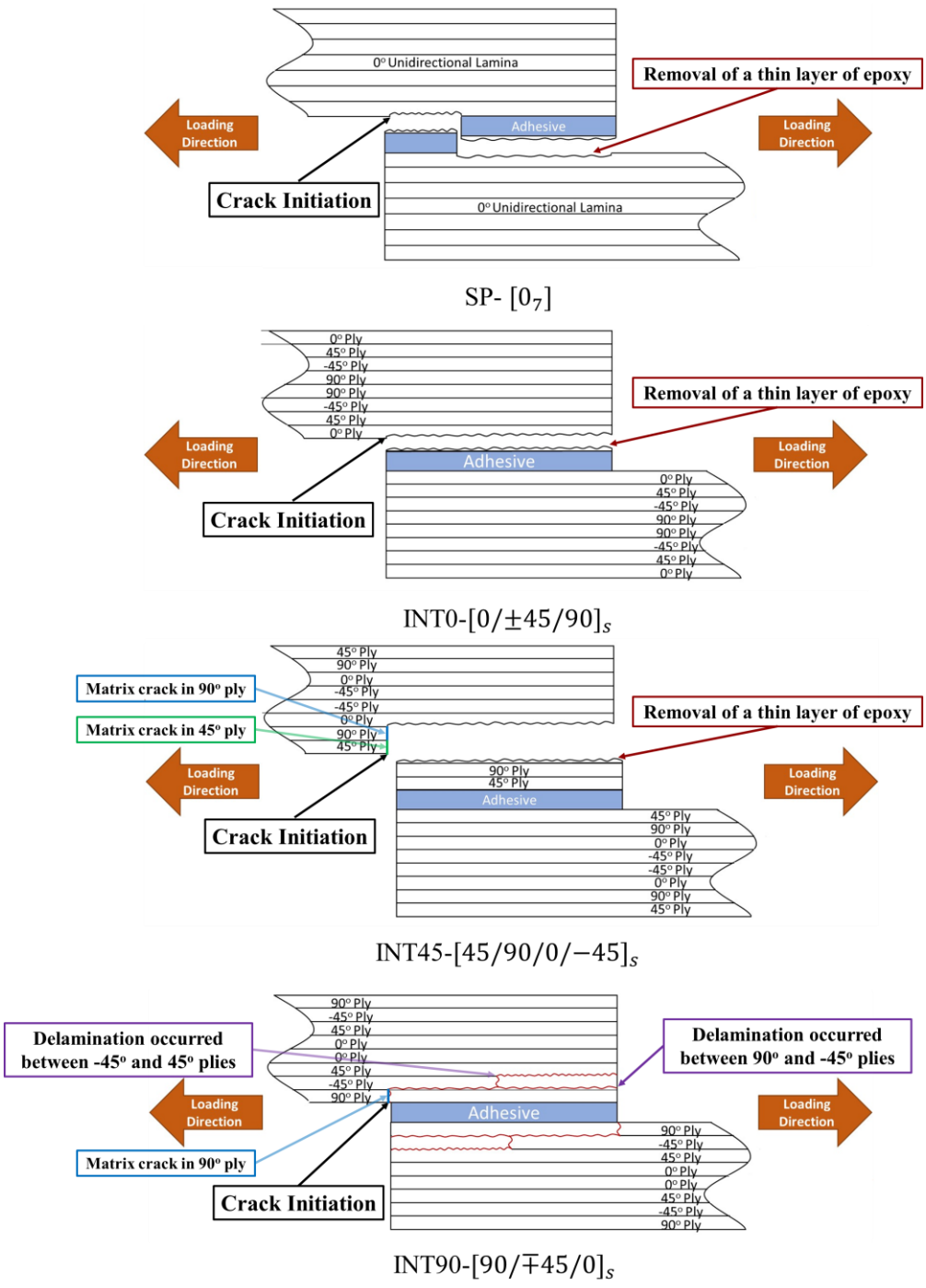

Figure 5.8. Schematic of distinct failure modes observed in the SLJ specimens with different stacking sequences.

The finite element model described in Section 4.1 was used to determine the local stresses in the plies of the SLJ specimen adherends, and gain a better understanding of the driving forces for the observed failure mechanisms.

First, a mesh sensitivity study was performed to determine a suitable mesh density for the SLJ specimen models. The INT0 SLJ specimen subjected to an axial force of 12.4 kN was used for this purpose, where the gradient of transverse stress along the specimen width in the bonded 0° ply at the end of the specimen overlap region was assessed. For different overall mesh densities, the stress field converged once a total of 655,360 elements were used to mesh the model, which corresponded to 1 mm x 1 mm and 0.1 mm x 0.1 mm elements used at the center and end of the overlap region (Figure 5.9a), respectively. While considering the mesh density through the thickness of the specimens, 4 elements through the thickness of the adhesive and each of the adherend plies also resulted in a converged stress field (Figure 5.9b). Therefore, all SLJ specimen models considered in this study comprising a mesh with the converged densities.

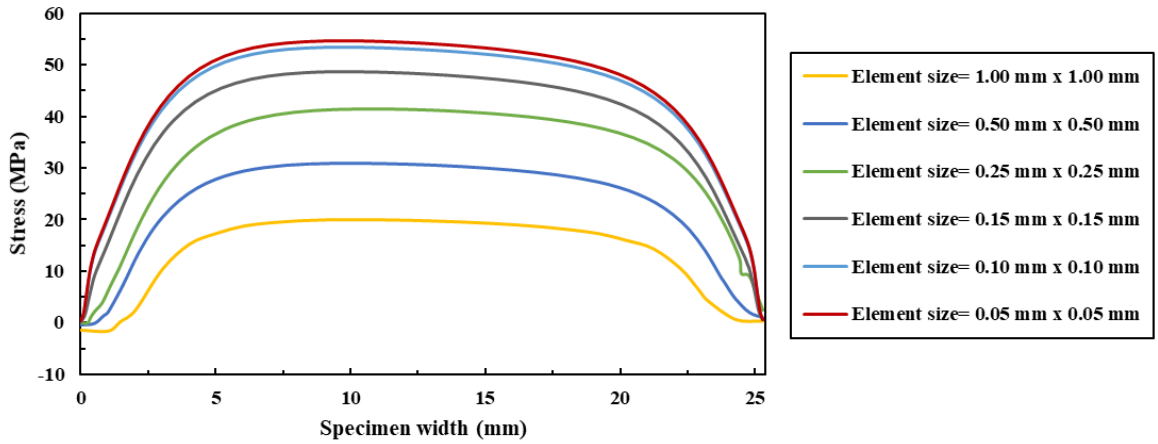

(a)

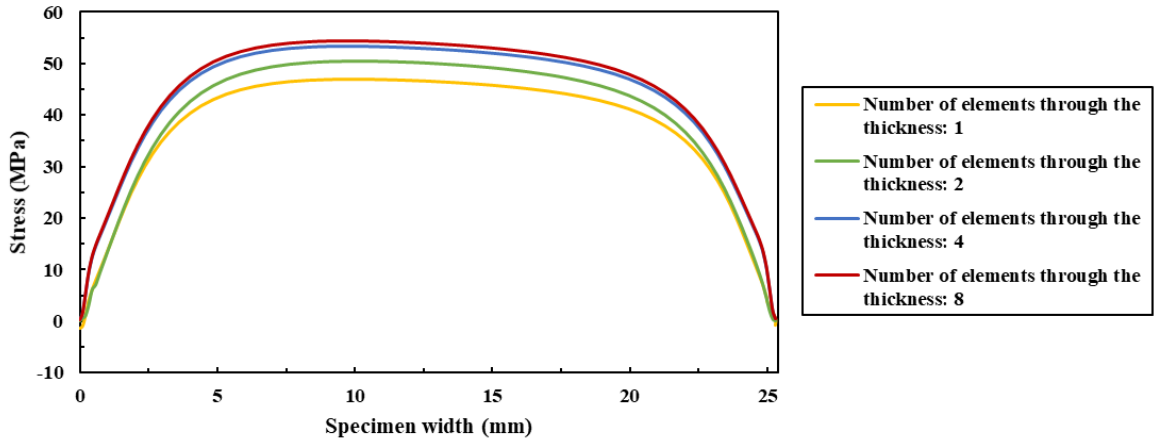

(b)

Figure 5.9. The influence of element size on the transverse stress variation across the SLJ specimen width in the bonded 0° ply at the specimen overlap location for the INT0 specimen: a) stress field for different mesh densities along the width and length in the overlap area, and b) stress field for different mesh densities through the thickness of the adhesive and adherend plies.

The displacement between the two tabs measured from the experiments at the onset of failure in the adherend (i.e., maximum applied tensile load in Figure 5.7) was compared to that predicted by the finite element models for each SLJ specimen (Table 5.3). The predicted

displacements deviated from the experimental data by ≤ 11%, which was deemed acceptable for the purposes of predicting the ply level stresses in the adherends of the SLJ specimens.

Recall that a linear elastic response was assumed for the CFRP adherend and adhesive in the presented numerical model of the SLJ specimens. The assumed linear elastic response of the CFRP adherends was justified based on the behaviour reported in Refs. [42, 134], as well as the observations that damage initiation in the adherends occurred at the peak applied load immediately prior to final failure. Also, the assumed linear elastic response of the adhesive was also justified since the joint failure mode of SLJ specimens comprised of failure of the adherend without any interfacial or adhesive failure, while there was no plastic deformation or damage in the adhesive.

Table 5.3. Experimentally obtained and numerically predicted displacements at onset of damage (i.e. peak tensile load) for each SLJ specimen. The errors correspond to the predicted displacements.

Specimen	Displacement at Onset of Damage (mm)		Error (%)
	Simulation	Experiment	
SP	0.48	0.54	11.0
INT0	0.61	0.58	5.80
INT45	0.60	0.59	0.14
INT90	0.41	0.40	2.10

The predicted local stress distributions across the width of the adherend plies of the SP specimen at the end of the overlap region revealed that only the first 0^o ply adjacent to the adhesive layer achieved conditions to promote local matrix cracking (Figure 5.10). In particular, both in-plane transverse (σ_2) and out-plane transverse (σ_3) normal stresses exceeded the ply transverse strength of 51.9 MPa (Figure 5.10a). As observed on the fracture surfaces of the specimens, a thin layer of epoxy along with some fibres from the surface of the first 0°

ply adjacent to the adhesive, which was evident by the black lines observed on the purple region (indicated with yellow dash lines in Figure 5.3a), were removed from one adherend. Moreover, the magnitude of shear stresses were well below the corresponding ply strengths (Figure 5.10b). Therefore, it can be concluded that the matrix crack near the surface of the 0° ply adjacent to the adhesive was primarily driven by the out-of-plane transverse normal stress σ_3 (i.e. Mode I crack opening).

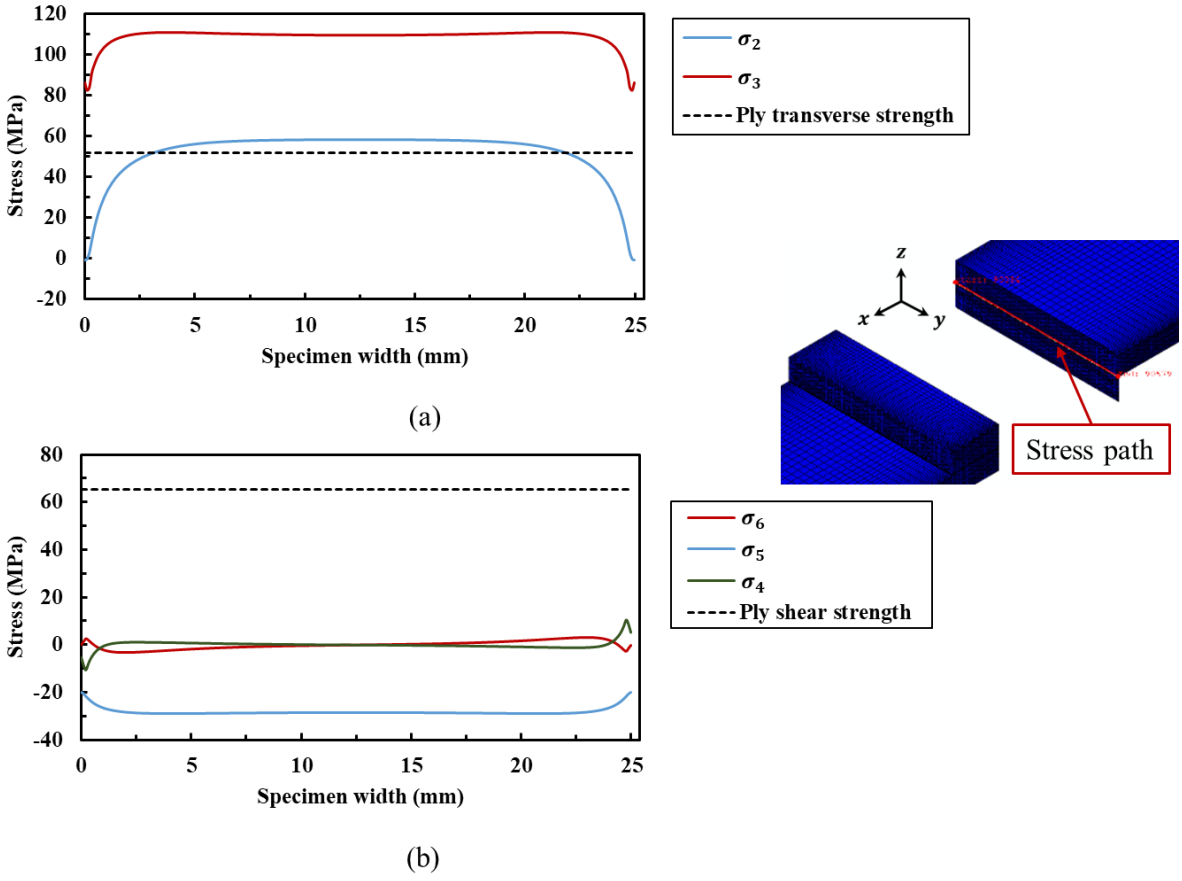

Figure 5.10. Widthwise stress distribution for the first 0° ply of the SP specimen comprising an adherend with a $[\mathbf{0}_7]$ stacking sequence: (a) normal stresses (σ_2 and σ_3), and (b) shear stresses (σ_4, σ_5 and σ_6). The local stresses are determined in the local coordinate system, where direction 1 corresponds to the fibre direction.

For the INT0 specimen with adherends comprising a $[0/\pm45/90]_s$ ply stacking sequence, both in-plane transverse (σ_2) and out-plane transverse (σ_3) normal stresses in the first 0° ply exceeded the ply transverse strength (Figure 5.11a). A thin layer of epoxy near the surface of the first 0° ply in one adherend was removed (Figure 5.12a), which was driven by σ_3 (i.e. Mode I). In addition, the transverse stresses (σ_2) was sufficiently large to promote local through-thickness intra-ply matrix cracking that was also observed in some specimens (Figure 5.12b). Similar to the SP specimen, the magnitude of shear stresses for the INT0 specimen were notably lower the corresponding ply strength (Figure 5.11b).

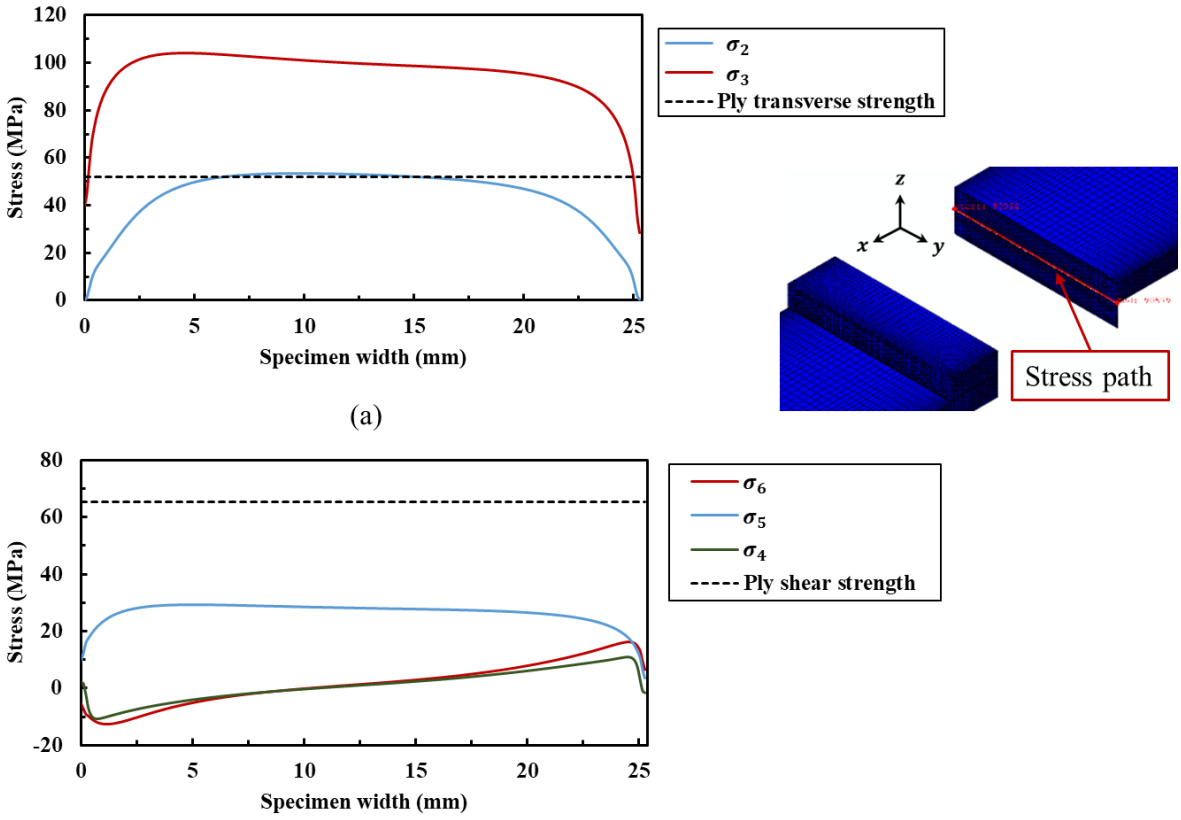

Figure 5.11. Widthwise stress distribution for the first 0° ply of the INT0 specimen comprising an adherend with a $[0/\pm45/90]_s$ stacking sequence: (a) normal stresses (σ_2 and σ_3), and (b) shear stresses (σ_4, σ_5 and σ_6). The local stresses are determined in the local coordinate system, where direction 1 corresponds to the fibre direction.

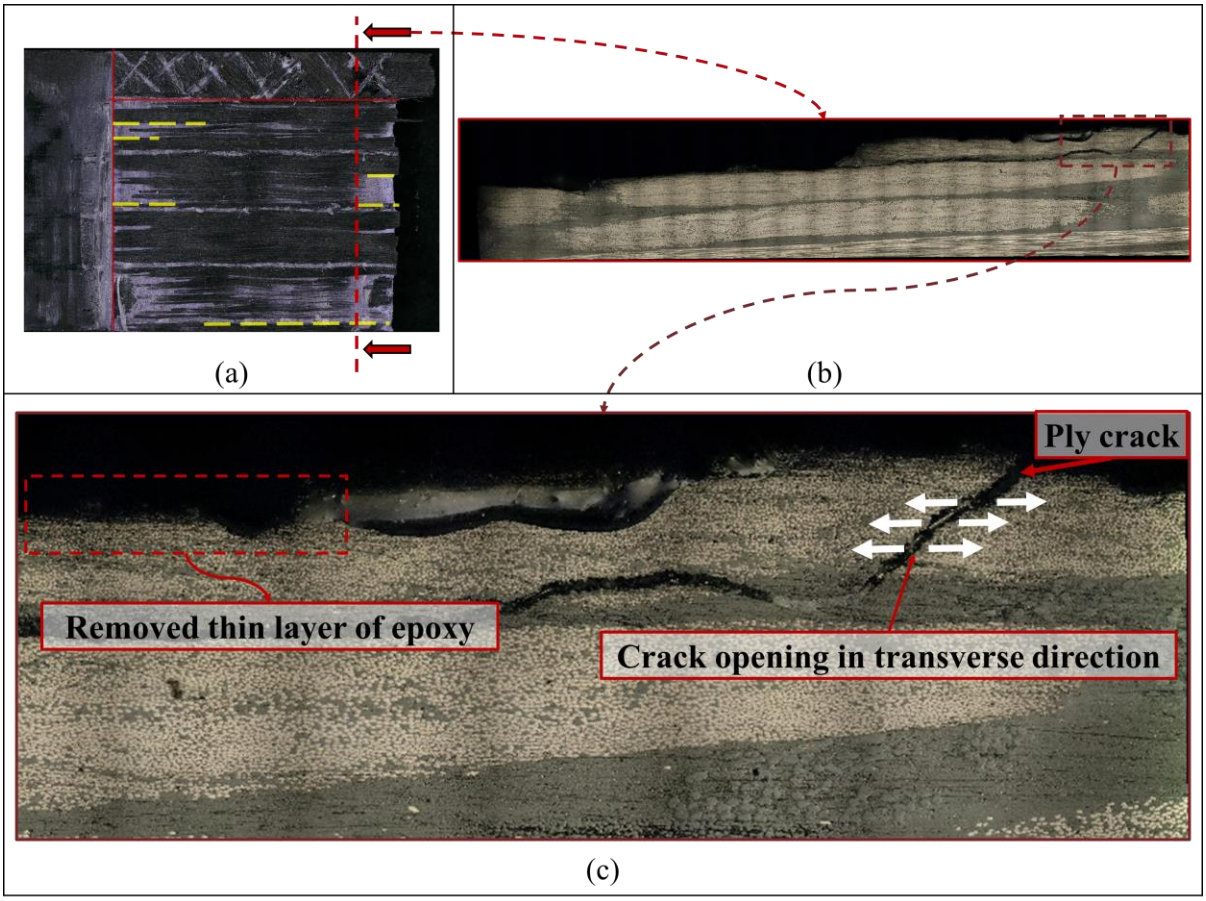

Figure 5.12. Post-test images of the INT0 specimen comprising an adherend with a $[\mathbf{0}/\pm\mathbf{45}/\mathbf{90}]_s$ stacking sequence: (a) the specimen fracture surface, (b) the adherend cross section, and (c) a magnified image taken from the adherend cross-section.

The local stress fields for the INT45 specimen with adherends comprising a $[45/90/0/-45]_s$ ply stacking sequence revealed that the 45° ply bonded to the adhesive layer and the adjacent 90° ply achieved conditions to promote local through-thickness matrix cracking (Figure 5.13). As observed on the fracture surface of the INT45 specimens (Figure 5.14), matrix cracking occurred in the 45° ply outside the overlap area and through-thickness matrix crack was observed in the 90° ply at the end of the overlap area. It could be concluded

that matrix cracks initiated in the 45° ply outside the overlap area due to the combination of high transverse normal stresses (σ_2) and in-plane shear stresses (σ_6) (i.e., mixed Mode I and Mode II). Matrix cracking in the 90° ply was driven primarily by the high transverse normal stresses (σ_2). Furthermore, removal of a thin layer of epoxy of the 0° ply near the interface with the 90° ply was observed within the overlap area (Figure 5.14, similar to the $[0_7]$ and $[0/\pm 45/90]_s$ laminates). However, the predicted out-of-plane normal stresses (σ_3) in the 0° ply were less than the corresponding ply strength (Figure 5.13a). The existence of through-thickness matrix cracks in the 45° and 90° plies would tend to promote out-of-plane stress concentrations at the interface between the 90° and 0° plies, which was not captured in the model since damage was not considered. Thus, failure of the 0° ply was driven by the combination of damage in the adjacent 45° and 90° plies, the high out-of-plane normal stresses (σ_3) in the ply and possibly the out-of-plane shear stress (σ_5).

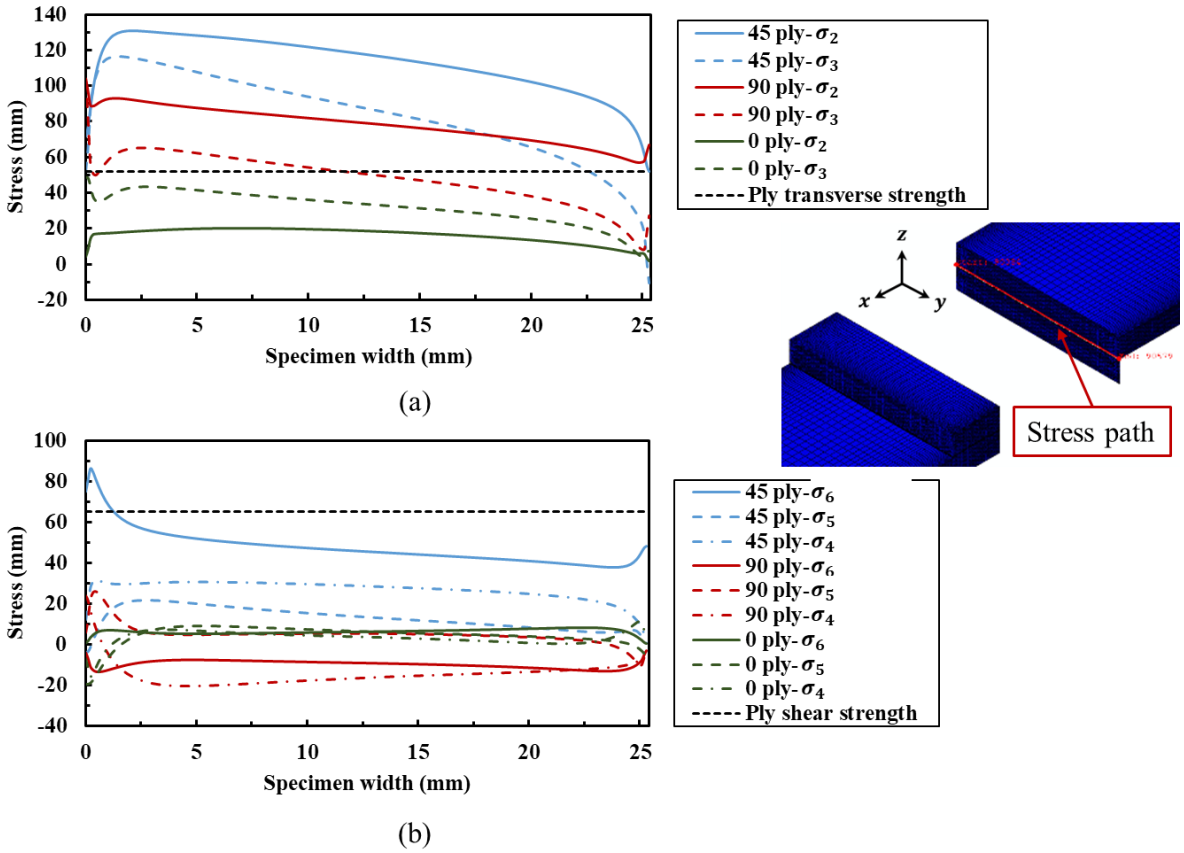

Figure 5.13. Widthwise stress distribution for the 45°, 90° and 0° plies of the INT45 specimen comprising an adherend with a $[\mathbf{45/90/0/-45}]_s$ stacking sequence: (a) normal stresses (σ_2 and σ_3), and (b) shear stresses (σ_4, σ_5 and σ_6). The local stresses are determined in the local coordinate system, where direction 1 corresponds to the fibre direction.

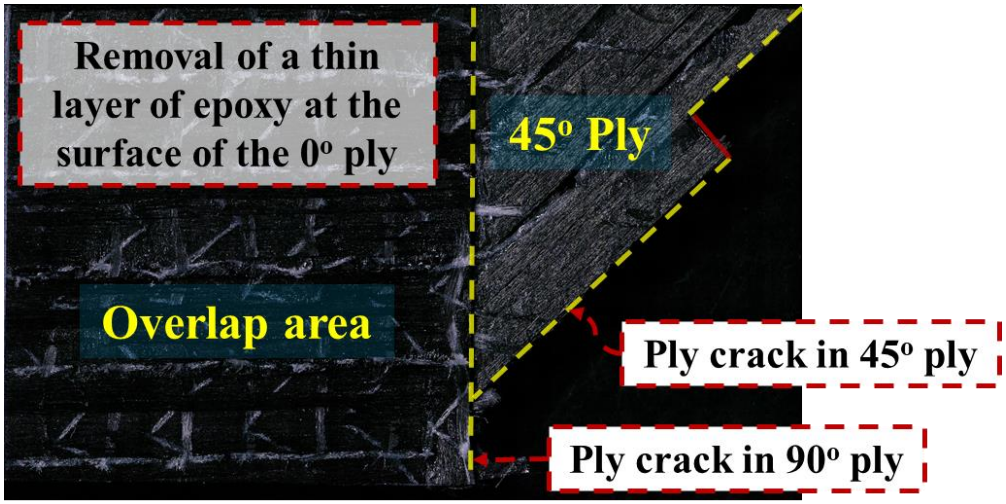

Figure 5.14. The fracture surface of the INT45 specimen comprising an adherend with a $[\mathbf{45/90/0/-45}]_s$ stacking sequence.

The predicted local stress distribution across the width of the INT90 specimen adherend comprising a $[90/\mp 45/0]_s$ ply stacking sequence indicated that only the first 90° ply adjacent to the adhesive layer achieved conditions to promote local through-thickness matrix cracking (Figure 5.15). However, it was observed on the fracture surfaces of the INT90 specimen that matrix cracking occurred in both the 90° and -45° plies (Figure 5.16). It could be concluded that the existence of matrix cracks would cause stress concentrations at the ply interfaces, which would lead to delamination between the 90° and -45° plies as well as between the -45° and 45° plies (Figure 5.16b).

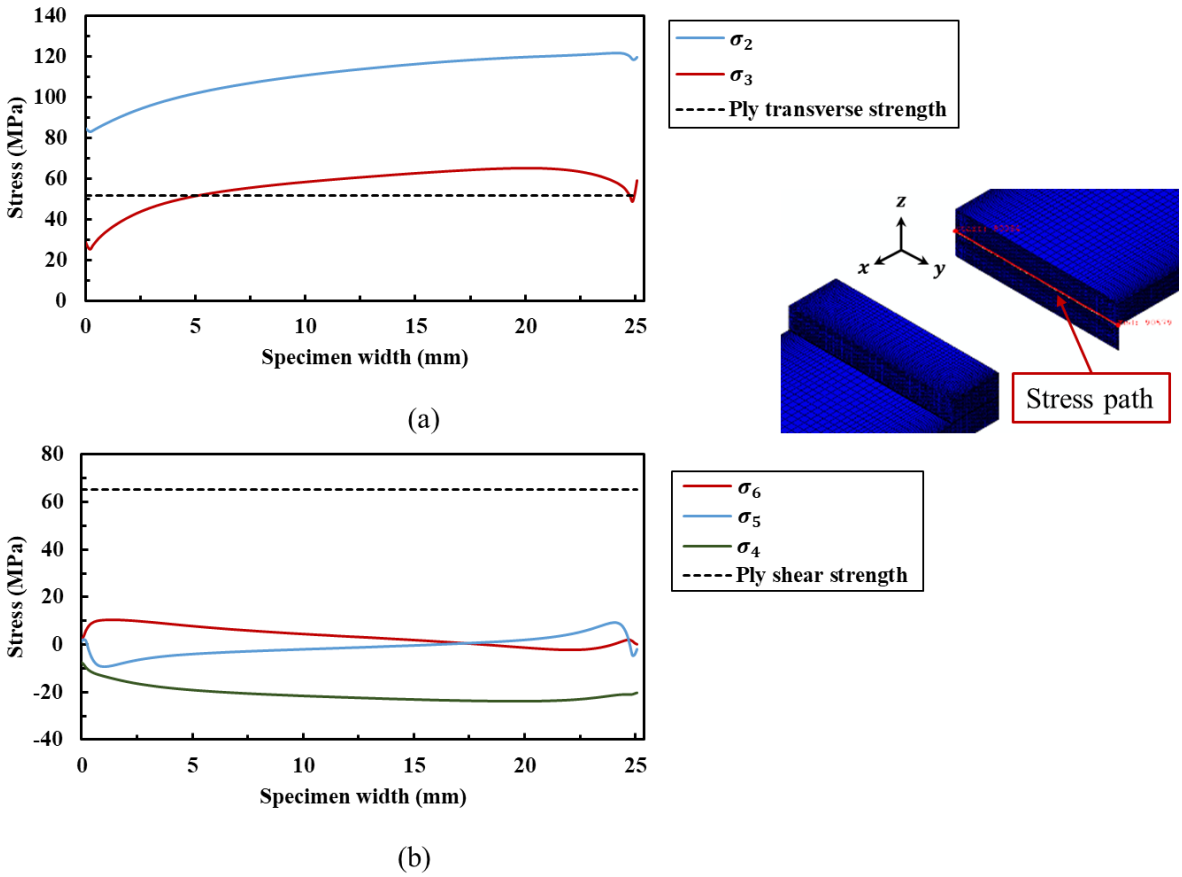

Figure 5.15. Widthwise stress distribution for the first 90° ply of the INT90 specimen comprising an adherend with a $[\mathbf{90/\mp 45/0}]_s$ stacking sequence: (a) normal stresses (σ_2 and σ_3), and (b) shear stresses (σ_4, σ_5 and σ_6). The local stresses are determined in the local coordinate system, where direction 1 corresponds to the fibre direction.

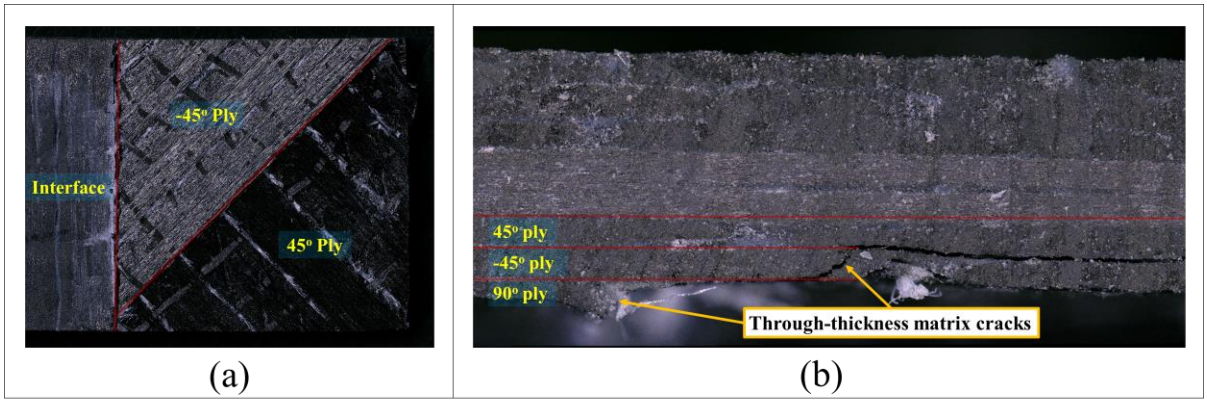

Figure 5.16. (a) The fracture surface of the INT90 specimen comprising an adherend with a $[\mathbf{90}/\mp\mathbf{45}/\mathbf{0}]_s$ stacking sequence and (b) an image taken from the longitudinal edge of the INT90 specimen.

5.2 Double Cantilever Beam Tests

5.2.1 Influence of Adherend Fiber Volume Fraction on Mode I Fracture

The first assessment aimed to determine the influence of the $[0_7]$ CFRP adherend fibre volume fraction on the Mode I fracture behaviour of the DCB test specimens. Accordingly, the force-displacement response and the critical SERR for specimens comprising an adherend with 45% (DCB-1) and 53% (DCB-2) fibre volume fraction were compared. Note that the bond-line thickness of the DCB specimens and the loading rate used for the tests were constant at 0.25 mm and 0.1 mm/sec, respectively.

Force-displacement response of the DCB specimens are presented in Figure 5.17. The 45% fibre volume fraction DCB test specimens (DCB-1) exhibited notable variation in the slope of the linear region of the force-displacement response (Figure 5.17a). The variation of these results was due to the inconsistency of the pre-crack length in the DCB specimens, where the range of pre-crack length was from 32.56 mm to 35.28 mm. However, the slope of the linear

region of the force-displacement response for the 53% fibre volume fraction DCB specimens (DCB-2) was more consistent (Figure 5.17b). In addition, crack propagation was more stable in the adhesive of the DCB-2 specimens compared to the DCB-1 specimens, which was evident by the rapid force drops in the force-displacement response.

The critical strain energy release rate at the initial crack length (G_{Ic}) was calculated for each specimen using the modified beam theory (Table 5.4, Appendix A). The average G_{Ic} value for the DCB-1 specimens was 1393 J/m^2 and increased to 1698 J/m^2 for the DCB-2 specimens. The resistance curve (R-curve) of DCB-2 specimens indicated that the G_I value was not influenced significantly by the crack length (Figure 5.18). Note that the R-curve of DCB-1 specimens was similar to DCB-2 specimens.

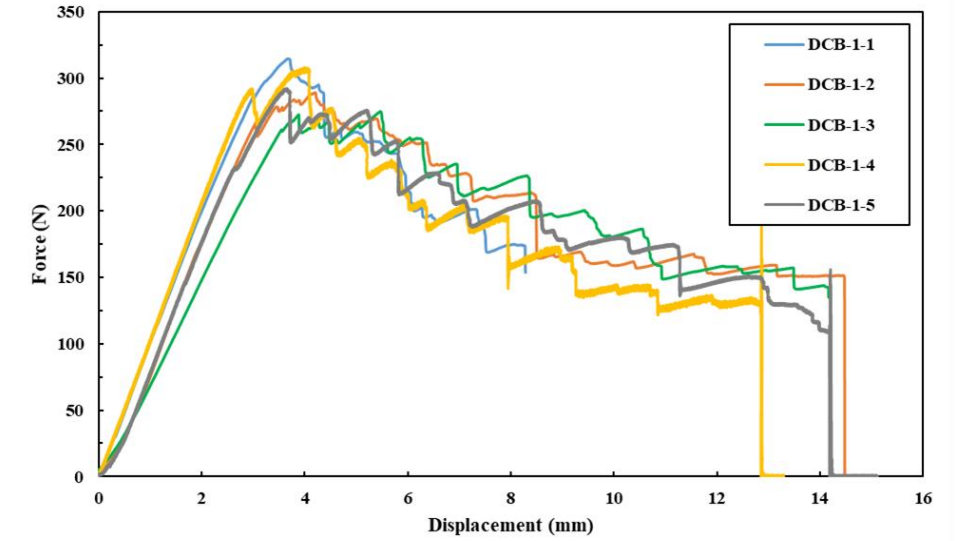

(a)

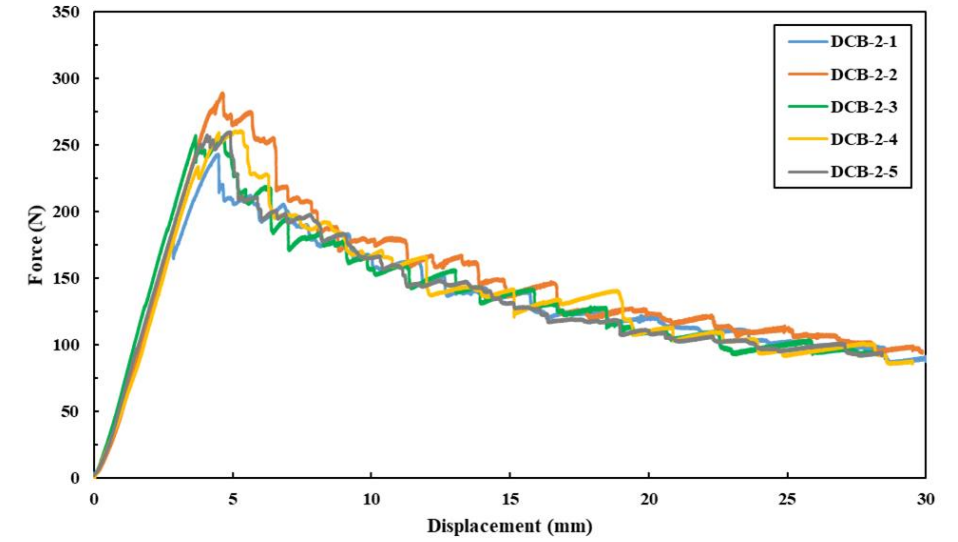

(b)

Figure 5.17. Force-displacement response for the DCB specimens comprising CFRP adherends with different fibre volume fractions: (a) 45% and (b) 53%.

Table 5.4. The critical SERR (G_{Ic}) of DCB specimens comprising CFRP adherends with 45% and 53% fibre volume fractions.

Adherend Fiber Volume Fraction (%)		DCB-1-1	DCB-1-2	DCB-1-3	DCB-1-4	DCB-1-5
45	G_{Ic} (J/m^2)	1292	1312	1346	1441	1569
	$G_{Ic_{avg}}$ (J/m^2) (±STV)	1393 (±92)				
		DCB-2-1	**DCB-2-2**	**DCB-2-3**	**DCB-2-4**	**DCB-2-5**
53	G_{Ic} (J/m^2)	1506	1880	1573	1857	1676
	$G_{Ic_{avg}}$ (J/m^2) (±STV)	1698 (±149)				

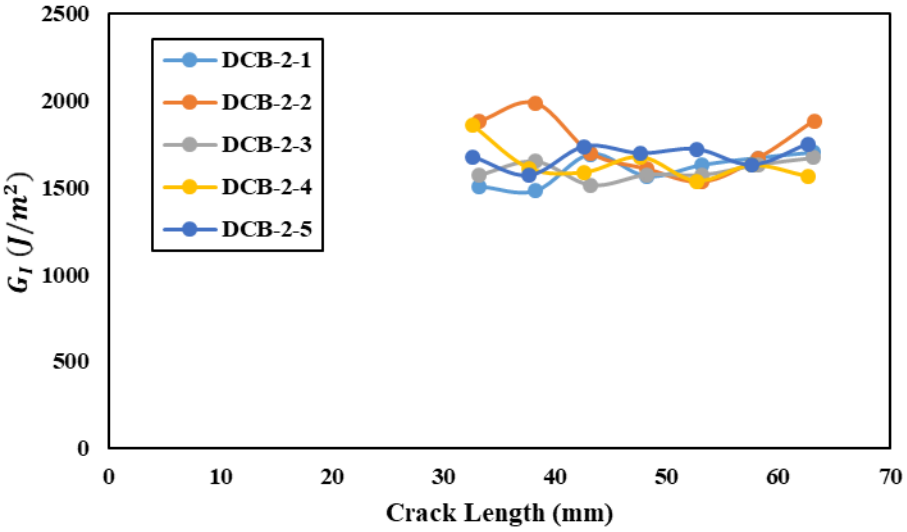

Figure 5.18. Resistance curve of DCB-2 specimens.

The fracture surfaces for both DCB-1 and DCB-2 specimens revealed that cohesive failure was the dominant failure mode (see purple regions in Figure 5.19). Moreover, it was observed in a few spots that a thin layer of epoxy was removed from the adherend (see gray and black regions in Figure 5.19). Overall, the CFRP adherend fibre volume fraction did not notably

influence the fracture surface morphology. Observation of DCB specimens during the experiment at different applied displacements indicated that the progression of crack propagation and damage was similar for both DCB-1 and DCB-2 specimens (Figure 5.20). The progression of damage indicated that crack was propagated through the adhesive layer which was evident from the purple regions observed on the fracture surfaces of DCB specimens (see purple regions in Figure 5.19). In addition, there seems to be some bridging between the adherends, which may be the removal of a thin layer of epoxy from the top surface of the 0° plies (see gray and black regions in Figure 5.19).

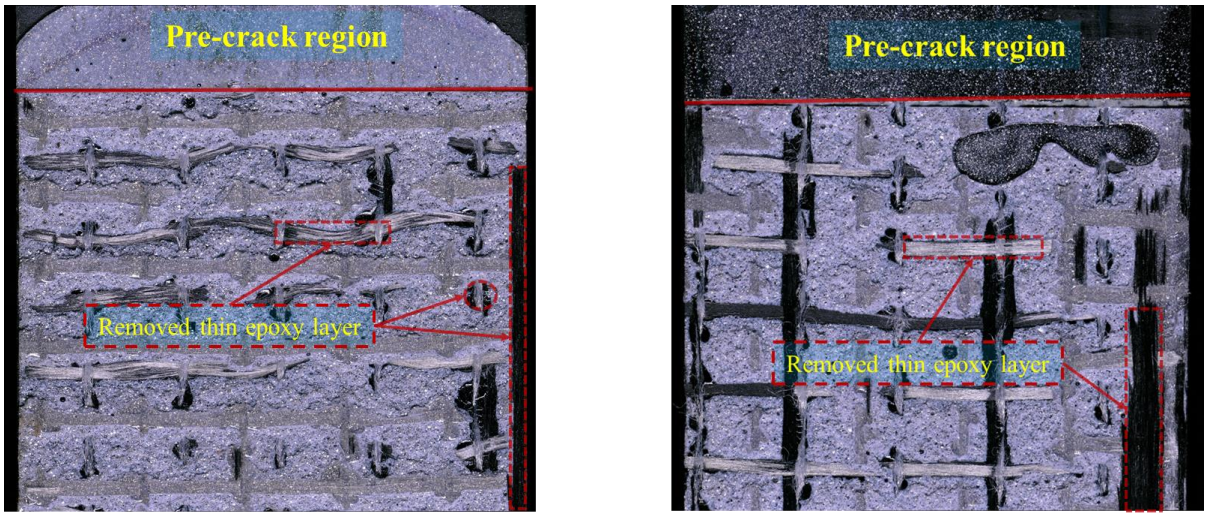

Figure 5.19. The fracture surfaces of DCB specimens comprising an adherend with a [0_7] stacking sequence with different fibre volume fraction: (a) 45% and (b) 53%.

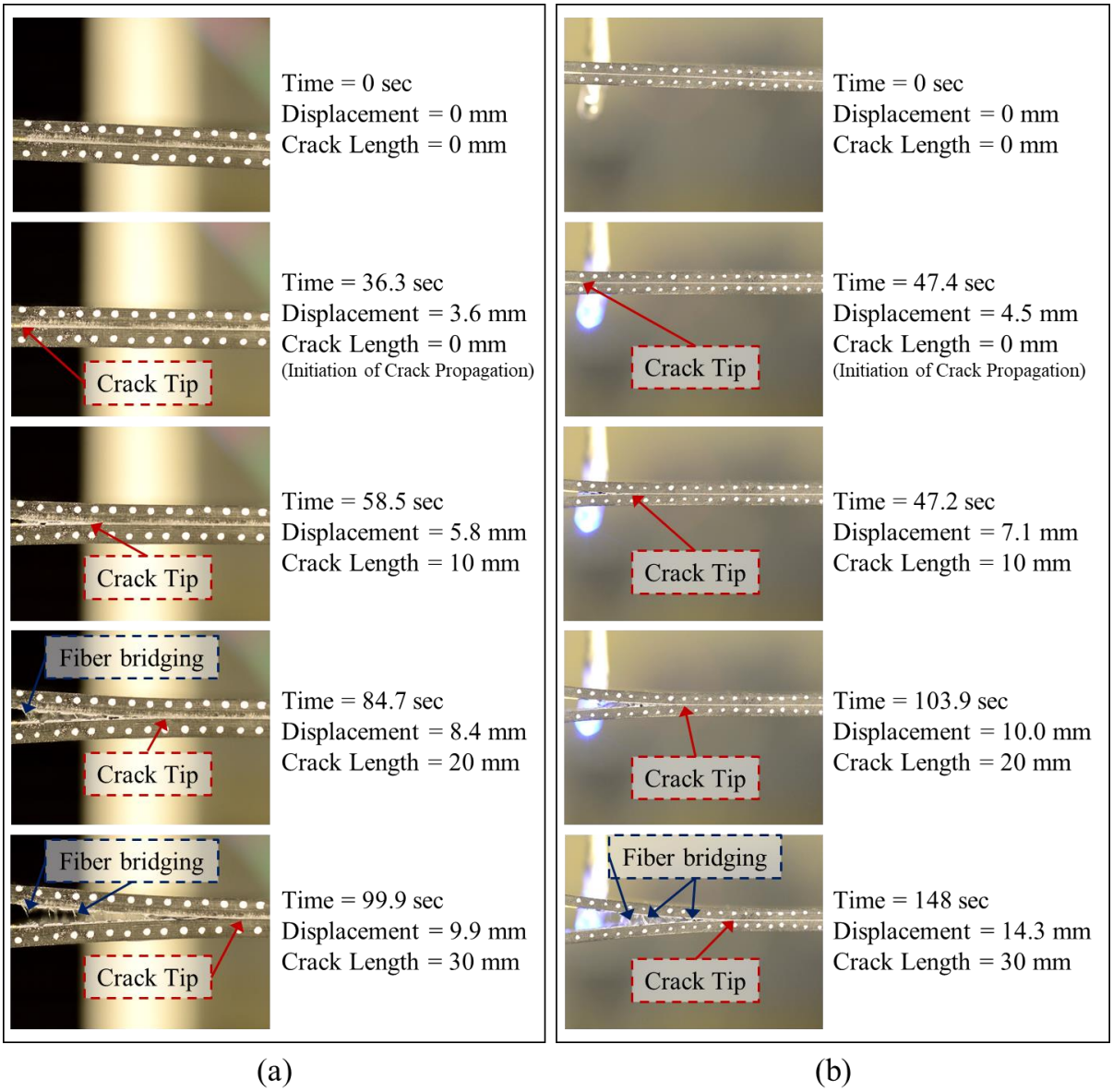

Figure 5.20. Side view of (a) DCB-1-1 and (b) DCB-2-1 at different applied displacements

5.2.2 Influence of Adhesive Bond-line Thickness on Mode I Fracture

The effect of bond-line thickness (DCB-3: 0.4 mm, DCB-4: 0.65 mm) on Mode I fracture behaviour was assessed using force-displacement response and critical SERR of DCB

specimens. It should be noted that the CFRP adherend volume fraction and the applied loading rate for both sets of DCB specimens were constant at 53% and 0.1 mm/sec, respectively.

The force-displacement response for specimens DCB-3 and DCB-4 is presented in Figure 5.21. The slope of the linear region of the force-displacement response was consistent for both sets of DCB specimens, which was attributed to a low variation in the measured pre-crack length for all test specimens (see Table 3.5 in Section 3.3.1). Stable crack propagation was observed in the adhesive for both DCB-3 and DCB-4 specimens, with average G_{Ic} values of 1763 J/m^2 and 1949 J/m^2, respectively (Table 5.5, Appendix A). Note that the R-curves for DCB-3 and DCB-4 specimens were similar in form to the R-curves for the DCB-2 specimens (see Figure 5.18).

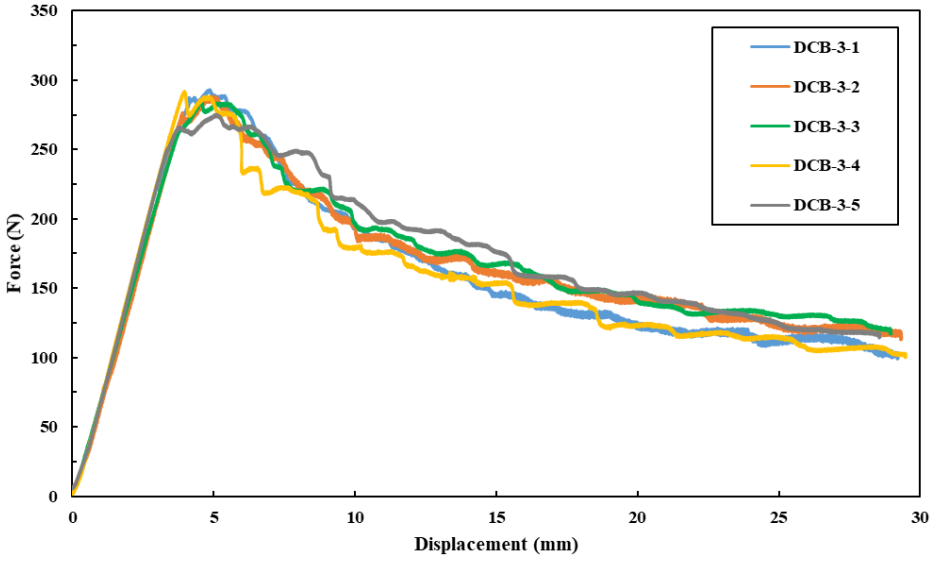

(a)

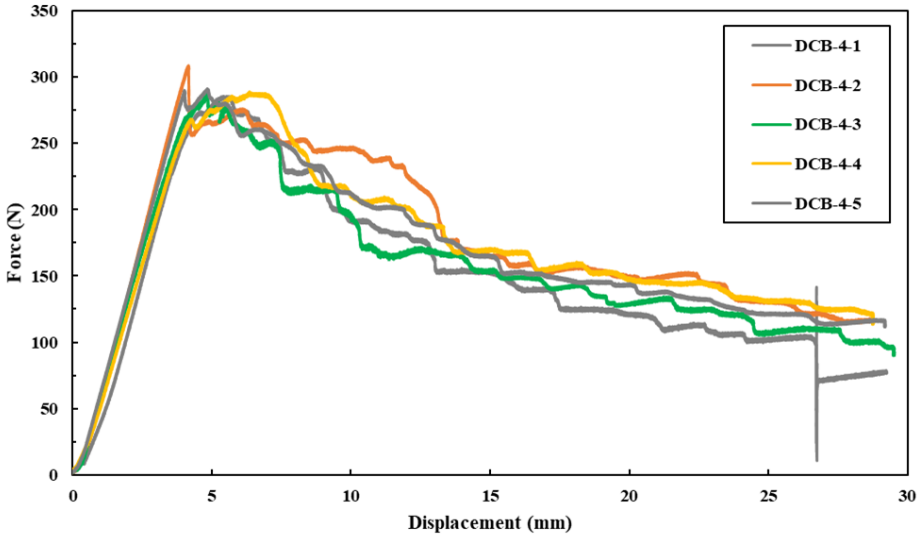

(b)

Figure 5.21. The force-displacement response of the DCB specimens with different adhesive bond-line thicknesses: (a) 0.4mm and (b) 0.56 mm.

Table 5.5. The critical SERR (G_{Ic}) of DCB specimens with indicated adhesive bond-line thicknesses.

Bond-line Thickness (mm)		**DCB-2-1**	**DCB-2-2**	**DCB-2-3**	**DCB-2-4**	**DCB-2-5**
0.25	$G_{Ic}\ (J/m^2)$	1506	1880	1573	1857	1676
	$G_{Ic_{avg}}\ (J/m^2)$ **(±STV)**	1698 (±149)				
		DCB-3-1	**DCB-3-2**	**DCB-3-3**	**DCB-3-4**	**DCB-3-5**
0.4	$G_{Ic}\ (J/m^2)$	1759	1754	1787	1785	1724
	$G_{Ic_{avg}}\ (J/m^2)$ **(±STV)**	1763 (±26)				
		DCB-4-1	**DCB-4-2**	**DCB-4-3**	**DCB-4-4**	**DCB-4-5**
0.65	$G_{Ic}\ (J/m^2)$	1813	2167	1915	1899	1814
	$G_{Ic_{avg}}\ (J/m^2)$ **(±STV)**	1949 (±134)				

Observation of the fracture surfaces of the DCB-3 specimens revealed that cohesive failure was the dominant failure mode (see purple regions in Figure 5.22a), while in few spots a thin epoxy layer was removed from the CFRP adherend (see gray and black regions in Figure 5.22a). The failure mode of the DCB-4 specimens with 0.65 mm bond-line thickness (Figure 5.22b) was similar to the DCB-3 specimens. It should be noted that the progression of damage for both DCB-3 and DCB-4 were similar to DCB-2 specimens (see Figure 5.19).

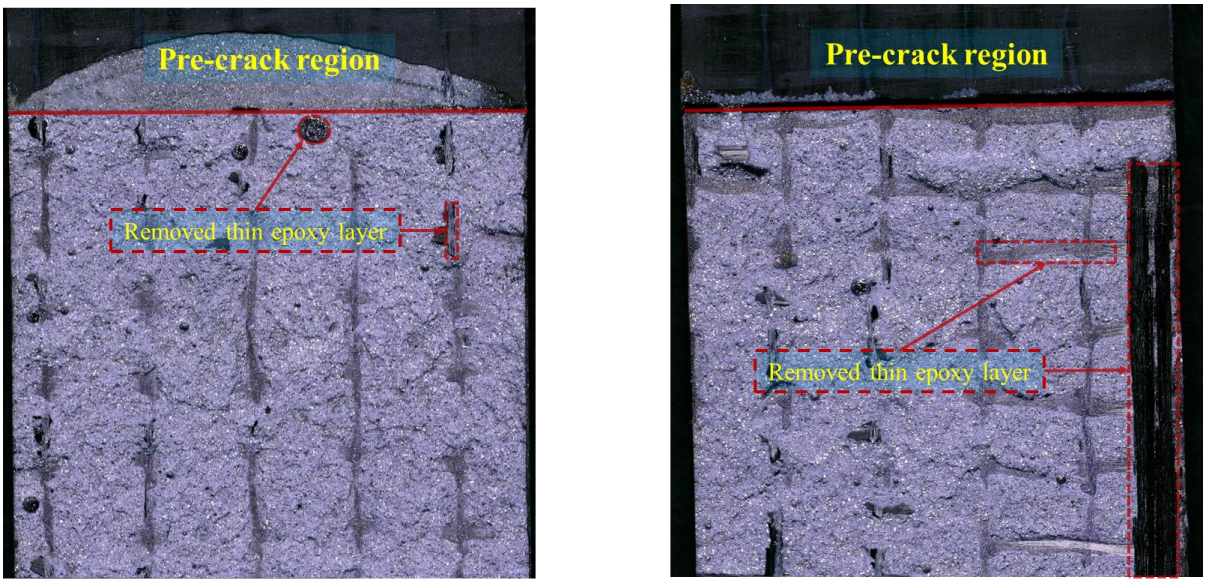

Figure 5.22. The fracture surfaces of the DCB specimens with different bond-line thicknesses: (a) 0.4 mm and (b) 0.65 mm.

5.2.3 Influence of Loading Rate on Mode I Fracture

The influence of loading rate on the Mode I fracture behaviour of DCB specimens was assessed using the force-displacement response and the critical SERR of DCB specimens, with loading rates of 5.0 mm/s (DCB-5) and 15 mm/s (DCB-6). Note that the CFRP adherend fibre volume fraction and the adhesive bond-line thickness of the DCB specimens were constant at 53% and 0.4 mm, respectively.

Four repeated tests were conducted for the DCB-5 specimens (Figure 5.23a), while three repeated tests were conducted for the DCB-6 specimens (Figure 5.23b). For the DCB-6 specimens, an unstable crack propagation was observed in the adhesive, which was evident in the rapid force drops from the force-displacement response (Figure 5.23b). The critical SERR at initial crack length (G_{Ic}) was calculated for each DCB specimen using the modified beam

theory (Table 5.6, Appendix A). The average G_{Ic} value for the DCB specimens with loading rates of 5.0 mm/s and 15.0 mm/s were 2044 J/m^2 and 2138 J/m^2, respectively. The R-curves for both DCB-5 and DCB-6 specimens were similar in form to the DCB-2 specimens (see Figure 5.18).

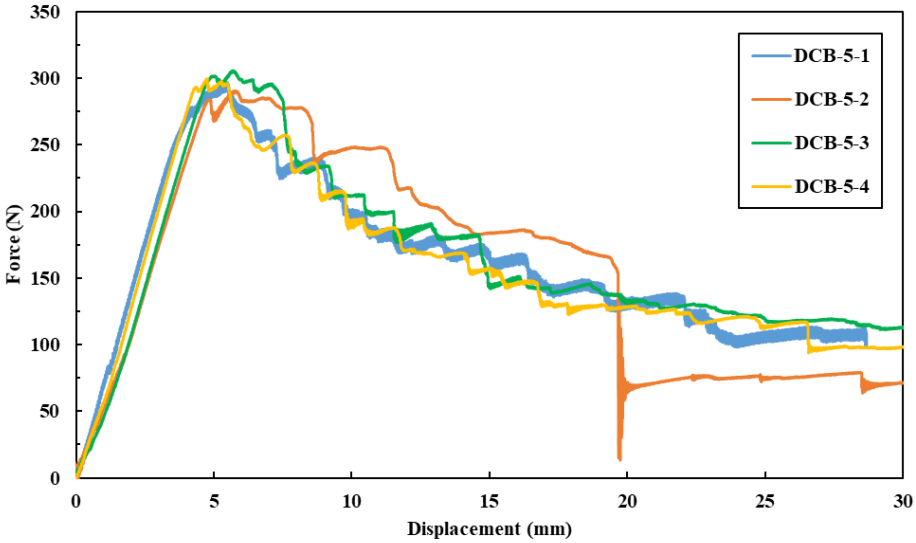

(a)

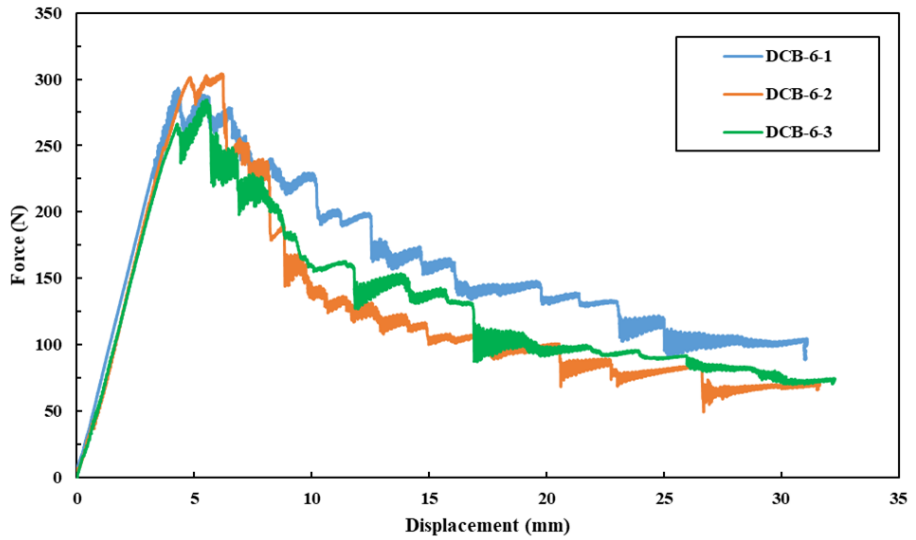

(b)

Figure 5.23. The force-displacement response of the DCB specimens with different loading rates (crosshead speed): (a) 5.0 mm/s and (b) 15.0 mm/s.

Table 5.6. The critical SERR (G_{Ic}) of the DCB specimens with indicated loading rates (crosshead speed).

Loading Rate (mm/s)		**DCB-3-1**	**DCB-3-2**	**DCB-3-3**	**DCB-3-4**	**DCB-3-5**
0.1	G_{Ic} (J/m^2)	1759	1754	1787	1785	1724
	$G_{Ic_{avg}}$ (J/m^2) **(±STV)**	1763 (±26)				
		DCB-5-1	**DCB-5-2**	**DCB-5-3**	**DCB-5-4**	
5.0	G_{Ic} (J/m^2)	1938	2025	2066	2146	
	$G_{Ic_{avg}}$ (J/m^2) **(±STV)**	2044 (±75)				
		DCB-6-1		**DCB-6-2**	**DCB-6-3**	
15.0	G_{Ic} (J/m^2)	2189		2165	2061	
	$G_{Ic_{avg}}$ (J/m^2) **(±STV)**	2138 (±56)				

The crack length-time response was generated for the DCB specimens with different loading rates to determine the influence of loading rate on the crack propagation speed (Figure 5.22). The results indicated that the average crack propagation speed increased from 0.31 mm/s to 15.45 mm/s and 53.59 mm/s when the loading rate of the DCB test increased from 0.1 mm/s to 5.0 mm/s and 15 mm/s, respectively.

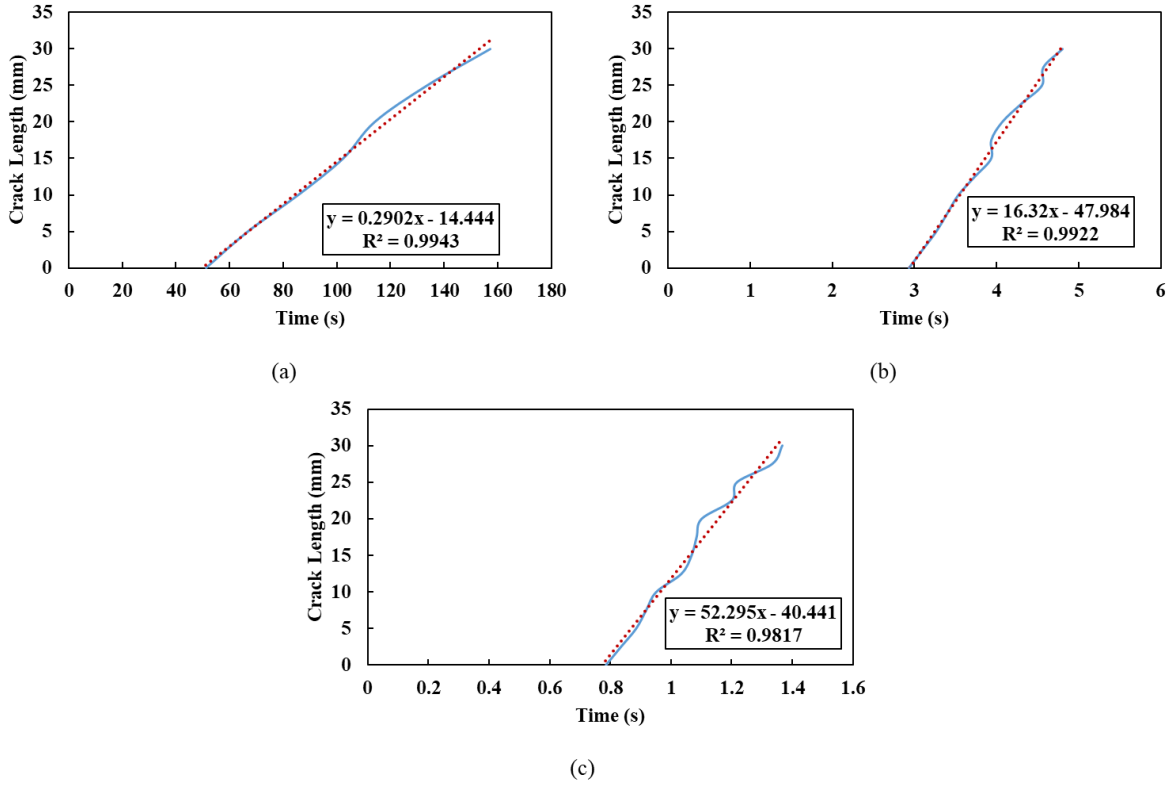

Figure 5.24. Crack length-time response of the DCB specimens with a loading rate of: (a) 0.1 mm/s (DCB-4-1), (b) 5.0 mm/s (DCB-5-1), and (c) 15.0 mm/s (DCB-6-1).

Similar to the previous DCB specimens, observation on the fracture surfaces for both DCB specimens with higher loading rates (i.e. 5.0 mm/s and 15.0 mm/s) revealed that cohesive failure was the dominant failure mode (see purple regions in Figure 5.25). However, removal of the thin layer of epoxy from the surface of CFRP adherend for the DCB specimens with higher loading rate was more severe compared to that for the DCB specimen with the loading rate of 0.1 mm/s (see Figure 5.22a). Note that the progression of damage for both DCB-3 and DCB-4 were similar to DCB-2 specimens (see Figure 5.19).

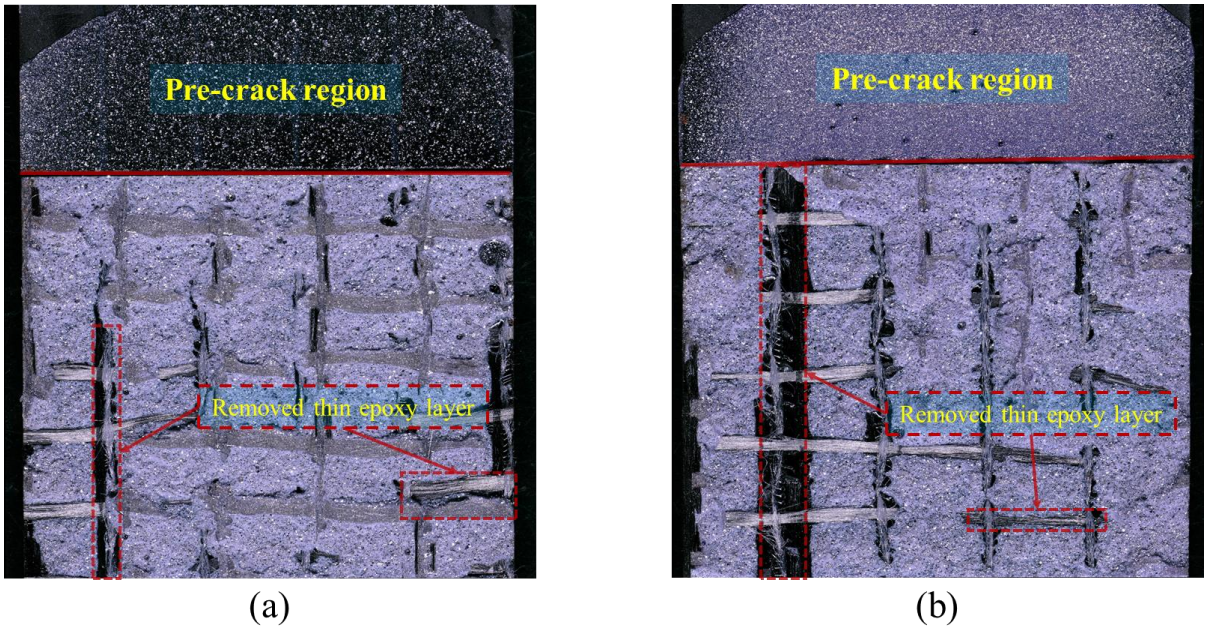

Figure 5.25. The fracture surfaces of the DCB specimens with different loading rates: (a) 5.0 mm/s and (b) 15.0 mm/s.

5.2.4 Inverse Approach to Determine Mode I Traction-Separation Response

The finite element model described in Section 4.2 was used to simulate the DCB specimens for the purpose of calibrating the Mode I traction-separation response of the adhesively bonded joint. The experimentally obtained G_{Ic} values were used and the goal of the inverse analysis was to determine the remaining traction-separation parameters (i.e., peak traction and initial stiffness) for an assumed bilinear traction-separation law.

5.2.4.1 Mesh Sensitivity Study

Elements with a width of 0.25 mm and four different lengths, including 0.05, 0.125, 0.25 and 0.5 mm, were used to study the influence of mesh element size. Moreover, the value of the viscosity coefficient for the cohesive elements was set to either 0 or 0.001 for each mesh

configuration, which was based on the recommendations from [135]. The predicted force-displacement response was not sensitive for mesh element lengths of 0.25 mm or lower (Figure 5.26). Thus, the numerical models for the DCB test specimens were meshed with 0.25 mm x 0.25 mm elements.

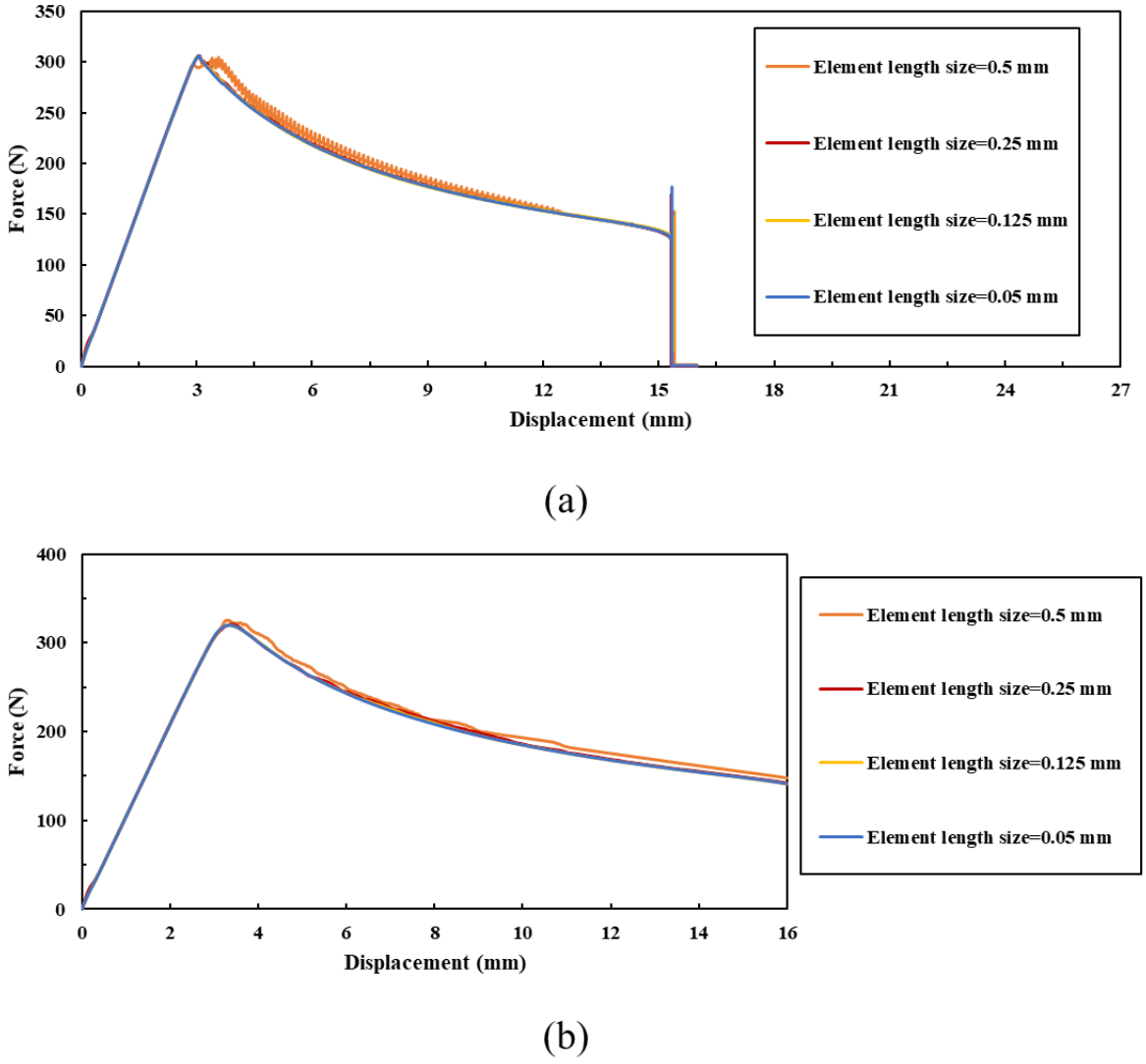

Figure 5.26. The influence of element length size on the predicted force-displacement response for finite element models with a cohesive element viscosity coefficient set to: (a) 0, and (b) 0.001. The properties set for the cohesive elements in these simulations were initial stiffness = 2585 MPa, peak traction = 53.38 MPa and $\boldsymbol{G_{Ic}}$ = 1393 $\boldsymbol{J/m^2}$.

5.2.4.2 Parametric Study of the Cohesive Properties

A parametric study was conducted to investigate the influence of the peak traction and initial stiffness on the force-displacement response of the DCB specimens.

The DCB specimen (DCB-1) was simulated using four different peak tractions for the cohesive elements including 5, 12.5, 25 and 53.38 MPa (see Section 4.2). The numerical results indicated that the initiation of nonlinear force-displacement response was influenced by the peak traction, while increasing the peak traction led to increasing the magnitude of force and displacement at the point of deviation from linearity in force-displacement response (Figure 5.27). Also, the predicted force-displacement response for the case when the viscosity coefficient was set to 0 revealed that the crack propagation or post-peak region was not sensitive to chosen peak traction of the cohesive elements. As a result, the viscosity coefficient for the cohesive elements was set to 0 for the remaining simulations. Moreover, by decreasing the peak stress from 53.38 MPa to 25 MPa, initiation of nonlinearity in the pre-peak region occurred earlier. However, despite an approximate 50% reduction in the specified peak stress, the difference between the predicted and experimental force-displacement response was not significant.

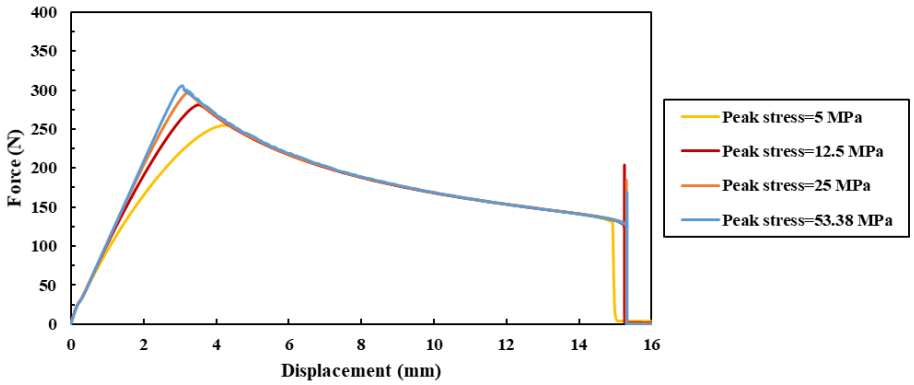

(a)

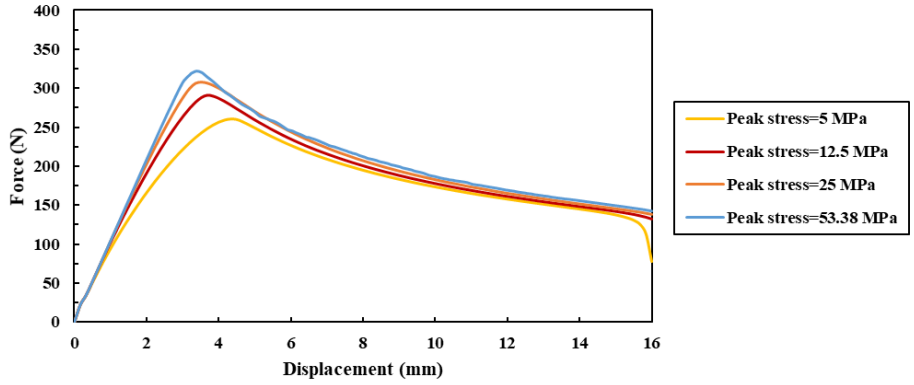

(b)

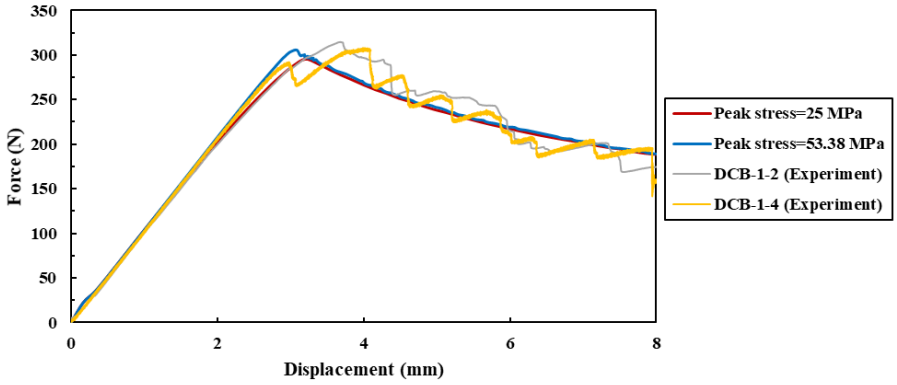

(c)

Figure 5.27. The influence of peak traction on the predicted force-displacement response for the DCB-1 specimen with G_{Ic} = 1393 J/m^2, initial stiffness of 2598 MPa, cohesive element viscosity coefficient set to: (a) 0, and (b) 0.001, and (c) a comparison of the experimental and numerical force-displacement response for the DCB-1 specimens (viscosity coefficient set to 0).

As noted in Section 4.2, the DCB specimen was simulated using five different initial stiffnesses values for the cohesive elements, including 500, 1000, 1500, 2585 and 4000 MPa. The numerical results revealed that the finite element model with the first two initial stiffnesses (i.e. 500 and 1000 MPa), could not predict the force-displacement response of the DCB specimen (Figure 5.28a). However, by employing the last three initial stiffnesses (i.e. 1500, 2585 and 4000 MPa), the finite element model predicted the expected force-displacement response. The numerical results of the last three finite element models indicated that the predicted force-displacement response was not sensitive to the initial stiffness of cohesive elements (Figure 5.28b).

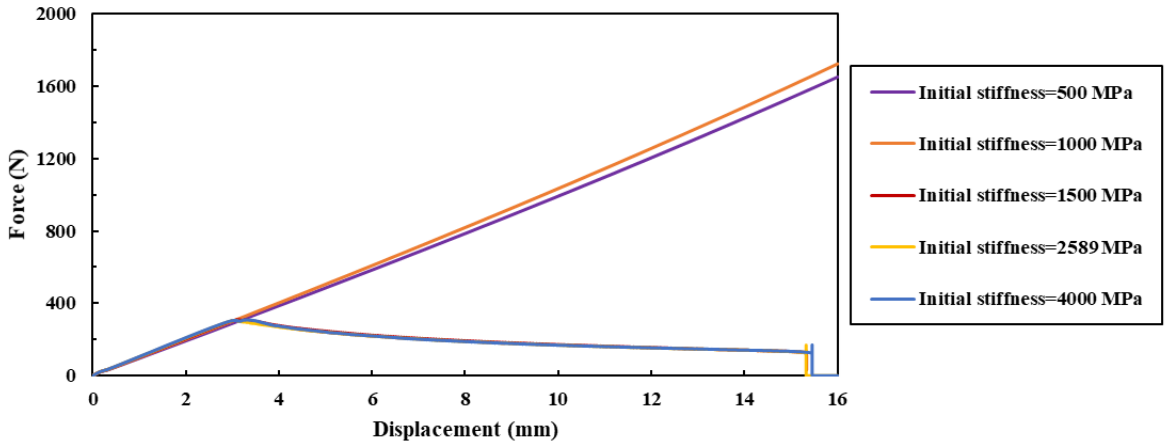

(a)

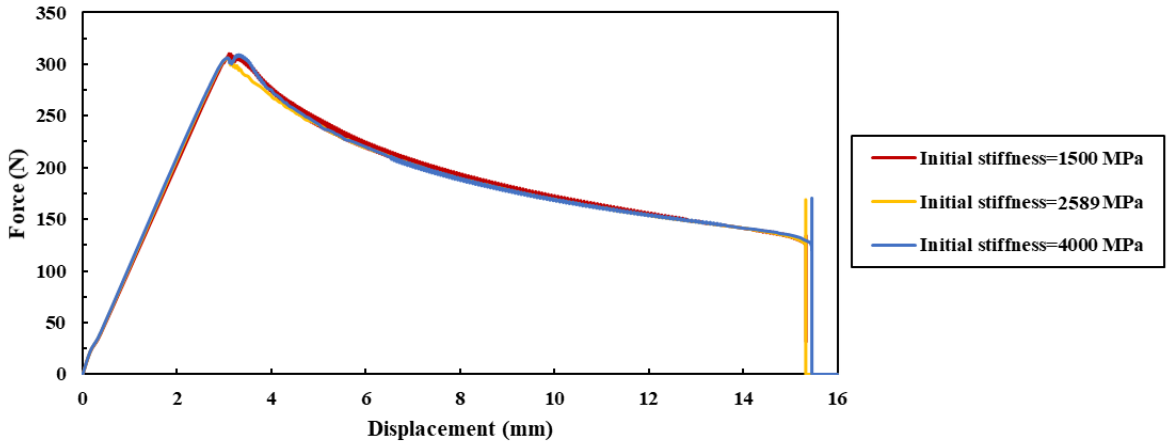

(b)

Figure 5.28. The influence of initial stiffness on the predicted force-displacement response for specimen DCB-1 with G_{Ic} = 1393 J/m^2, peak stress of 53.38, cohesive element viscosity coefficient set to 0: (a) five different initial stiffnesses, and (b) three initial stiffnesses (plot magnified).

5.2.4.3 Comparison between the Experimental and Numerical Results

The numerical result of the parametric study of the cohesive properties (see Sections 5.2.4.1 and 5.2.4.2) revealed that the force-displacement response of the DCB specimen was insensitive to the values of the initial stiffness considered. In addition, the post-peak region of

the force-displacement response of the DCB specimen was similarly insensitive to the values of the peak traction considered and the influence of peak traction ranging from 25 MPa to 53.38 MPa on the pre-peak region of the force-displacement response of the DCB specimen was insignificant. Thus, it was concluded that the initial stiffness and peak traction could not be determined accurately using the finite element analysis of the DCB specimen. As a result, as it was mentioned in Section 2.6, it was concluded that an additional experiment is required to extract the accurate value of initial stiffness and peak traction. The cohesive properties of the IRSA 07333 adhesive were determined by Watson et al. [119] using the RDCB test. Therefore, the initial stiffness and peak traction adapted from the result of the RDCB tests presented by Waston et al. [119] and the critical SERR calculated from the result of the DCB tests presented in this project were employed to generate the bilinear traction-separation response (Figure 5.29) to define the cohesive elements used in the simulation of the DCB specimens (Table 5.7).

Table 5.7. Cohesive material properties of IRSA 07333 adhesive used for the simulation of the DCB specimens.

Specimen Code	**Initial Stiffness (MPa)**	**Peak Traction (MPa)**	**Critical SERR ($G_{Ic_{avg}}$) ($\mathbf{J/m^2}$)**
DCB-1	2589	53.38	1393
DCB-2	2589	53.38	1698
DCB-3	1762	51.24	1763
DCB-4	1259	48.72	1949

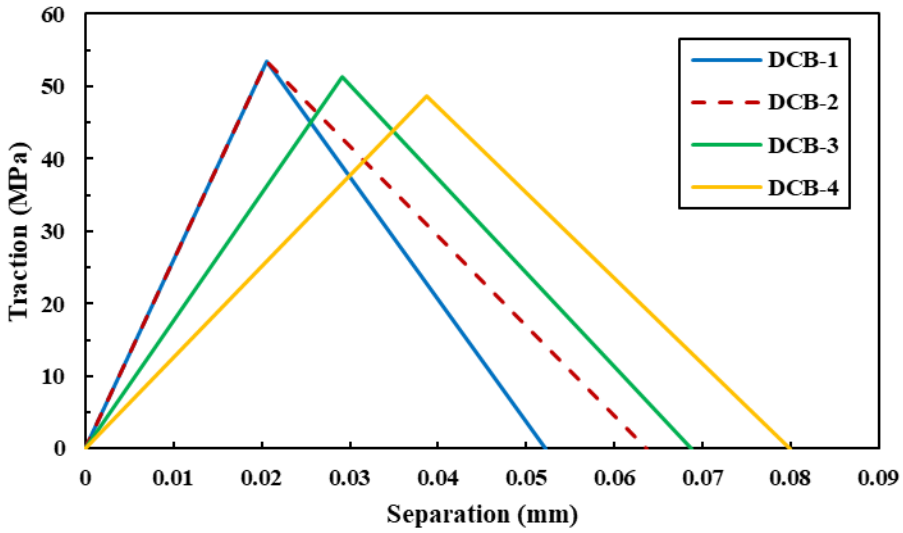

Figure 5.29. Bilinear traction-separation responses of IRSA 07333 adhesive used for the simulation of the DCB specimens.

In order to observe the influence of pre-crack length on the predicted force-displacement response, it was decided to simulate the DCB-1 specimens with three pre-crack lengths including 35.28 mm (specimen DCB-1-4), 32.56 mm (specimen DCB-1-3) and 33.45mm (specimen DCB-1). The numerical results indicated that the finite element model could predict the influence of pre-crack length on the force-displacement response of the DCB specimens (Figure 5.30). Moreover, based on the presented bilinear traction-separation response for each DCB specimen configuration (see Table 5.7), a comparison of the experimental and predicted force-displacement response revealed a good correlation (Figure 5.31).

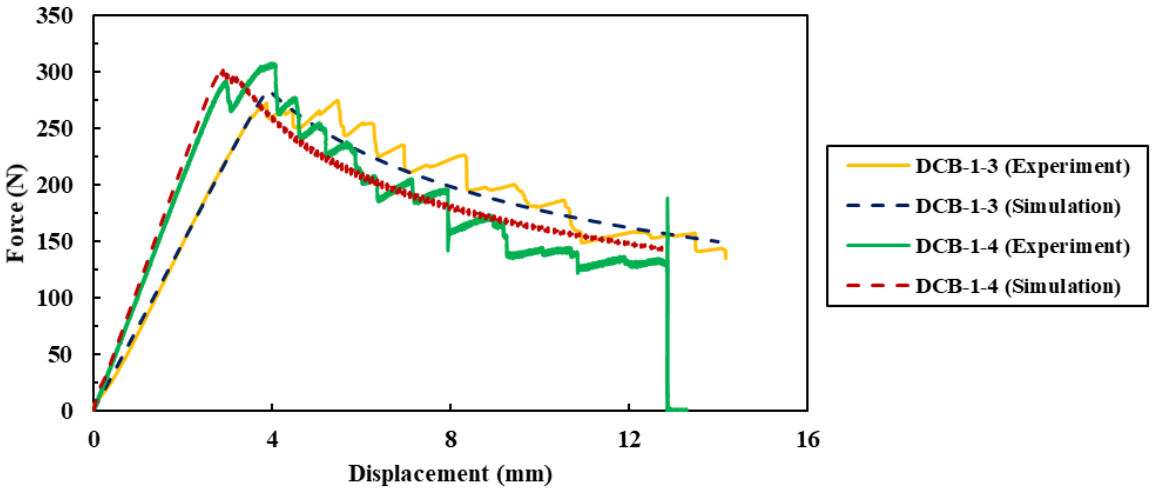

Figure 5.30. A comparison of the experimental and numerical force-displacement response for the upper and lower bound of the DCB-1 specimens. Cohesive properties for simulations from Table 5.7 with viscosity coefficient set to 0.

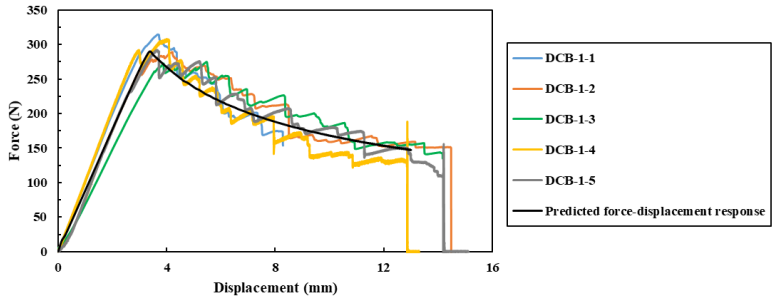

(a)

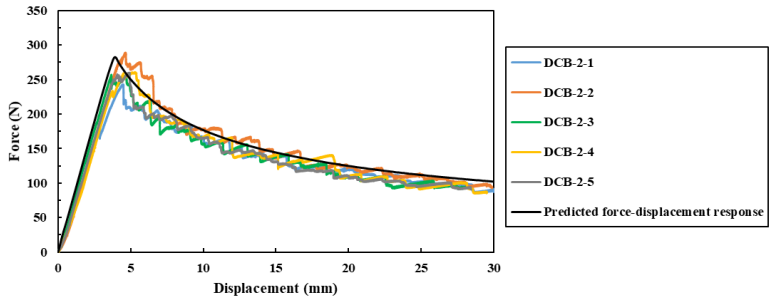

(b)

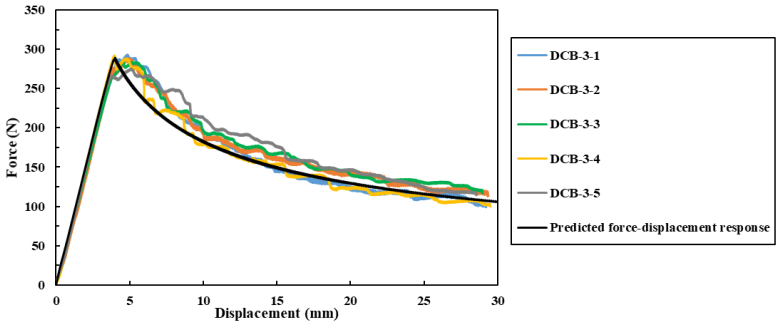

(c)

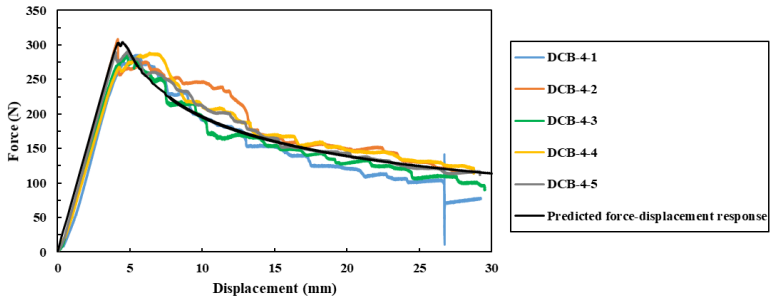

(d)

Figure 5.31. A comparison of the experimental and predicted numerical force-displacement response for different configurations of the DCB specimens: (a) DCB-1, (b) DCB-2, (c) DCB-3 and (d) DCB-4. Cohesive properties for simulations from Table 5.7 with viscosity coefficient set to 0.

Chapter 6: Discussion

6.1 Performance of Adhesively Bonded NCF-CFRP Single Lap Joint

The performance of the SLJ specimens comprising [0_7] NCF-CFRP adherends treated with different surface treatments demonstrated that there was no statistically significant difference in the measured joint strength. A similar failure mode consisting of damage in the adherend was observed for all corresponding SLJ specimens, while there was no evidence of adhesive and cohesive failure. Therefore, it can be concluded that the NCF-CFRP joint performance under a mixed-mode condition imparted by the single lap shear specimens was less sensitive to the adhesive and the adhesion between the adherend and adhesive, and instead dictated by the properties of the adherend. A light-fibre-tear failure mode was observed on the fracture surfaces of the SLJ specimens and was caused by combined peeling and shear stresses acting through the thickness of adherend [136, 137]. The predicted local stress distributions across the width of the adherend plies of the SP specimen at the end of the overlap region revealed that out-of-plane transverse normal stresses (i.e. peel stress) exceeded the ply transverse strength (see Figure 5.10a). Thus, the thin resin-rich region at the surface of the adherend bonded to the adhesive was not able to resist the combined out-of-plane stresses and ultimately controlled the SLJ strength.

It is worthwhile to mention that the lowest variability in joint strength was observed for the SLJ specimens treated with sandpaper. Measurements of the treated CFRP adherends revealed that the adherends treated with sandpaper exhibited the lowest variability in surface roughness with an average value 0.6 μm. From a practical point of view, modifying the surface roughness of the HP-RTM mould used to fabricate the CFRP parts can be used to control surface quality and improve the CFRP joint performance. On the other hand, the adherends treated by grit

blasting exhibited higher surface roughness compared to the sandpaper treated adherends, which typically leads to improved joint performance [90]. However, this was not found to be the case in this study. Instead, the average SLJ strength was slightly lower for the specimens with grit blasted adherends. Low joint strength for SLJ specimens treated with grit blasting is attributed to local damage in the polymer matrix of the CFRP adherend caused by the grit blasting procedure, which promoted the observed light-fiber-tear failure. The measured variability in the surface roughness for the grit blast treated adherends is due to the inconsistency of the local damage on the adherend surface, which contributed to the wide variability in SLJ strength.

Furthermore, the single lap joint strength increased by increasing the effective flexural longitudinal modulus of the CFRP adherend (Figure 6.1), which was dependent on the chosen stacking sequences. SLJ specimens comprising adherends with a high bending stiffness exhibited lower bending curvature, leading to less severe peel and out-of-plane shear stresses when compare to SLJ specimens consisting of adherends with lower bending stiffness. A similar trend was reported in the studies presented by Hart-Smith [100] and Kupski et al. [102]. Increasing in peel stress is observed from the local ply-level stress profiles for the SP, INT0 and INT45 SLJ specimens (Figures 5.10, 5.11 and 5.13), and by considering the corresponding variation in the onset of damage within the surface ply of the adherends (see Figures 5.7 and 5.8). For the INT90 specimens comprising adherends with the lowest flexural modulus, the finite element analysis revealed lower magnitude stresses compared to the other specimen configurations (see Figure 5.15), which is attributed to a more graduate evolution of local damage in the adherend that initiated in the surface 90° ply. Therefore, the adherend flexural

modulus and the onset of damage, which may be influenced by the orientation of the surface ply, collectively influence the SLJ strength.

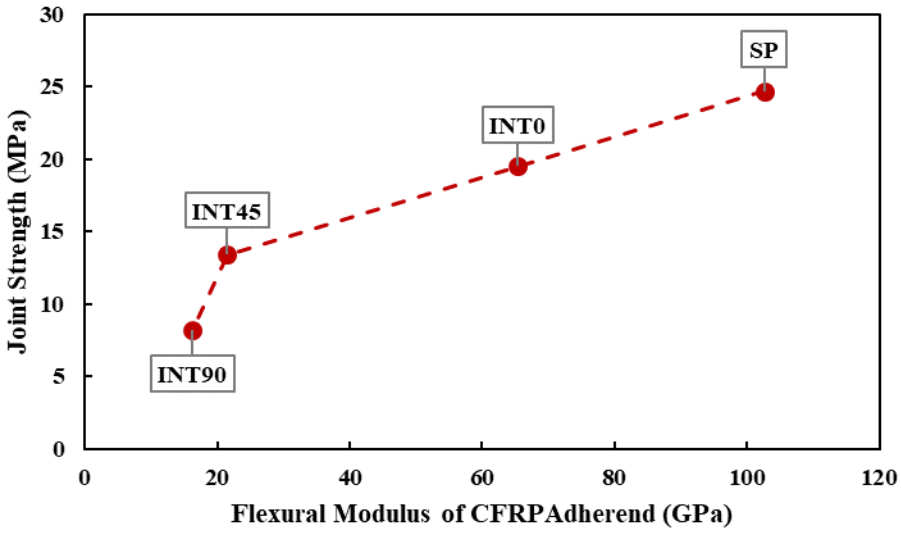

Figure 6.1. Effect of the flexural modulus of the CFRP adherend on SLJ strength.

In the present study, the spew fillets were removed from the edges of the overlap area of the SLJ specimens using sandpaper, which was also assumed in the conducted FEA to predict ply-level stresses. Lang and Mallick [98] reported that the presence of the spew fillets in adhesively bonded joints reduces the local stress concentrations and leads to an increase in the joint strength of adhesively bonded single lap joints. Hence, it could be concluded that a conservative measure of the joint strength was reported for the CFRP SLJ specimens assessed in this study.

6.2 Mode I Fracture Characterization of Adhesively Bonded NCF-CFRP Joint

Observations of fracture surfaces of the DCB specimens indicated that cohesive failure was the dominant failure mode. However, the crack path for the DCB specimens comprising a CFRP adherend with 53% fibre volume fraction (DCB-2) was more complex when compared to that of the CFRP adherend with 45% fibre volume fraction (DCB-1). Thin epoxy layers were removed from the adherend at the location of the stitching sites and the transverse glass fibres in both DCB configurations, resulting in localized bridging between the adherends. As observed on the fracture surface, localized bridging occurred in more locations for the DCB specimens comprising a CFRP adherend with 53% fibre volume fraction. It can be concluded that cracks were forced to propagate in a complex manner leading to an increased critical SERR value (Figure 6.2). It should be noted that length of the DCB-1 specimens was 120 mm, while it was 140 mm for the DCB-2 specimens.

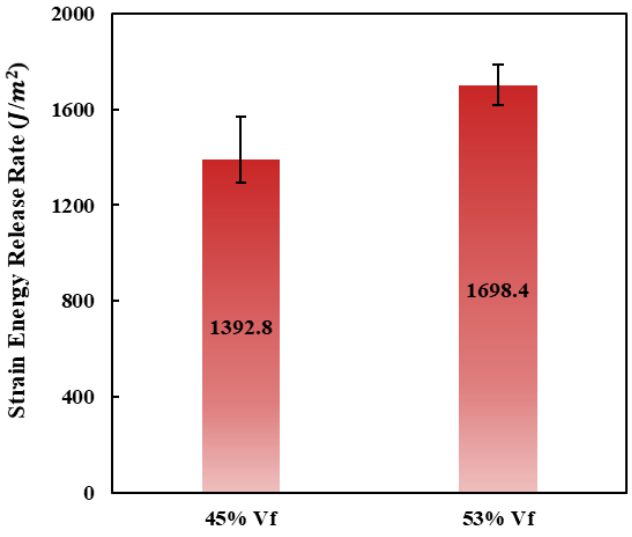

Figure 6.2. Effect of adherend fibre volume fraction on Mode I critical SERR (G_{Ic}).

The comparison between the fracture surfaces of SP SLJ specimens and DCB-1 specimens, both comprising adherends with $[0_7]$ stacking sequence and 45% fibre volume fraction, indicated that the joint configuration influenced the fracture surface morphology. Cohesive failure was the dominant failure mode under pure Mode I loading (Figure 6.3a), while light-fibre-tear failure, involving removal of a thin epoxy layer from the surface of the adherend, was the dominant failure mode under Mixed Mode I & II loading (Figure 6.3b). For the SLJ specimens, the adherends were subjected to high peel stress combined with out-of-plane shear stress at the end of the overlap area, which led to light-fibre-tear in the adherend. For DCB specimens, CFRP adherends were able to resist the peeling force since the peel stress was lower when compared to that for the SLJ specimens. However, owing to the stress concentration at the location of the stitching sites and the transverse glass fibres, the peel stress exceeded the ply transverse strength at these critical locations causing localized light-fibre-tear failure.

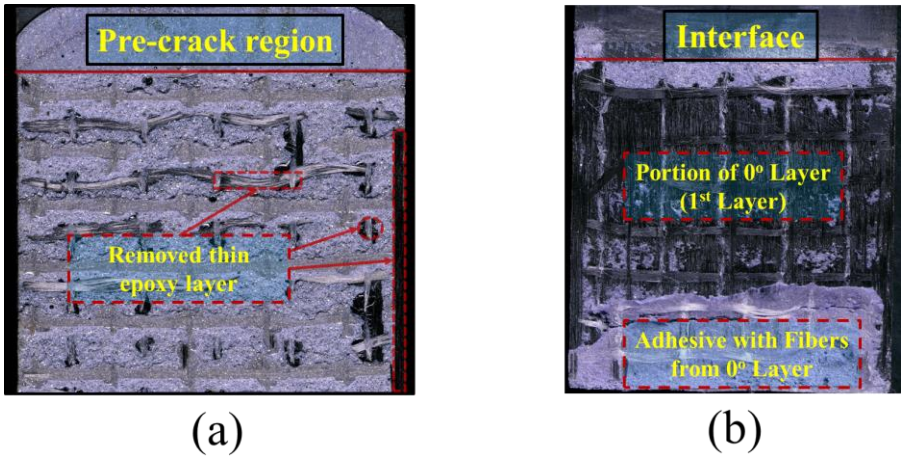

Figure 6.3. The fracture surfaces of the CFRP adherend with a $[0_7]$ stacking sequence with 45% fibre volume fraction under different loading conditions including (a) Mode I (DCB specimen) and (b) Mixed Mode I & II (SLJ specimen).

The DCB test results also revealed that the critical SERR increased with increasing adhesive bond-line thickness (Figure 6.4). The highest critical SERR was achieved for the DCB specimens with 0.65 mm bond-line thickness, while the lowest variability was achieved for the DCB specimens with 0.4 mm bond-line thickness. Increasing in critical SERR may be attributed to the ability of the adhesive to deform plastically when the bond line thickness increases, where a plastic zone forms ahead of the crack tip creating a damaged zone within the adhesive layer [138]. Increasing the adhesive bond-line thickness leads to a decrease in the degree of constraining effect from the two adherends and an increase in the plastic zone volume [27, 139, 140]. Kinloch and Shaw [139] reported that the critical SERR is dependent on the size of the plastic zone ahead of the crack tip.

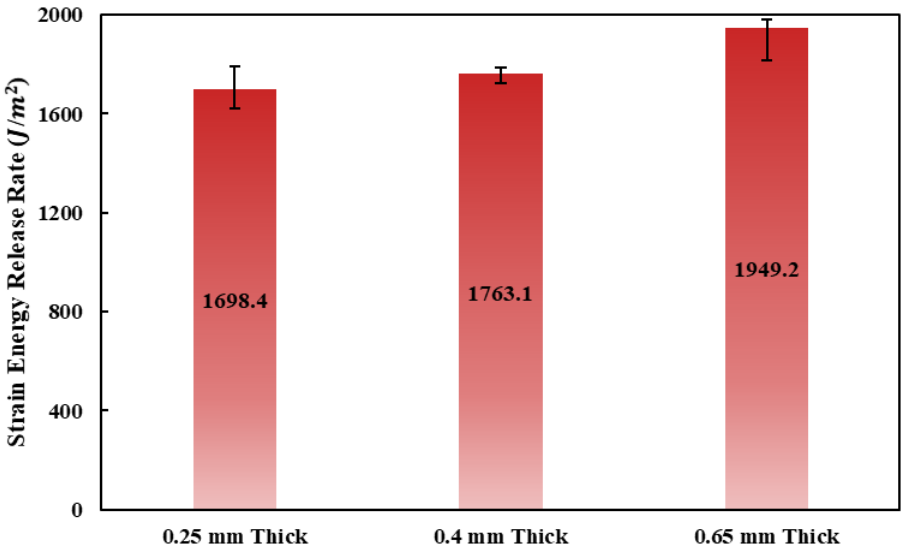

Figure 6.4. Influence of adhesive bond-line thickness on Mode I critical SERR (G_{Ic}).

The experimental results for the DCB specimens with different loading rates revealed that the critical SERR increased with increasing loading rate (Figure 6.5). Observation of the

fracture surfaces revealed that localized bridging was more widespread as the loading rate increased. This may be attributed to the increasingly brittle fracture behaviour of the NCF-CFRP adherend with increasing loading rate that facilitated the removal of a thin epoxy layer at the critical locations (i.e. the location of the stitching sites and the transverse glass fibres). Consequently, cracks in the adhesive layer are forced to propagate in a more complex manner, which explains the reason for an increase in the critical SERR value.

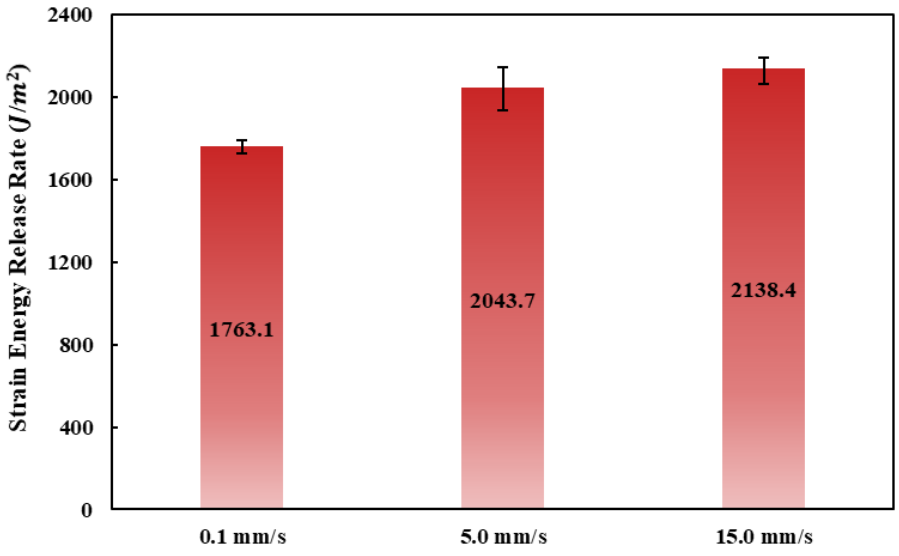

Figure 6.5. Influence of loading rate on Mode I critical SERR (G_{Ic}).

Furthermore, the parametric study performed to calibrate the Mode I cohesive properties revealed that the predicted force-displacement response of the DCB specimen was not significantly influenced by the initial stiffness and peak traction values considered for the bilinear traction-separation law. A similar issue was reported in previous studies [111, 141, 142]. For instance, Sun et al. [142] reported that the predicted force-displacement response for

an adhesively bonded joint was not sensitive to peak traction. As a result, an additional test was designed with higher sensitivity to peak traction for accurate identification purposes.

Finally, unstable crack propagation was observed in the adhesive of the DCB test specimens comprising CFRP adherends with 45% fibre volume fraction, which was evident in the rapid force drops in force-displacement response beyond the peak force (e.g. see Figure 5.17a). However, the numerical model developed to simulate the DCB tests predicted a smooth decreasing force in the post-peak region (see Figure 5.30). It can be concluded that the presented numerical model can capture the macroscopic response of the DCB specimen (e.g. the influence of pre-crack length or adhesive bond-line thickness on the predicted force-displacement response), whereas it is incapable of predicting the local mechanism of crack propagation (i.e. unstable crack propagation).

Chapter 7: Conclusions and Recommendations

7.1 Summary

The overall goal of this project was to assess the performance and Mode I fracture behaviour of adhesively bonded non-crimp fabric (NCF) carbon fibre-reinforced plastic (CFRP) joints. Adhesively bonded NCF-CFRP single lap joint (SLJ) specimens were used to assess the influence of the composite adherend surface treatment and stacking sequence on the joint strength and corresponding failure mechanisms. In addition, a three-dimensional finite element analysis was used to quantify the local stress components driving the observed failure mechanisms within the plies of the NCF-CFRP adherends. Double cantilever beam (DCB) tests were conducted to characterize the Mode I fracture behaviour of adhesively bonded NCF-CFRPs. The influence of adherend fibre volume fraction, adhesive bond-line thickness, and applied loading rate on Mode I fracture was investigated. A two-dimensional finite element analysis was employed to calibrate the Mode I bilinear traction-separation response of the adhesively bonded joint by comparing the predicted and experimentally measured force-displacement response. The following conclusions were drawn from this research project.

- For the NCF-CFRP adherend, the surface treatments considered did not notably influence the SLJ strength, owing to the fact that the CFRP adherend controlled failure of the joint. Nevertheless, the SLJ specimens with sandpaper treated adherends exhibited the lowest variability in strength when compared to specimens with adherends treated by other methods.

- The SLJ joint strength increased as the flexural modulus of the NCF-CFRP adherend increased, which is a direct result of the influence of stacking sequence on the onset

of local damage mechanisms. NCF-CFRP laminates with off-axis plies at the surface (and lower flexural modulus) exhibited damage onset (e.g., matrix cracking) at lower applied loads due to the low transverse strength of the unidirectional plies.

- The Mode I critical strain energy release rate (SERR) increased with increasing adherend fibre volume fraction, adhesive bond-line thickness and applied loading rate.
- Fibre-tear and light-fibre-tear failure were the dominant failure modes for SLJ specimens (mixed Mode I and II), while cohesive failure mode was the dominant failure mode for DCB specimens (Mode I). Furthermore, localized bridging was observed at the fracture surface of the DCB specimens, and the severity of bridging increased with increasing applied loading rate.
- To calibrate the cohesive zone model (CZM) parameters, DCB tests were less sensitive to the peak traction and initial stiffness, therefore, an additional test is required to calibrate accurately the CZM parameters.

7.2 Recommendations

Some recommendations for future studies are presented due to the complex nature of adhesive bonding for NCF-CFRP materials.

- In order to provide a better understanding of the mechanism of the surface treatments on the surface of CFRP adherends, additional experimental tests such as

contact angle test or employing spectroscopic methods including X-ray photoelectron spectroscopy could be beneficial.

- As a means to measure experimentally Mode I cohesive properties which cannot be determined by DCB tests, an additional experimental test such as the butt joint test is recommended to consider for future studies.
- The cohesive properties may not be material properties and can depend on several aspects, including the adherend surface treatment. As a result, it is recommended to assess the influence of adherend surface treatment on the Mode I fracture behaviour of adhesively bonded joints.
- With the intention of fully characterization of fracture behaviour, it is recommended to consider Mode II fracture assessment for the future experimental test.
- The test methodology of the present project focused on the low loading rates. However, composite and adhesives materials are polymeric materials which are sensitive to loading rate. As a result, it is suggested to assess the performance and fracture behaviour of adhesively bonded NCF-CFRP joints under high loading rates which could be beneficial for practical applications for vehicle structures.
- Joint durability is an important parameter in adhesively bonded joints. As a result, it is suggested to consider an experimental study under fatigue loading conditions to provide more insight into joint durability in adhesively bonded joints.

Bibliography

[1] Obama Administration Finalizes Historic 54.5 MPG Fuel Efficiency Standards | whitehouse.gov, https://obamawhitehouse.archives.gov/the-press-office/2012/08/28/obama-administration-finalizes-historic-545-MPG-fuel-efficiency-standard (accessed 8 March 2021).

[2] *The Road Ahead*. 2015.

[3] Canada to copy Obama's fuel efficiency rules - The Globe and Mail, https://www.theglobeandmail.com/report-on-business/industry-news/energy-and-resources/canada-to-copy-obamas-fuel-efficiency-rules/article4508608/ (accessed 8 March 2021).

[4] BMW 7 Series Plant: Dingolfing, Germany | CompositesWorld, https://www.compositesworld.com/articles/bmw-7-series-plant-dingolfing-germany (accessed 8 March 2021).

[5] Das S, Graziano D, Upadhyayula VKK, et al. Vehicle lightweighting energy use impacts in U.S. light-duty vehicle fleet. *Sustain Mater Technol* 2016; 8: 5–13.

[6] Mayyas AT, Qattawi A, Mayyas AR, et al. Life cycle assessment-based selection for a sustainable lightweight body-in-white design. *Energy* 2012; 39: 412–425.

[7] Joost WJ. Reducing vehicle weight and improving U.S. energy efficiency using integrated computational materials engineering. *JOM* 2012; 64: 1032–1038.

[8] Zhu G, Sun G, Yu H, et al. Energy absorption of metal, composite and metal/composite hybrid structures under oblique crushing loading. *Int J Mech Sci* 2018; 135: 458–483.

[9] Cherniaev A, Butcher C, Montesano J. Predicting the axial crush response of CFRP tubes using three damage-based constitutive models. *Thin-Walled Struct* 2018; 129: 349–364.

[10] Jacob GC, Fellers JF, Simunovic S, et al. Energy Absorption in Polymer Composites for Automotive Crashworthiness. *J Compos Mater* 2002; 36: 813–850.

[11] Singh H (Edag I. Mass Reduction for Light-Duty Vehicles for Model Years 2017-2025 Final Report. *Rep No DOT HS 811 666* 2012; 582.

[12] CFRP materials - Audi Technology Portal, https://www.audi-technology-portal.de/en/body/materials/cfrp-materials (accessed 8 March 2021).

[13] Lamborghini Murciélago LP 670 SuperVeloce - Technical Specifications, https://www.lamborghini.com/en-en/brand/masterpieces/murcielago-lp-670-superveloce (accessed 8 March 2021).

[14] Trejo Sandoval EA. Characterizing the deformation response of a unidirectional non-crimp fabric for the development of computational draping simulation models. *MASc Thesis, University of Waterloo*, 2020.

[15] Zeng Y. Mechanical characterization and computational modeling of snap-cure epoxy. *MASc Thesis, University of Waterloo,* 2020.

[16] Rosenberg P, Thoma B, Paper FH-AC, et al. Characterization of epoxy and polyurethane resin systems for manufacturing of high-performance composites in high-pressure RTM process. *academia.edu*.

[17] Panchagnula KK, Palaniyandi K. Drilling on fiber reinforced polymer/nanopolymer composite laminates: A review. *Journal of Materials Research and Technology* 2018; 7: 180–189.

[18] Banea MD, da Silva LFM. Adhesively bonded joints in composite materials: An overview. *Proc Inst Mech Eng Part L J Mater Des Appl* 2009; 223: 1–18.

[19] Ghaffari B, Lazarz K, Ondrus D, et al. A matrix array technique for evaluation of adhesively bonded joints.

[20] Budhe S, Banea MD, de Barros S, et al. An updated review of adhesively bonded joints in composite materials. *Int J Adhes Adhes* 2017; 72: 30–42.

[21] Kanerva M, Saarela O. The peel ply surface treatment for adhesive bonding of composites: A review. *International Journal of Adhesion and Adhesives* 2013; 43: 60–69.

[22] Fischer F, Kreling S, Gäbler F, et al. Using excimer lasers to clean CFRP prior to adhesive bonding. *Reinf Plast* 2013; 57: 43–46.

[23] Njuhovic E, Witt A, Kempf M, et al. Influence of the composite surface structure on the peel strength of metallized carbon fibre-reinforced epoxy. *Surf Coatings Technol* 2013; 232: 319–325.

[24] Park SM, Roy R, Kweon JH, et al. Strength and failure modes of surface treated CFRP secondary bonded single-lap joints in static and fatigue tensile loading regimes. *Compos Part A Appl Sci Manuf* 2020; 134: 105897.

[25] da Silva LFM, Campilho RDSG. Advances in numerical modelling of adhesive joints. In: *SpringerBriefs in Applied Sciences and Technology*. Springer Verlag, 2012, pp. 1–93.

[26] Trimiño LF, Cronin DS. Evaluation of Numerical Methods to Model Structural Adhesive Response and Failure in Tension and Shear Loading. *J Dyn Behav Mater* 2016; 2: 122–137.

[27] Banea MD, da Silva LFM, Campilho RDSG. The Effect of Adhesive Thickness on the Mechanical Behavior of a Structural Polyurethane Adhesive. *J Adhes* 2015; 91: 331–346.

[28] Blackman BRK, Kinloch AJ, Rodriguez-Sanchez FS, et al. The fracture behaviour of adhesively-bonded composite joints: Effects of rate of test and mode of loading. *Int J Solids Struct* 2012; 49: 1434–1452.

[29] Georgiou I, Ivankovic A, Kinloch AJ, et al. Rate dependent fracture behaviour of adhesively bonded joints. In: *European Structural Integrity Society*. Elsevier Ltd, 2003, pp. 317–328.

[30] Reinhart TJ. Overview of Composite Materials. In: *Handbook of Composites*. Springer US, 1998, pp. 21–33.

[31] Mallick P. *Fiber-reinforced composites: materials, manufacturing, and design*. 2007.

[32] Chawla K. *Composite materials: science and engineering*. 2012.

[33] Datoo MH. *Mechanics of Fibrous Composites*. 1991. Epub ahead of print 1991. DOI: 10.1007/978-94-011-3670-9.

[34] Inagaki M. *New carbons-control of structure and functions*. 2000.

[35] Lomov S V., Chi TT, Verpoest I. Mechanical properties of non-crimp fabric (NCF) based composites: Stiffness and strength. In: *Non-Crimp Fabric Composites: Manufacturing, Properties and Applications*. 2011, pp. 263–288.

[36] Sandoval ET. Characterizing the deformation response of a unidirectional non-crimp fabric for the development of computational draping simulation models.

[37] Lee BL, Song JW, Ward JE. Failure of Spectra®* Polyethylene Fiber-Reinforced Composites under Ballistic Impact Loading. *J Compos Mater* 1994; 28: 1202–1226.

[38] Vanclooster K, Lomov S V., Verpoest I. Experimental validation of forming simulations of fabric reinforced polymers using an unsymmetrical mould configuration. *Compos Part A Appl Sci Manuf* 2009; 40: 530–539.

[39] Margossian A, Ding M, Avila Gray L, et al. Flexural characterisation of unidirectional thermoplastic tapes using a dynamic mechanical analysis system. In: *16th European Conference on Composite Materials, ECCM 2014*. 2014, pp. 22–26.

[40] Šimáček P, Advani SG. Desirable features in mold filling simulations for liquid composite molding processes. *Polym Compos* 2004; 25: 355–367.

[41] Arbter R, Beraud JM, Binetruy C, et al. Experimental determination of the permeability of textiles: A benchmark exercise. *Compos Part A Appl Sci Manuf* 2011; 42: 1157–1168.

[42] Cherniaev A, Zeng Y, Cronin D, et al. Quasi-static and dynamic characterization of unidirectional non-crimp carbon fiber fabric composites processed by HP-RTM. *Polym Test* 2019; 76: 365–375.

[43] Laurenzi S, Marchetti M. Advanced Composite Materials by Resin Transfer Molding for Aerospace Applications. In: *Composites and Their Properties*. InTech, 2012. Epub ahead of print 22 August 2012. DOI: 10.5772/48172.

[44] Chaudhari R, Karcher M, Elsner P, et al. Characterization of high pressure RTM processes for manufacturing of high performance composites. In: *ECCM 2012 - Composites at Venice, Proceedings of the 15th European Conference on Composite Materials*. 2012.

[45] Chaudhari R, Rosenberg P, Karcher M, et al. High pressure RTM process variants for manufacturing of carbon fiber reinforced composites.

[46] Chamis CC. *Structural design and analysis, Part II*. 1974.

[47] Hyer MW. *Stress Analysis of Fibre-Reinforced Composite Materials*. 2009.

[48] Kaw A. *Mechanics of composite materials*. 2005.

[49] Harris B. Analysis and performance of fibre composites. *Compos Sci Technol* 1991; 41: 433–434.

[50] Altenbach H, Altenbach J, Kissing W, et al. Failure Mechanisms and Criteria. In: *Mechanics of Composite Structural Elements*. Springer Singapore, 2018, pp. 201–224.

[51] Puck A, Schürmann H. Failure analysis of FRP laminates by means of physically based phenomenological models. *Compos Sci Technol* 1998; 58: 1045–1067.

[52] Puck A, Kopp J, Knops M. Guidelines for the determination of the parameters in Puck's action

plane strength criterion. *Compos Sci Technol* 2002; 62: 371–378.

[53] Ebnesajjad S. *Handbook of Adhesives and Surface Preparation*. 2011. Epub ahead of print 2011. DOI: 10.1016/C2010-0-65918-9.

[54] Mittal K. *Adhesive Joints: Formation, Characteristics and Testintg*. 2002.

[55] da Silva LFM, Öchsner A, Adams RD. *Handbook of Adhesion Technology: Second Edition*. 2018. Epub ahead of print 2018. DOI: 10.1007/978-3-319-55411-2.

[56] Helfand D. Recent developments in epoxy resins and curing agents. *J Coatings Technol* 1996; 68: 73–79.

[57] Prolongo SG, Del Rosario G, Ureña A. Comparative study on the adhesive properties of different epoxy resins. *Int J Adhes Adhes* 2006; 26: 125–132.

[58] Brockmann H, Haufe M, Schulenburg JO. Mechanism of the curing reaction of model epoxy compounds with monuron. *Int J Adhes Adhes* 2000; 20: 333–340.

[59] Stewart I, Chambers A, Gordon T. The cohesive mechanical properties of a toughened epoxy adhesive as a function of cure level. *Int J Adhes Adhes* 2007; 27: 277–287.

[60] Rudawska A. Epoxy adhesives. In: *Handbook of Adhesive Technology, Third Edition*. CRC Press, 2017, pp. 415–442.

[61] Petrie EM. *Epoxy Adhesive Formulations*. 2006.

[62] Schiel M, Kreling S, Unger C, et al. Behavior of adhesively bonded coated steel for automotive applications under impact loads. *Int J Adhes Adhes* 2015; 56: 32–40.

[63] Pate KD. Applications of adhesives in aerospace. In: *Adhesion Science and Engineering*. 2002, pp. 1129–1192.

[64] Critchlow G. General Introduction to Surface Treatments. In: *Handbook of Adhesion Technology*. Springer Berlin Heidelberg, 2011, pp. 119–146.

[65] Baldan A. Adhesively-bonded joints and repairs in metallic alloys, polymers and composite materials: Adhesives, adhesion theories and surface pretreatment. *Journal of Materials Science* 2004; 39: 1–49.

[66] Davis GD. Surface Treatments of Selected Materials. In: *Handbook of Adhesion Technology*. Springer Berlin Heidelberg, 2011, pp. 147–177.

[67] Nandwani Y. Characterization of Structural Adhesives Using Lap Shear and Pin and Collar Tests. *undefined*.

[68] Banea MD, da Silva LFM. Adhesively bonded joints in composite materials: An overview. *Proc Inst Mech Eng Part L J Mater Des Appl* 2009; 223: 1–18.

[69] Kanerva M, Sarlin E, Hoikkanen M, et al. Interface modification of glass fibre-polyester composite-composite joints using peel plies. *Int J Adhes Adhes* 2015; 59: 40–52.

[70] Buchmann C, Langer S, Filsinger J, et al. Analysis of the removal of peel ply from CFRP surfaces. *Compos Part B Eng* 2016; 89: 352–361.

[71] Budhe SR. EFFECT OF PRE-BOND MOISTURE ON THE STATIC AND FATIGUE BEHAVIOUR OF BONDED JOINTS BETWEEN CFRP LAMINATES FOR STRUCTURES REPAIRS EFFECT OF PRE-BOND MOISTURE ON THE STATIC AND FATIGUE BEHAVIOUR OF BONDED STRUCTURAL REPAIRS Sandip Rudha Budhe.

[72] Fernholz KD. Bonding of polymer matrix composites. In: *Advances in Structural Adhesive Bonding*. Elsevier Inc., 2010, pp. 265–291.

[73] Marimuthu S, Sezer HK, Kamara AM. Applications of Laser Cleaning Process in High Value Manufacturing Industries. In: *Developments in Surface Contamination and Cleaning: Applications of Cleaning Techniques*. Elsevier, 2019, pp. 251–288.

[74] Satas, D, Tracton, AA, Rafanelli AJ. Coatings Technology Handbook, Second Edition. *J Electron Packag* 2002; 124: 67–68.

[75] Ganesan A, Yamada M, Fukumoto M. The effect of CFRP surface treatment on the splat morphology and coating adhesion strength. In: *Journal of Thermal Spray Technology*. Springer, 2014, pp. 236–244.

[76] Martínez-Landeros VH, Vargas-Islas SY, Cruz-González CE, et al. Studies on the influence of surface treatment type, in the effectiveness of structural adhesive bonding, for carbon fiber reinforced composites. *J Manuf Process* 2019; 39: 160–166.

[77] Li S, Sun T, Liu C, et al. A study of laser surface treatment in bonded repair of composite aircraft structures. *R Soc Open Sci*; 5. Epub ahead of print 21 March 2018. DOI: 10.1098/rsos.171272.

[78] Belcher MA, Krieg KL, Van Voast PJ, et al. Nonchemical surface treatments using atmospheric plasma systems for structural adhesive bonding. In: *International SAMPE Technical*

Conference. 2013, pp. 567–571.

[79] Wolf RA. *Atmospheric Pressure Plasma for Surface Modification*. 2012. Epub ahead of print 2012. DOI: 10.1002/9781118547519.

[80] Zaldivar RJ, Nokes J, Steckel GL, et al. The effect of atmospheric plasma treatment on the chemistry, morphology and resultant bonding behavior of a pan-based carbon fiber-reinforced epoxy composite. *J Compos Mater* 2010; 44: 137–156.

[81] Pizzorni M, Lertora E, Mandolfino C. Low pressure plasma treatment of CFRP substrates for adhesive bonding: an investigation of joint durability under severe temperature-moisture conditioning. *Int J Adhes Adhes* 2020; 99: 102592.

[82] Fischer F, Kreling S, Jäschke P, et al. Laser surface pre-treatment of CFRP for adhesive bonding in consideration of the absorption behaviour. In: *Journal of Adhesion*. Taylor & Francis Group, 2012, pp. 350–363.

[83] Sorrentino L, Marfia S, Parodo G, et al. Laser treatment surface: An innovative method to increase the adhesive bonding of ENF joints in CFRP. *Compos Struct* 2020; 233: 111638.

[84] Rauh B, Kreling S, Kolb M, et al. UV-laser cleaning and surface characterization of an aerospace carbon fibre reinforced polymer. *Int J Adhes Adhes* 2018; 82: 50–59.

[85] Mittal KL, Bahners T. *Laser Surface Modification and Adhesion*. Hoboken, NJ, USA: John Wiley & Sons, Inc., 2014. Epub ahead of print 10 October 2014. DOI: 10.1002/9781118831670.

[86] Shang X, Marques EAS, Machado JJM, et al. Review on techniques to improve the strength of adhesive joints with composite adherends. *Composites Part B: Engineering* 2019; 177: 107363.

[87] Boerio FJ, Roby B, Dillingham RG, et al. Effect of grit-blasting on the surface energy of graphite/epoxy composites. *J Adhes* 2006; 82: 19–37.

[88] Chamochin R, De Santayana MC, Abenojar J, et al. The effect of surface treatment on the behavior of toughened acrylic adhesive/GRP(epoxy) composite joints. In: *Journal of Adhesion Science and Technology*. Taylor & Francis Group, 2010, pp. 1903–1916.

[89] Zaldivar RJ, Kim HI, Steckel GL, et al. The effect of abrasion surface treatment on the bonding behavior of various carbon fiber-reinforced composites. *J Adhes Sci Technol* 2012; 26: 1573–1590.

[90] Yang G, Yang T, Yuan W, et al. The influence of surface treatment on the tensile properties of carbon fiber-reinforced epoxy composites-bonded joints. *Compos Part B Eng* 2019; 160: 446–456.

[91] Banea MD, Da Silva LFM. Adhesively bonded joints in composite materials: An overview. *Proceedings of the Institution of Mechanical Engineers, Part L: Journal of Materials: Design and Applications* 2009; 223: 1–18.

[92] Banea MD, Rosioara M, Carbas RJC, et al. Multi-material adhesive joints for automotive industry. *Compos Part B Eng* 2018; 151: 71–77.

[93] Jeevi G, Nayak SK, Abdul Kader M. Review on adhesive joints and their application in hybrid composite structures. *Journal of Adhesion Science and Technology* 2019; 33: 1497–1520.

[94] Neto JABP, Campilho RDSG, Da Silva LFM. Parametric study of adhesive joints with composites. In: *International Journal of Adhesion and Adhesives*. Elsevier, 2012, pp. 96–101.

[95] Singh A, del Rey Castillo E, Ingham J. FRP-to-FRP bond characterization and force-based bond length model. *Compos Struct* 2019; 210: 724–734.

[96] da Silva LFM, Rodrigues TNSS, Figueiredo MAV, et al. Effect of adhesive type and thickness on the lap shear strength. *J Adhes* 2006; 82: 1091–1115.

[97] Moya-Sanz EM, Ivañez I, Garcia-Castillo SK. Effect of the geometry in the strength of single-lap adhesive joints of composite laminates under uniaxial tensile load. *Int J Adhes Adhes* 2017; 72: 23–29.

[98] Lang TP, Mallick PK. Effect of spew geometry on stresses in single lap adhesive joints. *Int J Adhes Adhes* 1998; 18: 167–177.

[99] Belingardi G, Goglio L, Tarditi A. Investigating the effect of spew and chamfer size on the stresses in metal/plastics adhesive joints. *Int J Adhes Adhes* 2002; 22: 273–282.

[100] Hart-Smith L. *Adhesive-bonded single-lap joints*. 1973.

[101] Demiral M, Kadioglu F. Failure behaviour of the adhesive layer and angle ply composite adherends in single lap joints: A numerical study. *Int J Adhes Adhes* 2018; 87: 181–190.

[102] Kupski J, Teixeira de Freitas S, Zarouchas D, et al. Composite layup effect on the failure mechanism of single lap bonded joints. *Compos Struct* 2019; 217: 14–26.

[103] Purimpat S, Jérôme R, Shahram A. Effect of fiber angle orientation on a laminated composite single-lap adhesive joint. *Adv Compos Mater* 2013; 22: 139–149.

[104] Ozel A, Yazici B, Akpinar S, et al. A study on the strength of adhesively bonded joints with different adherends. *Compos Part B Eng* 2014; 62: 167–174.

[105] Meneghetti G, Quaresimin M, Ricotta M. Influence of the interface ply orientation on the fatigue behaviour of bonded joints in composite materials. *Int J Fatigue* 2010; 32: 82–93.

[106] Chaves FJP, Da Silva LFM, De Moura MFSF, et al. Fracture mechanics tests in adhesively bonded joints: A literature review. *Journal of Adhesion* 2014; 90: 955–992.

[107] Dillard DA. Fracture mechanics of adhesive bonds. In: *Adhesive Bonding: Science, Technology and Applications*. Elsevier Inc., 2005, pp. 189–208.

[108] Griffits AA. The phenomena of rupture and flow in solids. *Masinovedenie* 1995; 9–14.

[109] Kinloch AJ, Kinloch AJ. Fracture mechanics of adhesive joints. In: *Adhesion and Adhesives*. Springer Netherlands, 1987, pp. 264–338.

[110] Irwin GR, Kies JA. Critical energy rate analysis of fracture strength. *Spie Milestone Ser MS* 1997; 137: 136–141.

[111] Alfano M, Lubineau G, Furgiuele F, et al. On the enhancement of bond toughness for Al/epoxy T-peel joints with laser treated substrates. *Int J Fract* 2011; 171: 139–150.

[112] Valoroso N, Fedele R. Characterization of a cohesive-zone model describing damage and de-cohesion at bonded interfaces. Sensitivity analysis and mode-I parameter identification. *Int J Solids Struct* 2010; 47: 1666–1677.

[113] Marzi S, Hesebeck O, Brede M, et al. A rate-dependent cohesive zone model for adhesively bonded joints loaded in mode i. *J Adhes Sci Technol* 2009; 23: 881–898.

[114] Dastjerdi AK, Pagano M, Kaartinen MT, et al. Cohesive behavior of soft biological adhesives: Experiments and modeling. *Acta Biomater* 2012; 8: 3349–3359.

[115] Watson B, Liao CH, Worswick MJ, et al. Mode I traction-separation measured using rigid double cantilever beam applied to structural adhesive. *J Adhes* 2018; 96: 717–737.

[116] Moore D, Williams J, Pavan A. *Fracture mechanics testing methods for polymers, adhesives and composites*. 2001.

[117] Da Silva LFM, De Magalhães FACRG, Chaves FJP, et al. Mode II fracture toughness of a brittle and a ductile adhesive as a function of the adhesive thickness. *J Adhes* 2010; 86: 891–905.

[118] Banea MD, Da Silva LFM, Campilho RDSG. Mode II fracture toughness of adhesively bonded joints as a function of temperature: Experimental and numerical study. In: *Journal of Adhesion*. Taylor & Francis Group, 2012, pp. 534–551.

[119] Watson B, Worswick MJ, Cronin DS. Quantification of mixed mode loading and bond line thickness on adhesive joint strength using novel test specimen geometry. *Int J Adhes Adhes* 2020; 102: 102682.

[120] Marzi S, Biel A, Stigh U. On experimental methods to investigate the effect of layer thickness on the fracture behavior of adhesively bonded joints. *Int J Adhes Adhes* 2011; 31: 840–850.

[121] Lißner M, Alabort E, Cui H, et al. Experimental characterisation and numerical modelling of the influence of bondline thickness, loading rate, and deformation mode on the response of ductile adhesive interfaces. *J Mech Phys Solids* 2019; 130: 349–369.

[122] Ravindran S, Sockalingam S, Kodagali K, et al. Mode-I behavior of adhesively bonded composite joints at high loading rates. *Compos Sci Technol* 2020; 198: 108310.

[123] Sun F, Zhang R, Blackman BRK. Determination of the mode I crack tip opening rate and the rate dependent cohesive properties for structural adhesive joints using digital image correlation. *Int J Solids Struct* 2021; 217–218: 60–73.

[124] Adams R, Adams R, Comyn J, et al. Structural Adhesive Joints in Engineering. *Assem Autom* 2000; 20: 136–140.

[125] Pardoen T, Ferracin T, Landis CM, et al. Constraint effects in adhesive joint fracture. *J Mech Phys Solids* 2005; 53: 1951–1983.

[126] Xie D, Waas AM. Discrete cohesive zone model for mixed-mode fracture using finite element analysis. *Eng Fract Mech* 2006; 73: 1783–1796.

[127] Leffler K, Alfredsson KS, Stigh U. Shear behaviour of adhesive layers. *Int J Solids Struct* 2007; 44: 530–545.

[128] Campilho RDSG, de Moura MFSF, Domingues JJMS. Numerical prediction on the tensile residual strength of repaired CFRP under different geometric changes. *Int J Adhes Adhes* 2009; 29: 195–205.

[129] Li S, Thouless MD, Waas AM, et al. Use of a cohesive-zone model to analyze the fracture of a fiber-reinforced polymer-matrix composite. *Compos Sci Technol* 2005; 65: 537–549.

[130] HEXION. *Technical Data Sheet*. Duisburg, 2015.

[131] Suratkar A. "Private correspondence" *PhD, Western University,* , 2020.

[132] Watson B, Nandwani Y, Worswick MJ, et al. Metallic multi-material adhesive joint testing and modeling for vehicle lightweighting. *Int J Adhes Adhes* 2019; 95: 102421.

[133] Data Thechnical Report. *Impact Resistant Structural Adhesive 07333 / 57333*. 2015.

[134] Suratkar A, Fan Y, Montesano J WJ. Quasi-static mechanical characterization of non-crimp carbon fiber reinforced epoxy laminates manufactured using HP-RTM process. In: *SPE Automotive Composites Conference & Exhibition (ACCE)*. 2018.

[135] Li B, Li Y, Su J. A combined interface element to simulate interfacial fracture of laminated shell structures. *Compos Part B Eng* 2014; 58: 217–227.

[136] Bak KM, Kalaichelvan K, Arumugam V. A novel approach for classification of failure modes in single lap joints using acoustic emission data. *J Compos Mater* 2014; 48: 3003–3017.

[137] Thull D, Zimmer F, Hofmann T, et al. Investigation of fluorine-based release agents for structural adhesive bonding of carbon fibre reinforced plastics. *Appl Adhes Sci* 2019; 7: 2.

[138] Papini M, Fernlund G, Spelt JK. The effect of geometry on the fracture of adhesive joints. *Int J Adhes Adhes* 1994; 14: 5–13.

[139] Kinloch AJ, Shaw SJ. The Fracture Resistance of a Toughened Epoxy Adhesive. *J Adhes* 1981; 12: 59–77.

[140] Lopes Fernandes R, Teixeira de Freitas S, Budzik MK, et al. From thin to extra-thick adhesive layer thicknesses: Fracture of bonded joints under mode I loading conditions. *Eng Fract Mech* 2019; 218: 106607.

[141] Kafkalidis MS, Thouless MD, Yang QD, et al. Deformation and fracture of adhesive layers constrained by plastically-deforming adherends. *J Adhes Sci Technol* 2000; 14: 1593–1607.

[142] Sun C, Thouless MD, Waas AM, et al. Ductile-brittle transitions in the fracture of plastically-deforming, adhesively-bonded structures. Part I: Experimental studies. *Int J Solids Struct* 2008; 45: 3059–3073.

Appendix A

As mentioned in Section 3.3.3, a calibration parameter must be calculated for each DCB specimen to determine the corresponding strain energy release rate. The plot of the cube root of compliance as a function of crack length is required for calculating the calibration parameter for each DCB configuration (Figures A.1.1, A.1.2, A.1.3, A.1.4, A.1.5 and A.1.6).

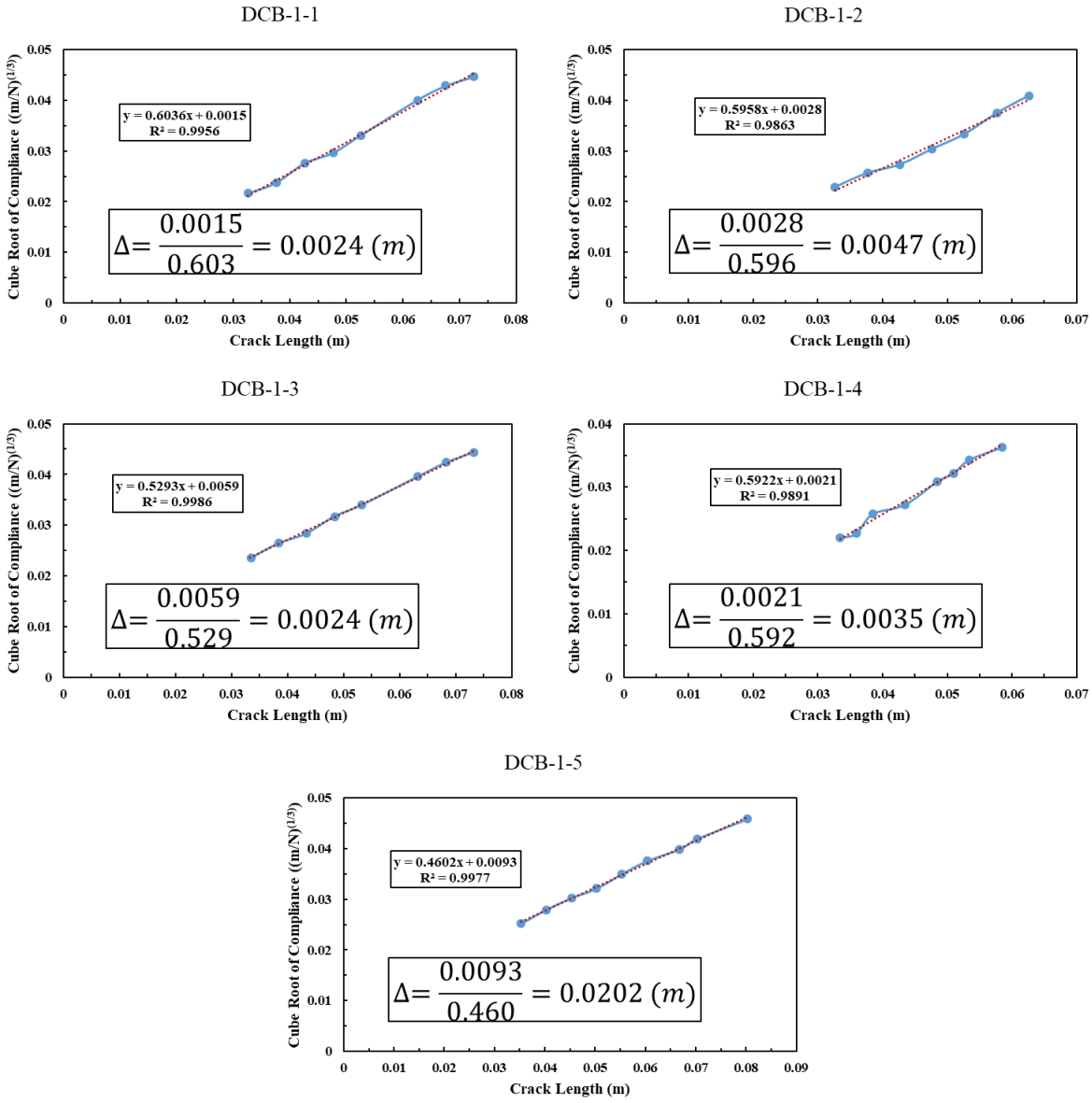

Figure A.1.1. The least-square plot of the cube root of the compliance versus the crack length for the DCB specimens comprising CFRP adherends with 45% fibre volume fraction with 0.25 mm adhesive bond-line thickness with a loading rate of 0.1 mm/s.

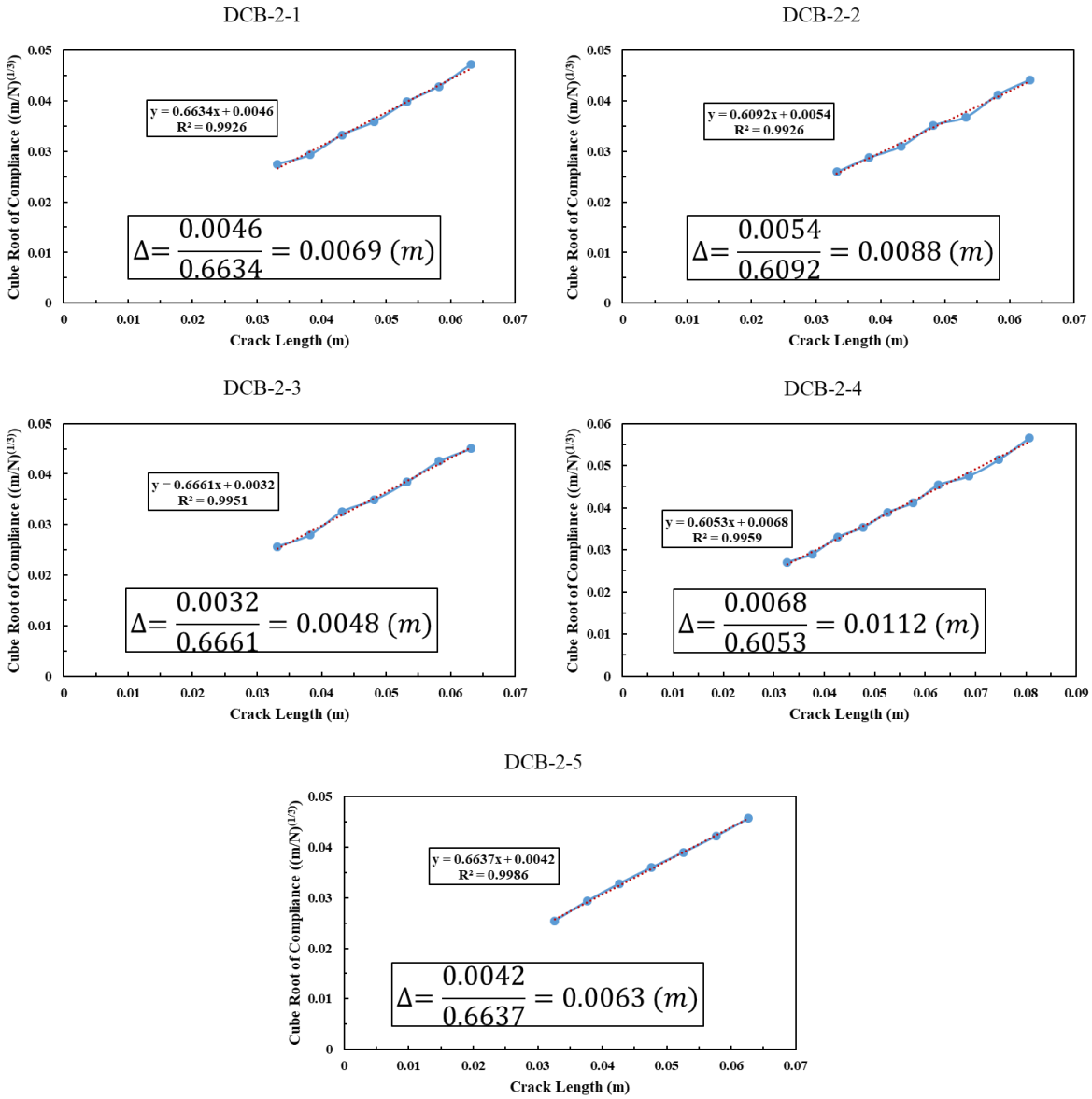

Figure A.1.2. The least-square plot of the cube root of the compliance versus the crack length for the DCB specimens comprising CFRP adherends with 53% fibre volume fraction with 0.25 mm adhesive bond-line thickness with a loading rate of 0.1 mm/s.

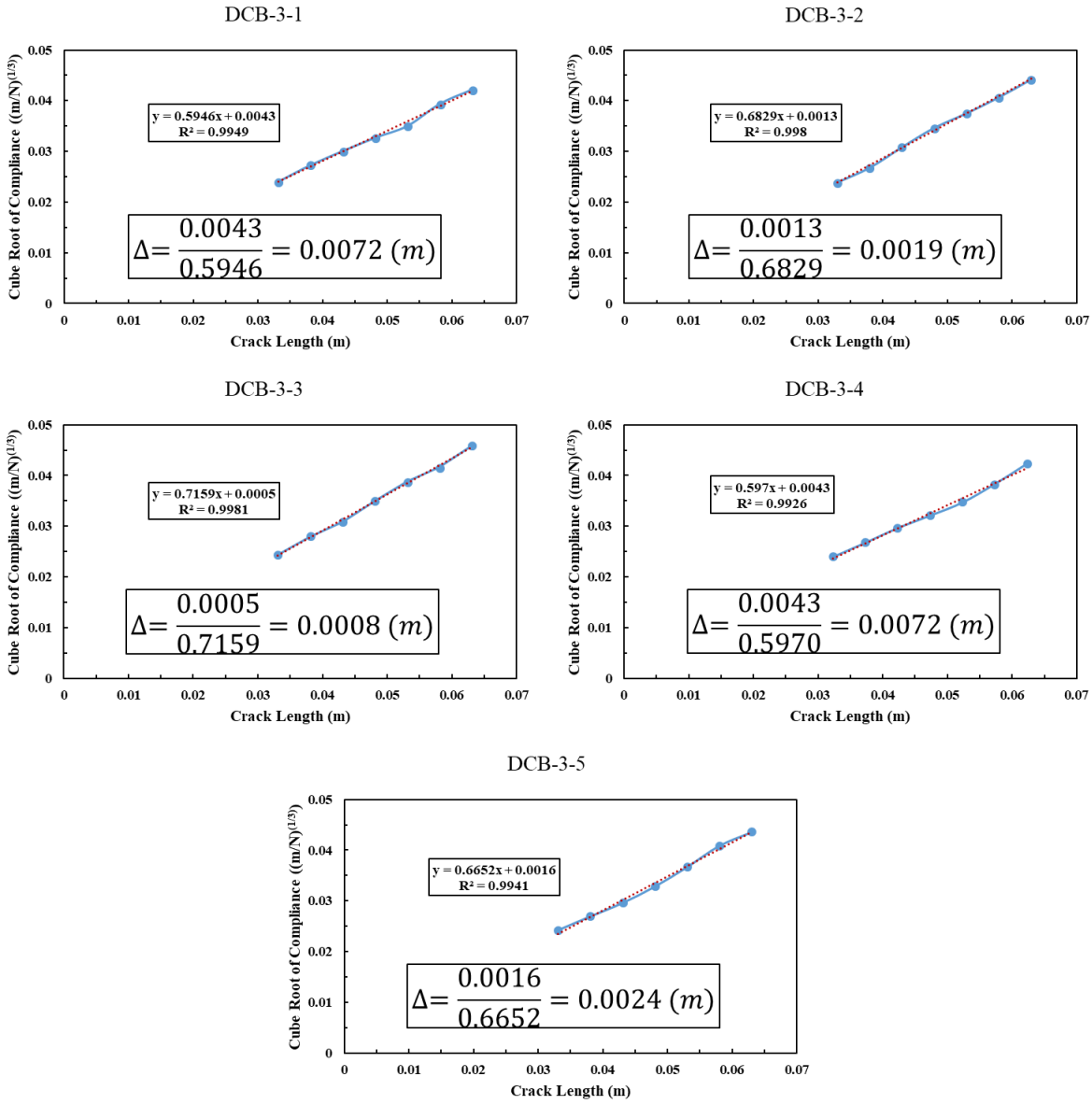

Figure A.1.3. The least-square plot of the cube root of the compliance versus the crack length for the DCB specimens comprising CFRP adherends with 53% fibre volume fraction with 0.4 mm adhesive bond-line thickness with a loading rate of 0.1 mm/s.

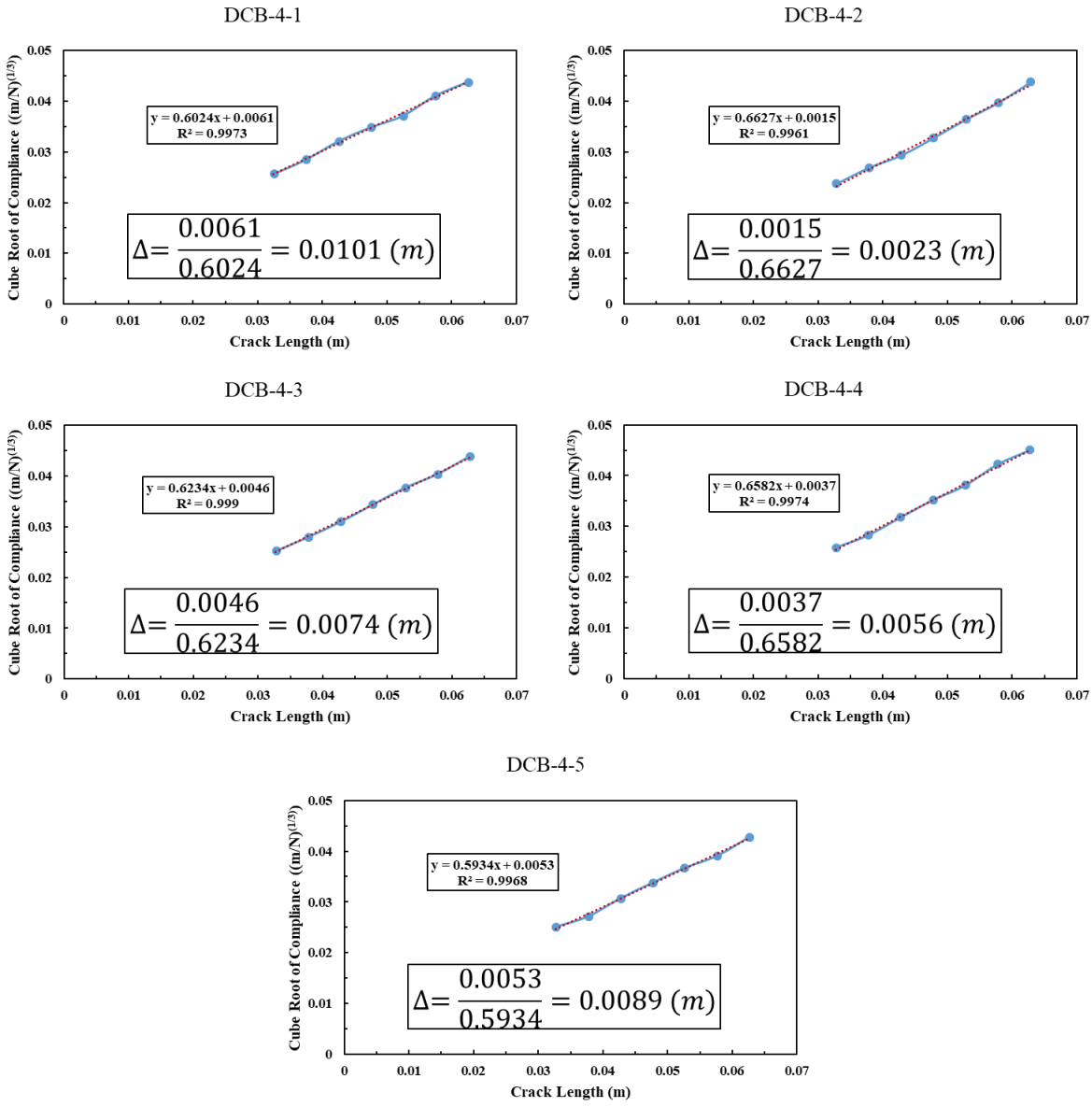

Figure A.1.4. The least-square plot of the cube root of the compliance versus the crack length for the DCB specimens comprising CFRP adherends with 53% fibre volume fraction with 0.65 mm adhesive bond-line thickness with a loading rate of 0.1 mm/s.

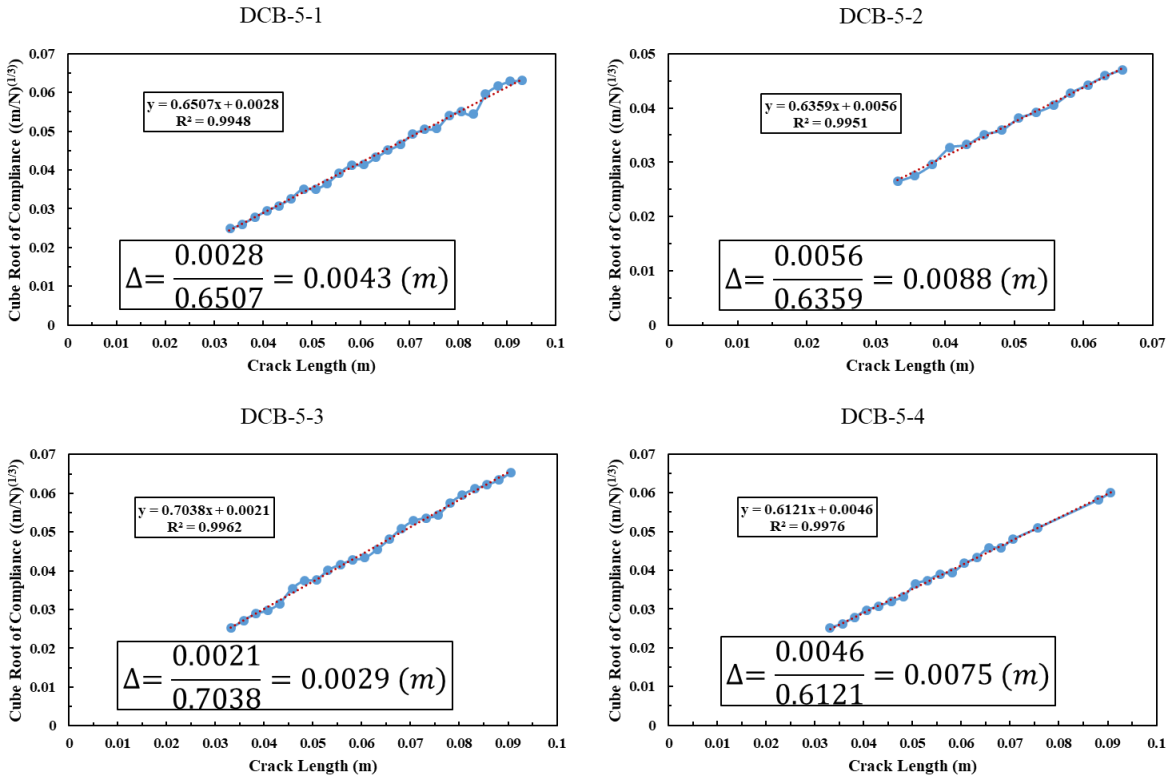

Figure A.1.5. The least-square plot of the cube root of the compliance versus the crack length for the DCB specimens comprising CFRP adherends with 53% fibre volume fraction with 0.4 mm adhesive bond-line thickness with a loading rate of 5.0 mm/s.

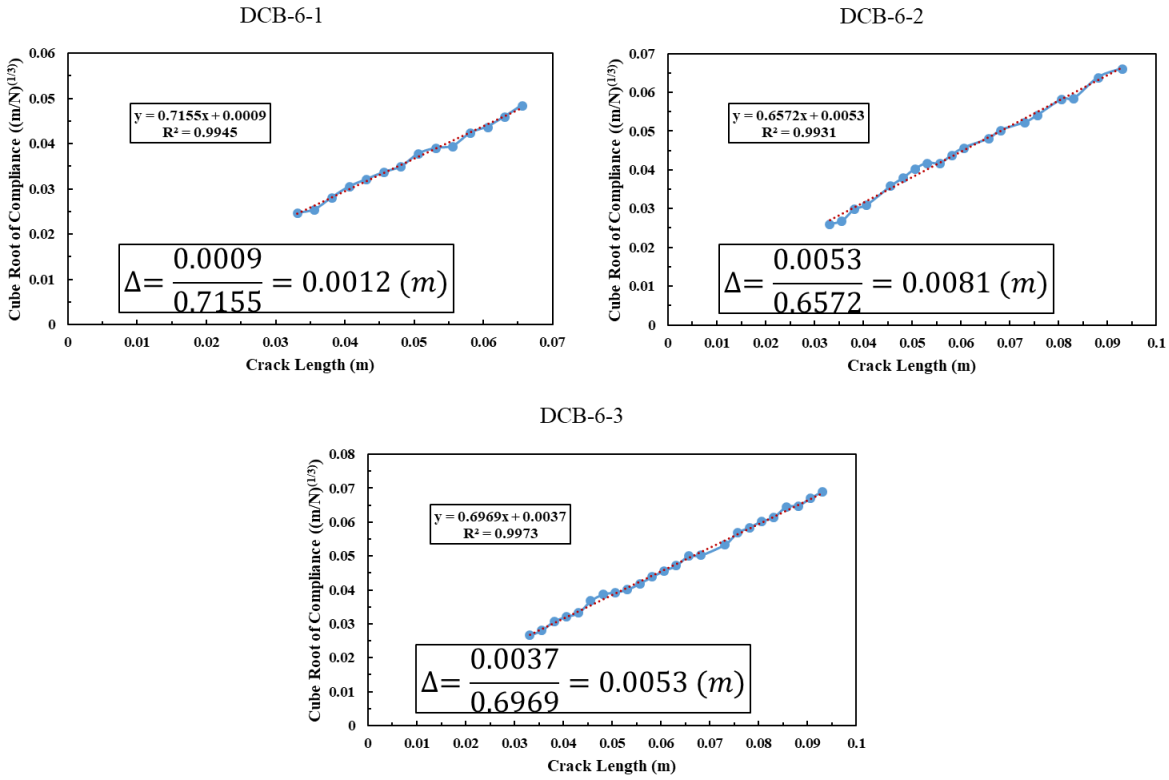

Figure A.1.6. The least-square plot of the cube root of the compliance versus the crack length for the DCB specimens comprising CFRP adherends with 53% fibre volume fraction with 0.4 mm adhesive bond-line thickness with a loading rate of 15.0 mm/s.

Appendix B

Copyright permissions

SPRINGER NATURE LICENSE
TERMS AND CONDITIONS
Mar 24, 2021

This Agreement between University of Waterloo -- Ramin Chitsaz Dehaghani ("You") and Springer Nature ("Springer Nature") consists of your license details and the terms and conditions provided by Springer Nature and Copyright Clearance Center.

License Number	5022681221047
License date	Mar 05, 2021
Licensed Content Publisher	Springer Nature
Licensed Content Publication	Springer eBook
Licensed Content Title	Failure Mechanisms and Criteria
Licensed Content Author	Holm Altenbach, Johannes Altenbach, Wolfgang Kissing
Licensed Content Date	Jan 1, 2004
Type of Use	Thesis/Dissertation
Requestor type	academic/university or research institute
Format	electronic
Portion	figures/tables/illustrations
Number of figures/tables/illustrations	4
Will you be translating?	no
Circulation/distribution	50000 or greater
Author of this Springer Nature content	no
Title	Experimental and Numerical Assessment of Adhesively Bonded Non-Crimp Fabric Carbon Fiber/Epoxy Composite Joints
Institution name	University of Waterloo
Expected presentation date	Mar 2021
Portions	Figures 6.1 on page 185
Requestor Location	University of Waterloo 200 University Avenue Waterloo, ON N2L 3E9 Canada Attn: University of Waterloo
Total	0.00 CAD

ELSEVIER LICENSE
TERMS AND CONDITIONS
Mar 24, 2021

This Agreement between University of Waterloo -- Ramin Chitsaz Dehaghani ("You") and Elsevier ("Elsevier") consists of your license details and the terms and conditions provided by Elsevier and Copyright Clearance Center.

License Number	5022690411164
License date	Mar 05, 2021
Licensed Content Publisher	Elsevier
Licensed Content Publication	Journal of Manufacturing Processes
Licensed Content Title	Studies on the influence of surface treatment type, in the effectiveness of structural adhesive bonding, for carbon fiber reinforced composites
Licensed Content Author	V.H. Martínez-Landeros,S.Y. Vargas-Islas,Celso E. Cruz-González,S. Barrera,K. Mourtazov,R. Ramírez-Bon
Licensed Content Date	Mar 1, 2019
Licensed Content Volume	39
Licensed Content Issue	n/a
Licensed Content Pages	7
Start Page	160
End Page	166
Type of Use	reuse in a thesis/dissertation
Portion	figures/tables/illustrations
Number of figures/tables/illustrations	2
Format	electronic
Are you the author of this Elsevier article?	No
Will you be translating?	No
Title	Experimental and Numerical Assessment of Adhesively Bonded Non-Crimp Fabric Carbon Fiber/Epoxy Composite Joints
Institution name	University of Waterloo
Expected presentation date	Mar 2021
Portions	Fig. 2 and Fig. 7
Requestor Location	University of Waterloo 200 University Avenue Waterloo, ON N2L 3E9 Canada Attn: University of Waterloo
Publisher Tax ID	GB 494 6272 12
Total	0.00 CAD

ELSEVIER LICENSE
TERMS AND CONDITIONS
Mar 24, 2021

This Agreement between University of Waterloo -- Ramin Chitsaz Dehaghani ("You") and Elsevier ("Elsevier") consists of your license details and the terms and conditions provided by Elsevier and Copyright Clearance Center.

License Number	5026151507984
License date	Mar 11, 2021
Licensed Content Publisher	Elsevier
Licensed Content Publication	International Journal of Adhesion and Adhesives
Licensed Content Title	Low pressure plasma treatment of CFRP substrates for adhesive bonding: an investigation of joint durability under severe temperature-moisture conditioning
Licensed Content Author	M. Pizzorni,E. Lertora,C. Mandolfino
Licensed Content Date	Jun 1, 2020
Licensed Content Volume	99
Licensed Content Issue	n/a
Licensed Content Pages	1
Start Page	102592
End Page	0
Type of Use	reuse in a thesis/dissertation
Portion	figures/tables/illustrations
Number of figures/tables/illustrations	1
Format	electronic
Are you the author of this Elsevier article?	No
Will you be translating?	No
Title	Experimental and Numerical Assessment of Adhesively Bonded Non-Crimp Fabric Carbon Fiber/Epoxy Composite Joints
Institution name	University of Waterloo
Expected presentation date	Mar 2021
Portions	Fig.4
Requestor Location	University of Waterloo 200 University Avenue WaterlooON N2L 3E9 Canada Attn: University of Waterloo
Publisher Tax ID	GB 494 6272 12
Total	0.00 CAD

ELSEVIER LICENSE
TERMS AND CONDITIONS
Mar 24, 2021

This Agreement between University of Waterloo -- Ramin Chitsaz Dehaghani ("You") and Elsevier ("Elsevier") consists of your license details and the terms and conditions provided by Elsevier and Copyright Clearance Center.

License Number	5026160212477
License date	Mar 11, 2021
Licensed Content Publisher	Elsevier
Licensed Content Publication	Reinforced Plastics
Licensed Content Title	Using excimer lasers to clean CFRP prior to adhesive bonding
Licensed Content Author	Fabian Fischer,Stefan Kreling,Frank Gäbler,Ralph Delmdahl
Licensed Content Date	September–October 2013
Licensed Content Volume	57
Licensed Content Issue	5
Licensed Content Pages	4
Start Page	43
End Page	46
Type of Use	reuse in a thesis/dissertation
Portion	figures/tables/illustrations
Number of figures/tables/illustrations	1
Format	electronic
Are you the author of this Elsevier article?	No
Will you be translating?	No
Title	Experimental and Numerical Assessment of Adhesively Bonded Non-Crimp Fabric Carbon Fiber/Epoxy Composite Joints
Institution name	University of Waterloo
Expected presentation date	Mar 2021
Portions	Figure 2
Requestor Location	University of Waterloo 200 University Avenue Waterloo ON N2L 3E9 Canada Attn: University of Waterloo
Publisher Tax ID	GB 494 6272 12
Total	0.00 CAD

ELSEVIER LICENSE
TERMS AND CONDITIONS
Mar 24, 2021

This Agreement between University of Waterloo -- Ramin Chitsaz Dehaghani ("You") and Elsevier ("Elsevier") consists of your license details and the terms and conditions provided by Elsevier and Copyright Clearance Center.

License Number	5026160346270
License date	Mar 11, 2021
Licensed Content Publisher	Elsevier
Licensed Content Publication	International Journal of Adhesion and Adhesives
Licensed Content Title	UV-laser cleaning and surface characterization of an aerospace carbon fibre reinforced polymer
Licensed Content Author	B. Rauh,S. Kreling,M. Kolb,M. Geistbeck,S. Boujenfa,M. Suess,K. Dilger
Licensed Content Date	Apr 1, 2018
Licensed Content Volume	82
Licensed Content Issue	n/a
Licensed Content Pages	10
Start Page	50
End Page	59
Type of Use	reuse in a thesis/dissertation
Portion	figures/tables/illustrations
Number of figures/tables/illustrations	1
Format	electronic
Are you the author of this Elsevier article?	No
Will you be translating?	No
Title	Experimental and Numerical Assessment of Adhesively Bonded Non-Crimp Fabric Carbon Fiber/Epoxy Composite Joints
Institution name	University of Waterloo
Expected presentation date	Mar 2021
Portions	Fig. 15
Requestor Location	200 University Avenue Waterloo, ON N2L 3E9 Canada Attn: University of Waterloo
Publisher Tax ID	GB 494 6272 12
Total	0.00 CAD

ELSEVIER LICENSE
TERMS AND CONDITIONS
Mar 24, 2021

This Agreement between University of Waterloo -- Ramin Chitsaz Dehaghani ("You") and Elsevier ("Elsevier") consists of your license details and the terms and conditions provided by Elsevier and Copyright Clearance Center.

License Number	5026160500407
License date	Mar 11, 2021
Licensed Content Publisher	Elsevier
Licensed Content Publication	Surface and Coatings Technology
Licensed Content Title	Influence of the composite surface structure on the peel strength of metallized carbon fibre-reinforced epoxy
Licensed Content Author	E. Njuhovic,A. Witt,M. Kempf,F. Wolff-Fabris,S. Glöde,V. Altstädt
Licensed Content Date	Oct 15, 2013
Licensed Content Volume	232
Licensed Content Issue	n/a
Licensed Content Pages	7
Start Page	319
End Page	325
Type of Use	reuse in a thesis/dissertation
Portion	figures/tables/illustrations
Number of figures/tables/illustrations	5
Format	electronic
Are you the author of this Elsevier article?	No
Will you be translating?	No
Title	Experimental and Numerical Assessment of Adhesively Bonded Non-Crimp Fabric Carbon Fiber/Epoxy Composite Joints
Institution name	University of Waterloo
Expected presentation date	Mar 2021
Portions	Fig.2, Fig. 3, Fig.4, Fig,5 and Fig.6
Requestor Location	University of Waterloo 200 University Avenue Waterloo, ON N2L 3E9 Canada Attn: University of Waterloo
Publisher Tax ID	GB 494 6272 12
Total	0.00 CAD

ELSEVIER LICENSE
TERMS AND CONDITIONS

Mar 24, 2021

This Agreement between University of Waterloo -- Ramin Chitsaz Dehaghani ("You") and Elsevier ("Elsevier") consists of your license details and the terms and conditions provided by Elsevier and Copyright Clearance Center.

License Number	5026161139169
License date	Mar 11, 2021
Licensed Content Publisher	Elsevier
Licensed Content Publication	Composites Part A: Applied Science and Manufacturing
Licensed Content Title	Strength and failure modes of surface treated CFRP secondary bonded single-lap joints in static and fatigue tensile loading regimes
Licensed Content Author	Seong-Min Park,Rene Roy,Jin-Hwe Kweon,Youngwoo Nam
Licensed Content Date	Jul 1, 2020
Licensed Content Volume	134
Licensed Content Issue	n/a
Licensed Content Pages	1
Start Page	105897
End Page	0
Type of Use	reuse in a thesis/dissertation
Portion	figures/tables/illustrations
Number of figures/tables/illustrations	2
Format	electronic
Are you the author of this Elsevier article?	No
Will you be translating?	No
Title	Experimental and Numerical Assessment of Adhesively Bonded Non-Crimp Fabric Carbon Fiber/Epoxy Composite Joints
Institution name	University of Waterloo
Expected presentation date	Mar 2021
Portions	Table 5 and Table 7
Requestor Location	University of Waterloo 200 University Avenue Waterloo, ON N2L 3E9 Canada Attn: University of Waterloo
Publisher Tax ID	GB 494 6272 12
Total	0.00 CAD

ELSEVIER LICENSE
TERMS AND CONDITIONS
Mar 24, 2021

This Agreement between University of Waterloo -- Ramin Chitsaz Dehaghani ("You") and Elsevier ("Elsevier") consists of your license details and the terms and conditions provided by Elsevier and Copyright Clearance Center.

License Number	5026170222261
License date	Mar 11, 2021
Licensed Content Publisher	Elsevier
Licensed Content Publication	International Journal of Solids and Structures
Licensed Content Title	The fracture behaviour of adhesively-bonded composite joints: Effects of rate of test and mode of loading
Licensed Content Author	B.R.K. Blackman,A.J. Kinloch,F.S. Rodriguez-Sanchez,W.S. Teo
Licensed Content Date	Jun 15, 2012
Licensed Content Volume	49
Licensed Content Issue	13
Licensed Content Pages	19
Start Page	1434
End Page	1452
Type of Use	reuse in a thesis/dissertation
Portion	figures/tables/illustrations
Number of figures/tables/illustrations	1
Format	electronic
Are you the author of this Elsevier article?	No
Will you be translating?	No
Title	Experimental and Numerical Assessment of Adhesively Bonded Non-Crimp Fabric Carbon Fiber/Epoxy Composite Joints
Institution name	University of Waterloo
Expected presentation date	Mar 2021
Portions	Fig.10
Requestor Location	University of Waterloo 200 University Avenue Waterloo, ON N2L 3E9 Canada Attn: University of Waterloo
Publisher Tax ID	GB 494 6272 12
Total	0.00 CAD

SPRINGER NATURE LICENSE
TERMS AND CONDITIONS

Mar 24, 2021

This Agreement between University of Waterloo -- Ramin Chitsaz Dehaghani ("You") and Springer Nature ("Springer Nature") consists of your license details and the terms and conditions provided by Springer Nature and Copyright Clearance Center.

License Number	5026170538461
License date	Mar 11, 2021
Licensed Content Publisher	Springer Nature
Licensed Content Publication	Springer eBook
Licensed Content Title	Advances in Numerical Modelling of Adhesive Joints
Licensed Content Author	Lucas F. M. da Silva, Raul D. S. G. Campilho
Licensed Content Date	Jan 1, 2012
Type of Use	Thesis/Dissertation
Requestor type	academic/university or research institute
Format	electronic
Portion	figures/tables/illustrations
Number of figures/tables/illustrations	1
Will you be translating?	no
Circulation/distribution	20000 - 49999
Author of this Springer Nature content	no
Title	Experimental and Numerical Assessment of Adhesively Bonded Non-Crimp Fabric Carbon Fiber/Epoxy Composite Joints
Institution name	University of Waterloo
Expected presentation date	Mar 2021
Portions	Fig. 11
Requestor Location	University of Waterloo 200 University Avenue Waterloo, ON N2L 3E9 Canada Attn: University of Waterloo
Total	0.00 CAD

ELSEVIER LICENSE
TERMS AND CONDITIONS
Mar 24, 2021

This Agreement between University of Waterloo -- Ramin Chitsaz Dehaghani ("You") and Elsevier ("Elsevier") consists of your license details and the terms and conditions provided by Elsevier and Copyright Clearance Center.

License Number	5026170668637
License date	Mar 11, 2021
Licensed Content Publisher	Elsevier
Licensed Content Publication	Polymer Testing
Licensed Content Title	Quasi-static and dynamic characterization of unidirectional non-crimp carbon fiber fabric composites processed by HP-RTM
Licensed Content Author	Aleksandr Cherniaev,Yu Zeng,Duane Cronin,John Montesano
Licensed Content Date	Jul 1, 2019
Licensed Content Volume	76
Licensed Content Issue	n/a
Licensed Content Pages	11
Start Page	365
End Page	375
Type of Use	reuse in a thesis/dissertation
Portion	figures/tables/illustrations
Number of figures/tables/illustrations	1
Format	electronic
Are you the author of this Elsevier article?	No
Will you be translating?	No
Title	Experimental and Numerical Assessment of Adhesively Bonded Non-Crimp Fabric Carbon Fiber/Epoxy Composite Joints
Institution name	University of Waterloo
Expected presentation date	Mar 2021
Portions	Table 1
Requestor Location	University of Waterloo 200 University Avenue Waterloo, ON N2L 3E9 Canada Attn: University of Waterloo
Publisher Tax ID	GB 494 6272 12
Total	0.00 CAD